This is to certify that the

dissertation entitled

Femtosecond Reaction

Dynamics in the Gas Phase

presented by

Una Marvet

has been accepted towards fulfillment
of the requirements for

Ph.D. degree in Physical Chemistry

Major professor

Date 12-14-98

FEMTOSECOND REACTION DYNAMICS IN THE GAS PHASE

By

Una Marvet

A DISSERTATION

Submitted to
Michigan State University
in partial fulfillment of the requirements
for the degree of

DOCTOR OF PHILOSOPHY

Department of Chemistry

1998

FE

...dvent of s

...ped by whic

...am of proc

...ples. This is p

...occurring in

...observed by

...ly of two

...scopy.

...he first invol

...Cames using

...ted by select

...und to be ge

...gate molecul

...orescence dep

...served in so

...ds of the spec

ABSTRACT

FEMTOSECOND REACTION DYNAMICS IN THE GAS PHASE

By

Una Marvet

The advent of short pulsed laser sources has allowed time-resolved methods to be developed by which molecular dynamics can be studied directly. This facilitates the observation of processes that may not be amenable to study by frequency-resolved techniques. This is particularly so in the case of reaction dynamics, where many changes may be occurring in a short period of time and the transition state is too short-lived to be readily observed by continuous wave (cw) methods. The work described here involves the study of two such processes in the gas phase by femtosecond pump-probe spectroscopy.

The first involves photoinduced molecular detachment of halogens from gem-dihaloalkanes using a 312 nm femtosecond pulse. The progress of the reaction is monitored by selective detection of fluorescence from the halogen product. The reaction was found to be general to a number of dihaloalkanes, and in every case to produce the appropriate molecular halogen product in the D' state. Molecular dynamics were probed by fluorescence depletion using a femtosecond pulse at 624 nm. Vibrational coherence was observed in some halogen products, indicating a concerted reaction mechanism. Analysis of the spectroscopic and dynamic data was performed; it was determined that

...e molecular c...

...mechanism...

...econd exper...

...ress. pairs of...

...ate using a...

...by fluoresce...

...py in the ...

...ssociative. The...

...parameter...

for one molecular detachment channel the reaction proceeds by an asynchronous concerted mechanism.

The second experiment is a real-time study of an unrestricted bimolecular reaction. In this process, pairs of gas phase mercury atoms are photoassociated to an electronically excited state using a femtosecond pulse. The dynamics of the resulting molecules are probed by fluorescence depletion using a second pulse. Analysis of the rotational anisotropy in the nascent dimers conclusively confirms that dimer formation is photoassociative. The degree of rotational excitation in the nascent molecules indicates the impact parameter selectivity of the photoassociation process.

for Jon, with love

In the course of

helped me in s

I would particul

rain good-humou

rician, with w

Zhang appr

description, a

Mark Waner d

small hours.

I would also lik

the graduate

Russ and Sam

And finally to M

Thank you.

ACKNOWLEDGMENTS

In the course of my graduate career I have encountered a lot of people, most of whom have helped me in some way.

I would particularly like to thank Pedro Cid-Aguero, who has a remarkable ability to remain good-humoured under all sorts of aggravation. Peter Gross is a truly practical theoretician, with whom discussions were invariably stimulating, no matter the subject. Qingguo Zhang applies an unparalleled attention for detail to every problem. Igor Pastirk defies description, and Emily Brown is one of the hardest-working people I have ever met. Mark Waner deserves a medal for his willingness to help produce posters into the wee small hours.

I would also like to thank some of the non-academic staff at Michigan State, most notably the graduate secretary Lisa Dillingham, Scott and Manfred in the glass shop and Dick, Russ and Sam in the machine shop.

And finally to Marcos, my advisor. It hasn't always been smooth, but it was rarely boring. Thank you.

TABLE OF CONTENTS

Photodiss

Thermody
X = H or a

Energetics
the minim
produce C
energies ar

Comparis

LIST OF TABLES

Schematic o

a The pulse
rovibronic
propagates
the potentia
pulse monit

b Periodic mo
pump-probe

Definitions
between the
pump and p
are manifes
transition di
pump and
parallel to t
are averaged

Clocking fig

a Potentials i
ultrashort p
wavelengths
V_2 transitio
closely reser

b Transients o
resonant wit
decays rapi
coupled regi
approached

Schematic o
harmonic of
amplified be

LIST OF FIGURES

Sketch of t

Detail of th

Experimen
Nd:YAG la
used to s
recompress
and a scan
linearly rec
as fluoresc
being sent

Schematic

Typical FI
positively
the beam a

Dispersed
CH_2I_2 at 3
be assigne
detected a
produced b
not been co

Dispersed
photoinduc
multiphoto
not correct

Spectrum r

Ambient (r

Ambient te

Excitation
iodine vapo

2.2 Sketch of the amplification mechanism.

2.3 Detail of the Bethune cells.

2.4 Experimental setup. A pulse from the CPM is collected by a photodiode. The Nd:YAG laser is triggered by the amplified pulse from the diode; an SM-1 unit is used to synchronise the pulses. After amplification, the CPM beam is recompressed and steered to a Mach-Zehnder interferometer having a fixed arm and a scanning arm. One arm is frequency doubled, and the two beams are linearly recombined before being focussed into the sample cell. Signal is collected as fluorescence by a monochromator and PMT then averaged in a boxcar before being sent to the computer. The boxcar is also triggered by the CPM.

2.5 Schematic of the frequency-resolved optical gating (FROG) system.

2.6 Typical FROG traces, showing (a) negatively chirped, (b) unchirped and (c) positively chirped pulses. The chirp is altered by translating the prism P2 across the beam as shown.

3.1 Dispersed fluorescence spectrum of I_2, produced by multiphoton dissociation of CH_2I_2 at 312 nm. The dominant fluorescence is between 290 and 350 nm and can be assigned to the I_2 D' $\rightarrow$ A' transition. A small amount of laser scatter is detected at 312 nm (shaded). The region marked (i) indicates fluorescence produced by other ion-pair states of I_2 (see text). The fluorescence intensity has not been corrected for detection efficiency of the spectrometer.

3.2 Dispersed fluorescence spectra of the D' state of I_2. The spectra were produced by photoinduced molecular detachment of I_2 from CH_2I_2 in a static cell by multiphoton excitation at 312 nm. The spectra are normalised and calibrated, but not corrected for detection efficiency of the spectrometer.

(a) Spectrum recorded at 0 °C.

(b) Ambient (room) temperature spectrum at 1 Torr.

(c) Ambient temperature spectrum in the presence of 80 Torr of Ar.

3.3 Excitation scheme and corresponding time-resolved (pump-probe) data for neat iodine vapour, showing how the observed transient is generated.

a A 624 nm
nm pulse c
transitions
fluorescen

b At negativ
reached ar
becomes p
positive tir

c Excitation
showing h
to the ioni

a Initially, t
pulse. Thi
undergoes

b Absorption
D' state. D
by detecti
may not b
eV from t
fluorescen
remains at
enhanceme
text). At p
population
of vibrati
wavepacke
time corre
sample pos

c Time-resol
positive tir
the pump
obtained v
vibrational

d Possible ex
threshold ir

(a) A 624 nm (pump) pulse excites I_2 to the B state; subsequent absorption of a 312 nm pulse causes transition to the E and f ion-pair states. These have strong, bright transitions to the valence states A and B. The detected signal is f → B fluorescence at 340 nm.

(b) At negative times (probe pulse arriving before pump), neither the E nor f state is reached and no signal is observed. As the pulses become overlapped in time, it becomes possible to access the f state and molecular fluorescence is obtained. At positive times, vibrational coherence characteristic of I_2(B) is observed.[33]

3.4 Excitation scheme and corresponding time-resolved (pump-probe) data for CH_2I_2, showing how the observed time-dependent fluorescence is generated. (I. P. refers to the ionisation potential of the molecule).

(a) Initially, the molecule undergoes multiphoton absorption of the 312 nm (pump) pulse. This causes it to dissociate, producing I_2 in the D'($^3\Pi_{2g}$) state, which undergoes a fluorescent transition to A' ($^3\Pi_{2u}$), detectable at 340 nm.

(b) Absorption of a 624 nm (probe) pulse by the iodine depletes the population of the D' state. Depletion efficiency tracks the progress of the reaction and is monitored by detecting the D'→ A' fluorescence at 340 nm. Note that the probe transition may not be as represented; there are a number of optically accessible I_2 states 2 eV from the D' state.[170,148] At negative times (probe pulse arriving first), the fluorescence produced by the D' → A' transition is unaffected by the probe, and remains at a constant level. As the pulses begin to overlap in time, an intense enhancement is observed; this is due to a cooperative multiphoton effect (see text). At positive times, absorption of the 624 nm (probe) pulse depletes the population of the D' state, and the fluorescence intensity decreases. Observation of vibrational modulation in the depletion signal indicates that a coherent wavepacket is generated in the D' state of I_2. Note that for the I_2 transient, positive time corresponds to the 624 nm pulse arriving at the cell first; for the CH_2I_2 sample positive time is when the 312 nm pulse arrives first.

3.5 Time-resolved data and vibrational fit to the D' → A' fluorescence at 340 nm and positive times. The data was collected with the probe laser polarised parallel to the pump and fit to a function $A+Be^{-t/\tau}\cos(\omega t+\phi)$. The fit displayed was obtained with an oscillation frequency ω of 92.2 cm^{-1}, corresponding to a vibrational period of 362 fs. The dephasing time τ was ~ 1 ps.

3.6 Possible excitation schemes to produce time zero fluorescence enhancement. The threshold indicated is the observed excitation threshold for production of CH_2 and

$I_2(D')$. The
correspond

a One photo
624 (probe
photon of
312 nm is
$(^1B_1)$ state

b An initial
requiring
equivalent
unknown.

c A three-ph
pathway o
pump and
molecular
investigati

Kinetic mo
comprised

a Depletion
CH_2I_2 with
dissociates
pulse probe

b Time zero
CH_2I_2 to a
excited pa
observed b
lifetime τ
excitation t

c The overall
convoluted

Time-resolv
$C_4H_8I_2$. The
accounted f
fit to the C_4
oscillation a

$I_2(D')$. The upper line on the figure corresponds to 12 eV, the excitation energy corresponding to a three-photon pump transition.

(a) One photon excitation with the 312 nm (pump) pulse requires three photons of 624 (probe) nm light to reach the threshold for production of $I_2(D')$. An additional photon of the probe produces an excitation of 12 eV. Single-photon absorption at 312 nm is equivalent to an excitation of 4 eV, which is sufficient to reach the $\tilde{A}$ ($^1B_1$) state of CH_2I_2 (marked (i) in the Figure).

(b) An initial absorption of two pump photons corresponds to an excitation of 8 eV, requiring one photon of 624 nm light to reach the threshold and two to be equivalent to an excitation of 12 eV. The pump-excited state, marked (ii), is unknown.

(c) A three-photon pump corresponds to an initial excitation of 12 eV. This is the pathway of the most interest to us because the dynamics observed between the pump and probe pulses correspond to the transition state of the photoinduced molecular detachment reaction. The state (iii) is the dissociative state under investigation.

3.7 Kinetic model for the dissociation of CH_2I_2. The model assumes that the signal is comprised of two contributions:

(a) Depletion signal, produced by the molecular detachment process. Excitation of CH_2I_2 with three photons of 312 nm light produces an excited molecule, which dissociates into CH_2 and $I_2(D')$. Depletion of the D' fluorescence with a 624 nm pulse probes the dynamics of formation of $I_2(D')$.

(b) Time zero signal. When the pump and probe pulses coincide, it is possible for CH_2I_2 to absorb probe photons prior to dissociation, which produces a highly excited parent molecule. This increases the amount of D' $\rightarrow$ A' fluorescence observed because it opens another pathway for production of $I_2(D')$. The statistical lifetime τ of the pump-excited state determines for how long after the initial excitation the molecule can absorb the probe.

(c) The overall signal is a weighted sum of these two contributions, each of which is convoluted with a Gaussian to simulate the pulsewidth.

3.8 Time-resolved data of the molecular photodetachment of I_2 from CH_2I_2 and n-$C_4H_8I_2$. The difference in dissociation time between the two molecules can be accounted for by the difference in mass of the alkyl fragment. The relatively poor fit to the $C_4H_8I_2$ dynamics at positive times is due to the presence of a vibrational oscillation at early times.

Time-resolv
and perpen
polarisation
intensity of
The anisotr
population

Pump-probe
285 nm (a)
probe beam
However, th
transient do

Time-resolv
polarised pu
the two tran
both the rap
immediately

Purely isotr
in Figure 3.

(a) The pure
anisotropy

(b) The pure vi

The thicker
rotational co

Model of th
(X, Y and Z
symmetry.

Fit to the
dissociation

(a) Fit obtained

(b) The f → B fl

3.9 Time-resolved data of the CH_2I_2 dissociation obtained at 340 nm with parallel (a) and perpendicular (b) configurations; 'parallel' and 'perpendicular' refer to the polarisation of the probe beam relative to the pump. Note the much smaller intensity of the time zero feature in the perpendicular polarisation configuration. The anisotropy data is ambiguous; no reliable conclusions about the rotational population of the products can be drawn from analysis of this data.

3.10 Pump-probe data obtained by selective detection of the I_2 fluorescence signal at 285 nm (a) and at 272 nm (b). Both transients were obtained with the pump and probe beams polarised parallel to each other. Both exhibit vibrational coherence. However, the 285 nm transient exhibits a large time zero spike and the 272 nm transient does not.

3.11 Time-resolved data at 272 nm of the CH_2I_2 dissociation, obtained with the probe polarised parallel (a) and perpendicular (b) to the probe. The difference between the two transients clearly indicates rotational anisotropy in the I_2 product. Notice both the rapid anisotropy decay time and the fact that depletion is more efficient immediately after time zero in the perpendicular polarisation configuration.

3.12 Purely isotropic and anisotropic components of the time-resolved data presented in Figure 3.11.

(a) The pure rotational contribution as given by the time dependent rotational anisotropy $r(t)$.

(b) The pure vibrational contribution as given by the isotropic signal $I_{\parallel} + 2I_{\perp}$.

The thicker lines show least–squares fits to the pure vibrational and pure rotational contributions.

3.13 Model of the CH_2I_2 molecule in the centre of mass frame, showing the principal (X, Y and Z) and rotational (a, b and c) axes and their transformation under C_{2v} symmetry.

3.14 Fit to the dispersed I_2 D'→ A' fluorescence spectrum produced from the dissociation of CH_2I_2.

(a) Fit obtained using only D'→ A' fluorescence.

(b) The f → B fluorescence spectrum obtained from excitation of neat I_2 vapour.

: Fit to
possib
was sc

Fits to
probe

Origin

Bimod
FWH
FWH

Disper
312 nr

From

From
laser s

Transi
dihalo
polaris

From

From
spectr

Time
femtos
vector

Anisot
cell. T
data w

Disper
(a). CI

(c) Fit to the observed fluorescence in the 300-350 nm range, taking into account the possibility of contribution from the f → B transition. The spectrum shown in (b) was scaled by a factor determined by optimisation and incorporated into the fit.

3.15 Fits to the vibrational coherences in the I_2 D'→ A' fluorescence at positive pump-probe delay times.

(a) Original, exponentially damped sinusoidal fit shown above (Figure 3.5).

(b) Bimodal Gaussian fit. One mode has an oscillation frequency of 96.5 cm^{-1} and a FWHM of 7. The second mode has an oscillation frequency of 104 cm^{-1} and a FWHM equivalent to a single D' vibrational level.

3.16 Dispersed fluorescence spectra of X_2(D') produced by multiphoton excitation at 312 nm.

(a) From CH_2Br_2 at 0 °C.

(b) From CH_2Cl_2 at 0 °C. The increasing signal level at longer wavelengths is due to laser scatter.

3.17 Transient data of photoinduced molecular detachment of X_2(D') from dihaloalkanes. Both sets of data were recorded from static cells, with the polarisation vectors of pump and probe pulses parallel to each other.

(a) From CH_2Br_2 at 287 nm.

(b) From CH_2Cl_2 at 254 nm. The increased signal:noise ratio in this data, as in the spectrum in Figure 3.16 (b), is due to low signal levels.

3.18 Time resolved data from the multiphoton dissociation of CH_2Br_2 using 312 nm femtosecond pulses. The transients were obtained at 287 nm, with the polarisation vector of the probe laser aligned parallel (a) and perpendicular (b) to the pump.

3.19 Anisotropic (a) and isotropic (b) portions of the 287 nm data from the CH_2Br_2 cell. The fit to the *r(t)* derived from the data is also shown. To obtain the *r(t)*, the data was properly normalised and a three-point smoothing applied.

3.20 Dispersed fluorescence spectra from multiphoton excitation at 312 nm of CH_2Br_2 (a), CBr_2F_2 (b) and CBr_2Cl_2 (c). All three are produced by the Br_2 D' → A'

transitio

Time ze
data are
with the

a) CH_2Br_2

b) CBr_2F_2

c) CBr_2Cl_2

Dispers
°C. sho
spectra
for com

Pump-p

a) Collecte

b) Collecte

Pump-p
reservoi
polarise

a) The pur
least-sq
(i) and a

b) The rot
results a

Pump-p
from the
are also

Normal
and CH_2

transition.

3.21 Time zero data for the molecular detachment of halogens from CX_2Br_2. Fits to the data are shown as continuous lines. The time data was obtained consecutively, with the same laser intensity for each scan.

(a) CH_2Br_2 at 0 °C.

(b) CBr_2F_2 at -47 °C.

(c) CBr_2Cl_2 at 0 °C.

3.22 Dispersed fluorescence spectra from the multiphoton dissociation of CH_2ICl at 0 °C, showing both the 320 - 400 and the 400 - 460 nm regions. The fluorescence spectra produced in these regions from a sample of pure I_2 vapour are also shown for comparison.

3.23 Pump-probe data from the multiphoton dissociation of CH_2ICl at 312 nm.

(a) Collected at 340 nm, corresponding to the G $\rightarrow$ A transition.

(b) Collected at 430 nm, corresponding to the D' $\rightarrow$ A' transition.

3.24 Pump-probe data was collected from the CH_2ICl sample at 340 nm with the liquid reservoir maintained at 0 °C. Dynamics were studied with the probe laser polarised both parallel and perpendicular to the pump.

(a) The purely anisotropic contribution *r(t)* to the 340 nm signal. Also shown are a least-squares fit obtained by assuming a Gaussian distribution of rotational levels (i) and a thermal (Boltzmann) distribution (ii).

(b) The rotational populations *P(j)* responsible for the fits shown in (a). The two results are very similar, and produce almost identical fits.

3.25 Pump-probe data collected from the CH_2ICl sample. Fits to the data obtained from the Fourier transform and from the exponential decay model (Equation 3.1) are also displayed.

3.26 Normal mode analysis of the ground state of CH_2I_2, plotted as a function of I-I and CH_2-I distance. Only the I-C-I bending (ν_4) and I-C-I symmetric stretch (ν_3)

modes co

Schemati
X- from g
given for

Synchron
initiated
forms be
a symmet

Asynchr
carbon-h
before th

Classical
large sph
moiety. I
be separa

The three
first bond
assumed

The asyn
to be 2.7
assumed

Depende
breaking
concerte
stated for

Schemati
photoass
asymptot

Dispersed
static cell

Excitation

Using a 6
compare
differenc
from two

Femtosec
nm. Dat
perpendi
pulse and
molecule

a Rotationa
the best f

Rotationa
rotationa

Schemati
impact p
of collisi
function

The diffe
as a func
energies
formed v
nm the
theoretic

(b) Using a 60 fs laser pulse centred at 312 nm. The D → X emission is red-shifted compared to the emission produced by 266 nm excitation because of the difference in excitation energy. The peak at 407.8 nm is an atomic line resulting from two-photon excitation to the 7^1S_0 state.

4.3 Femtosecond pump-probe transients from the photoassociation of mercury at 312 nm. Data was collected with the probe laser polarised parallel (a) and perpendicular (b) to the binding laser. Note that bond formation occurs during the pulse and that the data is clearly anisotropic, indicating alignment of the nascent molecules.

4.4 (a) Rotational anisotropy *r(t)* obtained from the experimental data. The heavy line is the best fit to the experimental data (plotted as points), as described in the text.

(b) Rotational population of the photoassociated product, obtained from the fit to the rotational anisotropy.

4.5 Schematic of a bimolecular collision process, illustrating the definition of the impact parameter *b*. The equations show the relation between the relative energy of collision E_R and the energy $E_\perp$ along the direction of the interatomic axis as a function of the impact parameter.

4.6 The differential photoassociation cross section $d\sigma_{PA}/db$ from Equation 4.9, plotted as a function of binding wavelength. Note that as the wavelength is tuned to lower energies the reaction requires smaller impact parameters and the products are formed with a narrower, lower energy distribution of rotational excitation. At 290 nm the photoassociation process is not very restrictive and approaches the theoretical limit $P(b) = 1$ (see text).

LIST

Symbol
Å
c
h
h
IR
J
mJ
k
m
nm
s
ns
ps
fs
W
mW

LIST OF SYMBOLS AND ABBREVIATIONS

Symbol	Meaning
Å	Ångstrom, 10^{-10} metre
c	Speed of light in vacuum
h	Planck's constant
$\hbar$	$h/2\pi$
IR	Infrared
J	Joule
mJ	millijoule, 10^{-3} J
k	Boltzmann's constant
m	metre
nm	nanometre, 10^{-9} m
s	second
ns	nanosecond, 10^{-9} s
ps	picosecond, 10^{-12} s
fs	femtosecond, 10^{-15} s
W	Watt
mW	milliwatt, 10^{-3} W

Frequency

1. INTRODUCTION

1.1 Frequency Resolved Spectroscopy and Reaction Dynamics

Frequency-resolved spectroscopy involves the excitation of matter using a narrow bandwidth source. By this method, single quantum states of materials can be interrogated in order to determine energy level spacing and the shape of potential energy surfaces (PES's). In the case where excitation leads to a chemical reaction, the observation of changes in the spectroscopy of a sample as a reaction evolves can provide information about the progress of the reaction.

An alternative approach is to use crossed molecular beam techniques, which allow the increasingly sensitive selection of reactant states, thereby facilitating state-to-state scattering experiments.[1,2] This method relies on asymptotic properties, for example the translational excitation and spatial distribution of the products, to yield information about the characteristics of the potential energy surface along which a reaction occurs. These are statistical measurements, *i.e.* they reveal the kinetic behaviour of a thermally averaged ensemble of molecules.

To probe microscopic chemical reaction dynamics, changes in the PES can be studied by analysis of phenomena such as line-broadening.[3,4] These methods rely on the fact that the dynamic behaviour of a system is representable as the Fourier transform of the frequency-resolved spectrum. However, it can be difficult to interpret diffuse spectra,

...ularly in p

...ription of sta

...sition state re

...y short lifetim

...ures

...2 Time-Reso

...2.1 Introducti

The develop

...thodology for

...y short (< 1

...typical duratio

...quantum leve

...he resulting w

...ured directly

...2.2 Preparati

Excitation w

...sition of the

...ssing occur

...ce of a molec

Multiphoton

particularly in polyatomic molecules, because a number of other factors such as congestion of states may also contribute to the appearance of the spectrum. Short-lived transition state regions also tend to be difficult to examine in this way because they have very short lifetimes and therefore low spectral intensity compared to reactant and product species.

1.2 Time-Resolved Spectroscopy

1.2.1 Introduction

The development of ultrashort pulse technology[5-7] has allowed an alternative methodology for the study of chemical reaction processes. This involves excitation using very short ($< 10^{-13}$ s) pulses. The uncertainty principle dictates that pulses of short temporal duration have a broad bandwidth. The effect of this bandwidth is that a number of quantum levels are populated, which creates a phase coherent superposition of states. The resulting wavepacket will evolve in time, allowing the reaction dynamics to be probed directly.

1.2.2 Preparation of the Wavepacket

Excitation with an ultrashort pulse may or may not be resonant with an electronic transition of the material irradiated. In the absence of resonances, impulsive stimulated scattering occurs.[8] This produces a phase coherent wavepacket in the ground electronic state of a molecule and has been exploited in transient grating experiments, for example.[8-10] Multiphoton absorption of IR pulses can also be used to selectively excite certain

nal modes i

The electronic

ption of the a

ndergo a vert

nfiguration ψ_f o

ere a_v are the c

ic state will in p

non-zero for m

ential energy su

ssing short tim

ximation. U

requency ω_v first-

Soxy.[3]

ere ν is the g

requency and α

2 yields

vibrational modes in the ground electronic state.[8,10-12]

The electronic resonance case is however of more relevance to this study. Absorption of a photon of the appropriate frequency allows a system in the ground electronic state V_0 to undergo a vertical transition to an excited surface potential V_1. This produces a wavefunction ψ_1 on V_1 such that

$$\psi_1 = \sum_{n=0} a_n \varphi_n \,, \tag{1.1}$$

where a_n are the coefficients of the excited state eigenfunctions φ_n. The value of a for each state will in part depend on the intensity of the pulse at the transition frequency. If a is non-zero for more than one value of n, ψ_1 is not a stationary state of the excited state potential energy surface (PES) and a wavepacket will be produced. To examine the effect of using short time duration pulses, consider a system within the Born-Oppenheimer approximation. Under excitation with a Gaussian pulse of FWHM τ and central frequency ω, first-order perturbation theory yields an expression for the coefficients a_n as follows:[13]

$$a_n = C\langle \varphi_n | \psi_0 \rangle \exp\left[-\frac{(\omega_n - \omega)^2 \alpha \tau^2}{4} \right], \tag{1.2}$$

where ψ_0 is the ground-state wavefunction of the system, $\omega_n = (E_n - E_0)/\hbar$ is the Bohr frequency and α and C are constants. In the limit of a pulse of long time duration ($\tau \rightarrow \infty$), (1.2) yields

$$a_n = C\langle \varphi_n | \psi_0 \rangle \delta(\omega_n - \omega) \,. \tag{1.3}$$

ase. a_r is

her han

esult indic

ncy sprea

d state wa

nsistent wit

dition of

ach. spect

correlation

sion produ

ent in the

rm yields

ible when

ribution of t

packet dyn

3 Dynamics

Once the wa

dependent

In this case, a_n is non-zero only when $\omega = \omega_n$, and a single eigenstate of V_1 is populated. On the other hand, in the limit of very short pulses $\tau \rightarrow 0$ and we get from (1.1) and (1.2)

$$\psi_1 = C \sum_{n=0} \langle \varphi_n | \psi_0 \rangle \varphi_n \,. \tag{1.4}$$

This result indicates that excitation with an ultrashort pulse, *i.e.* one possessing a broad frequency spread relative to the energy level spacing of the system, reproduces the ground state wavefunction, multiplied by a scaling factor, on the excited state PES. This is consistent with the semiclassical method advanced by Heller and coworkers[14-16] for the elucidation of spectra of complicated systems. In this inherently time-dependent approach, spectra are calculated from the Fourier transform of the appropriate autocorrelation function (of $\psi_1(0)$ with $\psi_1(t)$). The first step is to assume that a vertical transition produces the ground state wavefunction, multiplied by the transition dipole moment, in the excited state.[14] This wavepacket can then be propagated and the Fourier transform yields the absorption spectrum. Both Heller's model and equation (1.4) are applicable whenever the density of states of a system is high compared to the frequency distribution of the excitation and are used as the basis for many theoretical models of wavepacket dynamics.[12,17]

1.2.3 Dynamics and Probing

Once the wavepacket has been created it will begin to evolve in time according to the time-dependent Schrödinger equation:

$$i\hbar \frac{\partial \psi_1(t)}{\partial t} = \hat{H} \psi_1(t) \,. \tag{1.5}$$

Subsequent time evolution of the wavepacket on V_1 can then be described by selection of the appropriate Hamiltonian. This may be done in a full quantum-mechanical calculation, but semiclassical methods have proved effective, particularly at early times.[12,14-22]

In order to monitor the progress of the wavepacket experimentally, we use a second (probe) pulse to cause a transition from V_1 to some final state V_2. If we monitor an observable associated with the transition from V_1 to V_2 we can directly determine the dynamics of the system along V_1. A schematic is shown in Figure 1.1 (a). At some time τ after the initial excitation, the system is irradiated with the probe pulse, which will be absorbed by the excited molecules if the central frequency ω of the pulse corresponds to the resonance condition $\hbar\omega = V_2(\boldsymbol{q}) - V_1(\boldsymbol{q})$, where $V_n(\boldsymbol{q})$ is the coordinate-dependent energy of potential surface V_n. To model the time-dependent behaviour of the system, a three-level model can be applied.[23] The time-dependent Hamiltonian of the system can be considered to be a sum of contributions from the (unperturbed) molecular Hamiltonian $\hat{H}_M$ and the effects $\hat{H}_{pu}$ and $\hat{H}_{pr}$ of the pump and probe interactions respectively:

$$\hat{H}(t) = \hat{H}_M + \hat{H}_{pu} + \hat{H}_{pr}, \tag{1.6}$$

where the molecular Hamiltonian

$$\hat{H}_M = \hat{H}_0|0\rangle\langle 0| + \hat{H}_1|1\rangle\langle 1| + \hat{H}_2|2\rangle\langle 2|, \tag{1.7}$$

and $\hat{H}_n$ indicates the Hamiltonian of the system in state n. The time-dependent Schrödinger equation (1.5) can be written[17]

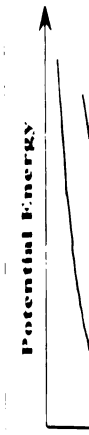

Figure 1.1 S

a The puls
electronic
propagates
the potenti
pulse monit

b Periodic
of pump-pro

The solutio

exceptions. Fi

$\tilde{V}_j(t) = \tilde{V}_j$

wave a

occurring

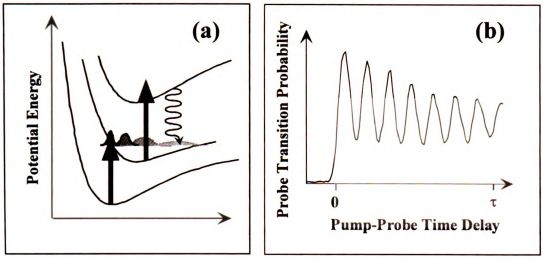

Figure 1.1 Schematic of time resolved pump-probe spectroscopy.

(a) The pulse causes a vertical transition to the excited electronic state. Several rovibronic levels are accessed, producing a phase coherent wavepacket which propagates in time as shown. As the wavepacket propagates, it spreads out along the potential energy surface (PES). Subsequent probing by absorption of a second pulse monitors the progress of the wavepacket evolution along the PES.

(b) Periodic modulation in absorption efficiency of the probe pulse as a function of pump-probe delay time.

$$i\hbar\frac{\partial}{\partial t}\begin{pmatrix}|\psi_0(t)\rangle\\|\psi_1(t)\rangle\\|\psi_2(t)\rangle\end{pmatrix}=\begin{pmatrix}h_0 & \tilde{V}_{01}(t) & \tilde{V}_{02}(t)\\ \tilde{V}_{10}(t) & h_1 & \tilde{V}_{12}(t)\\ \tilde{V}_{20}(t) & \tilde{V}_{21}(t) & h_2\end{pmatrix}\begin{pmatrix}|\psi_0(t)\rangle\\|\psi_1(t)\rangle\\|\psi_2(t)\rangle\end{pmatrix}. \qquad (1.8)$$

The solution of (1.8) is complex, but can be simplified by making certain assumptions. Firstly, we assume no direct coupling between the ground and probe states, *i.e.* $\tilde{V}_{02}(t) = \tilde{V}_{20}(t) \approx 0$. The electric field is assumed to be classical and the dipole and rotating wave approximations applied. For a pump pulse centred at $t = 0$ and a probe pulse occurring some time τ later, where τ is larger than the pulse duration, we can write[24]

$$\psi_2(\tau) = \frac{i}{\hbar}\int_{-\infty}^{\infty}\exp(i\hat{H}_2 t)\mu_{12}\exp(-i\hat{H}_1 t)\psi_1(\tau)E_2(t)dt \qquad (1.9)\ (a)$$

$$\psi_1(\tau) = \exp(-i\hat{H}_1\tau)\psi_1 \qquad (b)$$

$$\psi_1 = \frac{i}{\hbar}\int_{-\infty}^{\infty}\exp(i\hat{H}_1 t)\mu_{01}\exp(-i\hat{H}_0 t)\psi_0 E_1(t)dt\ , \qquad (c)$$

where $E_1(t)$ and $E_2(t)$ represent the electric field strengths of the pump and probe pulses respectively and μ indicates the dipole moment of the appropriate transition. Equations (1.9) show that by separating the pump and probe pulses in time, we treat the pump-probe process as a sequential excitation.

Equations (1.9) (b) and (c) describe the behaviour of the wavepacket on V_1, the state of interest. If we combine (1.1) and (1.9) (b), we can write

$$\psi_1(t) = \sum_{n=0} a_n \varphi_n \exp(-i\hat{H}_1 t) \qquad (1.10)$$

where $\hat{H}_1$ is the Hamiltonian for motion on the potential surface V_1 and φ_n are the eigenstates of V_1. Applying the time-independent Schrödinger equation to (1.10) yields (assuming $\hat{H}_1$ has no explicit time dependence)

$$\psi_1(t) = \sum_{n=0} a_n \varphi_n \exp(-iE_n t/\hbar)\,, \qquad (1.11)$$

where E_n is the energy of eigenstate φ_n. If there is a well-defined phase relationship between the states φ_n, we can expect to observe periodic behaviour in the wavepacket on V_1 and therefore in the probability of the transition to V_2. This can be understood quantum mechanically as a consequence of the interference between the populated states;

can also visual

ergy surface.

An observab

ulation of mo

Describe the t

(19a). We ca

ation, *i.e.* d

and is a funct

approximation.

$\frac{\partial^2}{\partial}$

Here $\hbar\omega_{\boldsymbol{q}j} =$

Eden V_{ij} and

Here $\tilde{E}_i(\omega)$ is

we can also visualise a wavepacket as a classical-type particle oscillating on the potential energy surface.

An observable related to the transition efficiency from V_1 to V_2 will depend on the population of molecules in state V_2, *i.e.*

$$I(t) = \left|\langle \psi_1(t) | \psi_2(t) \rangle\right|^2 . \tag{1.12}$$

To describe the time behaviour of the pump-probe signal we therefore require a solution to 1.9 (a). We can assume that the wavepacket does not move significantly during the excitation, *i.e.* $\delta x \ll \lambda$, where λ is the width of the wavepacket at the time of excitation and δx is a function of the duration t_p of the probe pulse. This is the 'frozen wavepacket' approximation.[23] Applying it to 1.9 (a) allows us to ignore the kinetic energy operator and gives[24]

$$\psi_2(\tau) = \frac{i}{\hbar} \int_{-\infty}^{\infty} \exp[i\omega(q)t]\mu_{12}E_2(t)\psi_1(\tau)dt , \tag{1.13}$$

where $\hbar\omega(q) = V_2(q) - V_1(q)$, the coordinate-dependent potential energy difference between V_1 and V_2. Substituting (1.13) in (1.12) gives

$$I(t) = \frac{1}{\hbar^2}\left|\langle \psi_1(t)\| [\mu_{12}(q)]\tilde{E}_2[\omega(q)]\|^2 |\psi_1(t)\rangle\right|^2 , \tag{1.14}$$

where $\tilde{E}_2(\omega)$ is the Fourier transform of the probe electric field:

$$\tilde{E}_2(\omega) = \int_{-\infty}^{\infty} E(t)\exp(i\omega t)dt . \tag{1.15}$$

It can be se

...ly ... only

...ation of tha

...ystem being e

...ed to study.

...al dissociatio

...Vibrationa

When a nu

...e packet wi

...the energy

...efficiently bo

...ond of the r

...Figure 1.1

...ipated for a

...ramp and p

Examinatio

...easily come

...result will

...lower comp

...ings differe

...blood cont

It can be seen from (1.14) that the time dependence in the signal intensity originates from $\psi_1(t)$ only. We can therefore directly relate modulation in signal intensity $I(t)$ to the evolution of the wavepacket on V_1. The method chosen to describe $\psi_1(t)$ depends on the system being examined, the characteristics of the pulses and the type of dynamics we wish to study. Of particular interest to this study are vibrational and rotational dynamics and dissociation processes; a brief discussion of each is presented.

A. Vibrational Dynamics

When a number of eigenstates of V_1 are populated, Equation (1.11) shows that the wavepacket will exhibit periodic behaviour, depending on the population of the states φ_n and the energy differences between them. In the case shown in Figure 1.1, where V_1 is sufficiently bound for the wavepacket to persist in this state longer than a vibrational period of the molecule, it will return to the Franck-Condon region for the excitation to V_2. Figure 1.1 (b) shows the changes in $V_1 \rightarrow V_2$ absorption efficiency that would be expected for a system such as the one shown in Figure 1.1 (a) as the time delay between the pump and probe pulses is varied.

Examination of Equations 1.11 and 1.14 shows that the time dependence in the signal intensity comes from the exponential portion of the wavepacket ψ_1. When this is squared, the result will be a rapidly varying term describing the coherence between V_1 and V_2 and a slower component that oscillates as the cosine of a frequency characteristic of the energy difference between populated levels.[25,26] There will be both vibrational and rotational contributions to this oscillation. In many cases, the different timescale of these

processes allows them to be treated separately. For example, the modulations shown in Figure 1.1 (b) are attributable to vibrational oscillation of the wavepacket on V_1. The slowly varying change in maximum amplitude of each oscillation is a consequence of the rotational dynamics. Neglecting the rotational contribution to the signal for a moment, the vibrational portion of the signal evolves as:[25]

$$I_v(t) \approx 2\sum_{ij} A_{Vij} \cos\left(2\pi c[E_1(v_{1i}) - E_1(v_{1j})]t\right) \tag{1.16}$$

where the constant A_{Vij} contains the non-time varying terms. Equation 1.16 allows vibrational dynamics to be modelled very simply as a sum of cosines. Furthermore, the vibrational spacing yields information about the shape of the potential energy surface.[20,27-29]

B. Rotational Dynamics

When one excites a molecule using a polarised light source, the transition probability depends on the angle between the polarisation of the light and the transition dipole moment in the absorbing molecule. Whether the relevant transition corresponds to a simple electronic excitation to a bound state, or a repulsive state excitation resulting in a chemical reaction, the result will be a population preferentially aligned with the electric field vector of the exciting radiation. Excitation with a polarised source thus produces an anisotropy in the sample, which can be measured using a pump-probe technique by recording time-resolved data with the polarisation vector of the probe pulse aligned either parallel or perpendicular to that of the pump. As with vibrational excitation, the timescale of rotational coherence allows the corresponding excitation to be determined.[12,21,25,30-35]

Equation (1.11) contains contributions from all the populated rovibronic states of V_1; both vibrational and rotational dynamics will therefore be observed. However, if the pump and probe pulses are polarised it is possible to separate the isotropic and anisotropic contributions to the signal. Two sets of experiments are performed; in the first, the probe laser is polarised parallel to the pump and the signal collected at different pump-probe delay times τ. In the second, the process is repeated with the polarisation of the probe laser set perpendicular to the pump. The isotropic contribution to the signal can then be isolated using the following formula:[36]

$$I(t)_{isotropic} = I(t)_{\parallel} + 2I(t)_{\perp} \tag{1.17}$$

where $I(t)_{\parallel}$ indicates the signal intensity with pump and probe polarised parallel to each other and $I(t)_{\perp}$ the corresponding signal for the perpendicular configuration. The time-dependent rotational anisotropy is extracted from the data using the formula

$$r(t) = \frac{I(t)_{\parallel} - I(t)_{\perp}}{I(t)_{\parallel} + 2I(t)_{\perp}}. \tag{1.18}$$

Separation of the signal in this way into isotropic and anisotropic portions allows us to study them independently of each other.

In order to analyse the anisotropic portion of the data, a model must be constructed to describe the time evolution of the molecular alignment.[36] This model was initially constructed by Baskin and Zewail[21] for the case of single photon pump and probe transitions. To illustrate the model, refer to Figure 1.2. If $\hat{\boldsymbol{\varepsilon}}_n$ are the unit electric

polarisation vectors for the laser pulses then from Equation 1.14, the time-dependent signal due to rotational anisotropy can be expressed as[37]

$$I_S(t) = A(t)\left\langle \left|\hat{\mu}_1(0)\cdot\hat{\varepsilon}_1\right|^2 \left|\hat{\mu}_2(t)\cdot\hat{\varepsilon}_2\right|^2 \right\rangle, \tag{1.19}$$

where $\hat{\mu}_1(0)$ and $\hat{\mu}_2(t)$ are unit vectors along the directions of the pump and probe transition dipoles and $A(t)$ contains the isotropic portion of the signal intensity. The $\hat{\mu}_2(t)$ are time-dependent because the molecules are tumbling in space. However, since the pump transition defines the zero of time for the reaction, the pump transition dipoles are denoted as $\hat{\mu}_1(0)$. The angle $\phi_2(t)$ between $\hat{\mu}_1(0)$ and $\hat{\mu}_2(t)$ contains information about the rotational dynamics of interest.

The averages in (1.19) take into consideration the contributions from individual molecules and can be viewed essentially as a summation (or rather average) over a collection of individual molecules. Since the transition dipoles $\hat{\mu}_1(0)$ and $\hat{\mu}_2(t=0)$ (at time zero) are molecule–fixed vectors, they are determined completely if the molecular orientation is specified. The molecular orientation can be characterised, for instance, by the three angles θ_1, ϕ_1, χ_1 defined in Figure 1.2. Here, θ_1 and ϕ_1 define the orientation of $\hat{\mu}_1(0)$ while χ_1 specifies rotation about $\hat{\mu}_1(0)$. The time evolution of the probe dipole $\hat{\mu}_2(t)$ is governed by the angular momentum j of the species being probed. The quantity j is conserved at least until collisions take place; this is a relatively long period of time in a rarefied gas phase experiment. The average over the molecules can be replaced with an average over θ_1, ϕ_1, χ_1 and j as long as the population of the species being pumped with

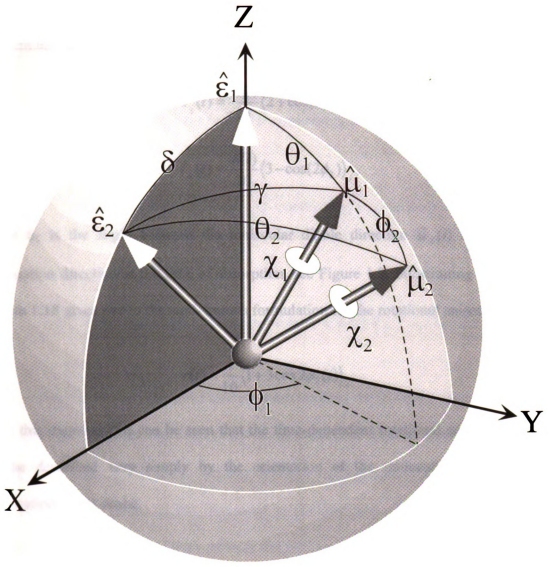

Figure 1.2 Definitions of the polarisation and transition dipole vectors and the angles between them. The space–fixed vectors $\hat{\varepsilon}_1$ and $\hat{\varepsilon}_2$ denote unit vectors along the pump and probe electric polarisation directions, respectively. Rotational dynamics are manifested as the time dependence of the angle ϕ_2 between the molecule-fixed transition dipoles $\hat{\mu}_1(0)$ and $\hat{\mu}_2(t)$. The quantity δ denotes the angle between the pump and probe pulse polarisation; $\delta = 0$ when the probe pulse is polarised parallel to the pump and $\delta = \pi/2$ when it is perpendicular. The remaining angles are averaged out in the derivation of the time dependent rotational anisotropy.

orientation θ_1, ϕ_1, χ_1 and the population of the species being probed with angular momentum j are used as the weights for the average. This yields[37]

$$I_{\parallel}(t) = \frac{A(t)}{15}\left\langle 2+\cos(2\phi_2)\right\rangle_j \qquad (1.20)\ (a)$$

$$I_{\perp}(t) = \frac{A(t)}{30}\left\langle 3-\cos(2\phi_2)\right\rangle_j, \qquad (b)$$

where ϕ_2 is the angle between the molecular dipole direction $\hat{\mu}_2(t)$ and the probe polarisation direction at the time of absorption, see Figure 1.2. Substituting 1.20 (a) and (b) into 1.18 gives rise to the well–known formulation for the rotational anisotropy,[32,36,38]

$$r(t) = \frac{1}{10}\left\langle 1+3\cos 2\phi_2(t)\right\rangle_j. \qquad (1.21)$$

From this expression it can be seen that the time-dependent rotational anisotropy signal can be described very simply by the orientation of the molecules relative to the polarisation of the probe.

To average over the angular momentum j in the above expression, we begin by assuming that the molecule is a symmetric top with axes $\hat{x}$, $\hat{y}$ and $\hat{z}$. The top motion is a composite of two different types of rotation: the nutation of the figure axis about j at a rate $\omega_n = j/i_{\perp}$ and the rotation of the top about its figure axis at a rate $\omega_r = j\cos\theta(1/i_{\parallel} - 1/i_{\perp})$, where $i_{\parallel}$ and $i_{\perp}$ denote respectively the moments of inertia of the molecule about its top axis and about any axis perpendicular to it.[39] If χ_0 is the angle of rotation about the figure axis of the top at time zero and we define an angle θ between

a figure as

a 2D vect

Knowing

ne arbitra

sists $\hat{x}$.

pressions

ates the

a figure as

e be di

the figure

$\hat{x}(t)$.

Applying th

the figure axis and the angular momentum j of the molecule, the equations of motion for the unit vectors along the top axes are as follows:[21]

$$\begin{aligned}\hat{x}(t) = &[\cos(\chi_0+\omega_r t)\cos(\omega_n t)-\cos\theta\sin(\chi_0+\omega_r t)\sin(\omega_n t)]\hat{X}\\ &+[\cos(\chi_0+\omega_r t)\sin(\omega_n t)+\cos\theta\sin(\chi_0+\omega_r t)\cos(\omega_n t)]\hat{Y}\\ &+\sin\theta\sin(\chi_0+\omega_r t)\hat{Z}\end{aligned} \qquad (1.22)(a)$$

$$\begin{aligned}\hat{y}(t) = &[-\sin(\chi_0+\omega_r t)\cos(\omega_n t)-\cos\theta\cos(\chi_0+\omega_r t)\sin(\omega_n t)]\hat{X}\\ &+[-\sin(\chi_0+\omega_r t)\sin(\omega_n t)+\cos\theta\cos(\chi_0+\omega_r t)\cos(\omega_n t)]\hat{Y}\\ &+\sin\theta\cos(\chi_0+\omega_r t)\hat{Z}\end{aligned} \qquad (b)$$

$$\hat{z}(t) = \sin\theta\sin(\omega_n t)\hat{X} - \sin\theta\cos(\omega_n t)\hat{Y} + \hat{Z}\cos\theta\,. \qquad (c)$$

Knowing the time evolution of the unit vectors along the top axes, the time evolution of an arbitrary vector can be predicted so long as its resolution in terms of the top unit vectors $\hat{x}$, $\hat{y}$ and $\hat{z}$ is known. We can therefore use Equations (1.22) to evaluate the expressions in Equations (1.20). We need to consider two simple cases. First, (||, ||) denotes the case where the dipole of both the pump and probe transitions are parallel to the figure axis (z axis) of the molecule at time zero. The second case is where the pump and probe dipoles are perpendicular to each other at time zero and one of them is parallel to the figure axis; this will be denoted by (||, ⊥). For the (||, ||) case, $\hat{\mu}_1(0) = \hat{z}(0)$ and $\hat{\mu}_2(t) = \hat{z}(t)$. Similarly, in the (||, ⊥) case $\hat{\mu}_1(0) = \hat{z}(0)$ and $\hat{\mu}_2(t) = \hat{x}(t)$. This gives[37]

$$\begin{aligned}\cos\phi_2(\|,\|) &= \cos(\omega_n t)\\ \cos\phi_2(\|,\perp) &= -\cos(\chi_0+\omega_r t)\sin(\omega_n t)\end{aligned} \qquad (1.23)$$

Combining these results with (1.21) yields[21,37]

$$r_{\parallel,\parallel}(t) = \frac{1}{10}\langle 1+3\cos(2\omega_n t)\rangle_{j,\theta,\chi_0}$$
$$= \frac{1}{10}\left[1+3\frac{\sum_j P_j \cos(2j\omega_{n0}t)}{\sum_j P_j}\right] \quad (1.24)$$

and[37]

$$r_{\parallel,\perp}(t) = -\frac{1}{5}\langle 1-3\cos^2(\chi_0+\omega_r t)\sin^2(\omega_n t)\rangle_{j,\theta,\chi}$$
$$= -\frac{1}{20}\left[1+3\frac{\sum_j P_j \cos(2j\omega_{n0}t)}{\sum_j P_j}\right]. \quad (1.25)$$

The quantity P_j denotes the rotational distribution of the species probed and the average over χ_0 is assumed to be uniformly weighted. Since $\omega_n t$ depends on j but not on θ or χ_0, only the j average is explicitly carried out in the last step. After such averaging, $\cos^2(\chi_0 + \omega_r t)$, the only χ_0 dependent factor in (1.25), becomes 0.5. To explicitly show the dependence on j, ω_n has been replaced by $j\omega_{n0}$, where $\omega_{n0} = 4\pi B_j$. Notice that the anisotropy in (1.25) is exactly $-1/2$ times that in (1.24). Similar j averages can be carried out for other more complicated cases.

C. Dissociation

When V_1 is repulsive, the pump transition initiates a photodissociation reaction. It is for this application, termed femtosecond transition state spectroscopy (FTS), that pump-probe spectroscopy is particularly useful.[4] As the name implies, the use of FTS to study a photochemical reaction allows one to directly monitor the progress of the reaction as it proceeds through the transition state to products.

Figure 1.

scribed a

ems to ev

ce or all

sonance co

erage of

Classical

ssociation

ally mode

der $V_g(R)$

ger along

excitation

rential. *I.e*

ion of the

ved. Ass

sequence

Figure 1.3 (a) illustrates the process. As discussed already for bound states, the pump is absorbed and produces a wavepacket on the excited potential surface V_1, which then begins to evolve in time. In this case, instead of returning to the Franck-Condon region, some or all of the excited molecules will dissociate. As the reaction proceeds, the resonance condition $\hbar\omega = V_2(R) - V_1(R)$ for the probe pulse will change; we can take advantage of this to determine the reaction dynamics.

Classical mechanical methods[23,40] have been found to be quite effective in explaining dissociation dynamics as observed by FTS.[41,42] In this approach, the repulsive surface is usually modelled as a simple exponential

$$V_1(R) = A_1 + V_1(R_i)\exp\left(-\frac{R-R_i}{L_1}\right), \tag{1.26}$$

where $V_1(R)$ is the potential energy of V_1 when the dissociating fragments are a distance R apart along the reaction coordinate and R_i is the internuclear separation at the moment of excitation by the pump. The parameter L_1 is a measure of the steepness of the potential, *i.e.* how rapidly the molecule proceeds towards dissociation. To determine the motion of the molecule along V_1 as a function of time, a simple impulsive classical model is used. Assuming that the change of potential energy during the reaction is a consequence of conversion to kinetic energy of the dissociating fragments

$$E = V_1(R) + \frac{1}{2}\mu\left(\frac{dR}{dt}\right)^2, \tag{1.27}$$

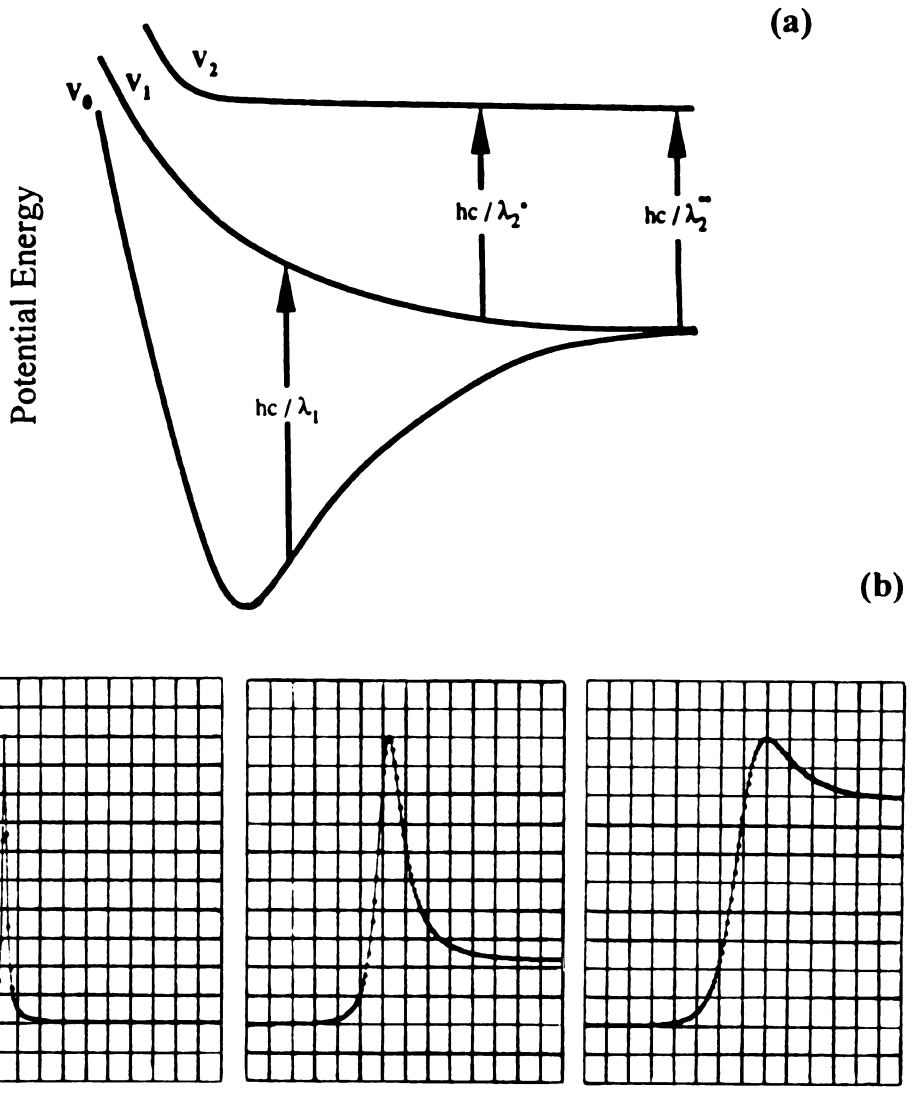

Figure 1.3 Clocking figure.

(a) Potentials involved in clocking experiments. Excitation from V_0 to V_1 by an ultrashort pulse produces a wavepacket on V_1. As the probe is tuned to shorter wavelengths, the wavepacket traverses the optically coupled region for the $V_1 \rightarrow V_2$ transition at greater pump-probe time delays and the transition state more closely resembles the products.

(b) Transients obtained at a range of probe frequencies. When the probe is tuned to be resonant with the transition state immediately after time zero, the signal forms and decays rapidly. As the time taken for the wavepacket to reach the optically coupled region increases, the resonance condition for the asymptotic products is approached and the signal no longer falls to zero.

where μ is the molecular reduced mass and $V(0) = E$. We can relate the terminal velocity v_t of the fragments to the change in potential energy during the reaction, since $v_t = \sqrt{(2E/\mu)}$. Separation of variables and substitution for $V_1(R)$ from Equation 1.26 therefore gives, after integration[43]

$$R(t) = R_i - L_1 \ln\left(\operatorname{sech}^2 \frac{v_t t}{2L_1}\right). \tag{1.28}$$

which allows us to determine $V_1(t)$:[30]

$$V_1(t) = E \operatorname{sech}^2\left(\frac{v_t t}{2L_1}\right). \tag{1.29}$$

If we select the frequency of the probe laser to correspond to the resonance condition at some arbitrary internuclear separation $R > R_i$, the time-dependent signal intensity $I(t)$ affords a direct measure of the reaction dynamics. Figure 1.3 (b) shows typical transients for several values of ω (and therefore R). The signal will initially be zero, then rise to a maximum when the wavepacket traverses the optically coupled region for the probe frequency, falling off again as the molecules proceed to dissociation. If the probe frequency selected is at the asymptotic limit, *i.e.* $\omega = \omega(\infty)$, see Figure 1.3 (a), the resonance will correspond to absorption by one of the fragments; the time taken for the signal to build will therefore yield a dissociation time for the reaction. At intermediate frequencies, the time required to reach each resonance point is determined by the slope of the potential to that point; a series of 'off-resonance' (with the fragments) experiments can therefore be used to map the shape of V_1. If there is a crossing on the potential, a

barrier may be formed as in the case of NaI dissociation, for example;[30,41,44] in this case, the wavepacket will oscillate in the bound portion of the potential with some molecules proceeding to dissociation each time the crossing region is traversed. The effect of this kind of process would be to produce oscillatory behaviour of the type shown in Figure 1.1 (b), superimposed on the clocking transient.

By this method, information about the time required for the reaction to occur, as well as the shape of the reactive PES can be obtained.[30,41,42,44,46-49] Direct probing of the transition state (the 'off-resonance' probing) is of particular significance because it is extremely difficult to examine the processes occurring *during* a reaction by any other method.

D. Bimolecular Reactions

Equation (1.14) can equally be applied to any of the cases we have discussed by application of the right wavefunction $\Psi_1(t)$ and judicious selection of the form of the potential surface. In principle, bimolecular reactions can be investigated by pump-probe spectroscopy in the same way as any other process. In practice, however, they are more difficult to describe and study. This is because in order for a bimolecular reaction to occur, there has to be an interaction between the reacting species. We cannot then simply define 'time zero', the initiation time of the reaction, as the moment at which the pump pulse is absorbed, because there may be a delay between excitation and the time when the molecules come into contact with one another. One approach that has been used to overcome this is to begin with dissociation of a precursor to produce one of the reactants,

which then immediately undergoes a reaction with another part of the precursor to form the product of interest.[48,50-58] Laser-assisted reactions of this type have the advantage of defining both the time zero and geometry of the reactants within a limited range. However, the presence of another species in the complex influences the reaction dynamics,[59-61] and the presence of a bond in the initial complex means that the reaction is not truly bimolecular.

It has been known for some time that two species in close proximity can collectively absorb radiation and both be excited by a single photon.[62-67] Photoassociation occurs if a bond is formed by this process.[2,65-70] Bimolecular reactions can therefore be studied by the pump-probe method if the pump pulse causes photoassociation. In this case, because the bond can only be formed in the presence of the exciting radiation, the initiation time could be defined very precisely without restricting the course of the reaction. This not only allows the observation of dynamics in the resulting product(s) but also enables us to directly measure the time taken for bond formation. There is however a drawback in using ultrashort pulses to study this type of reaction, which is that we are restricted to those reactive pairs that are close enough to each other during the pulse to form a bond. In the case of a pulse having a very short time duration, this means that the number of possible associating pairs could be prohibitively small.

In a photoassociation reaction, the ground state potential surface V_0 is repulsive or weakly binding and can be approximated by a Morse potential with a very shallow well. The difference between this and the excitation of a bound state is that the ground state

wavefunction is a thermal ensemble of scattering states rather than a single eigenfunction of the potential energy surface. Calculation of Franck-Condon factors for the transition from the ground to the first excited state is performed semiclassically.[12,69,70] Once this has been done, Equations 1.1 and 1.5 can be applied to determine $|\psi_1(t)\rangle$, the time-dependent wavefunction on the first excited state V_1. The same methods as in the bound-bound case can then be used to model subsequent dynamics.

1.2.4 Detection

Any detection technique that allows one to observe the efficiency of absorption of the probe is useful. The choice of detection method can therefore be made depending on the characteristics of the system under investigation and the dynamic properties one wishes to investigate. Common methods include fluorescence,[41,45,47] absorption,[71-74] molecular beam and ionisation methods[75-78] and ion photodetachment.[49] Each of these methods relies on a signal intensity that depends on the population of the probe state V_2. In addition, there are scattering-type techniques that do not require absorption of a photon; impulsive stimulated scattering or degenerate four-wave mixing are examples of these.[8-10]

1.2.5 Advantages

There are many advantages to this type of spectroscopy. The high peak intensities associated with short pulses allow multiphoton excitation and other nonlinear optical processes to occur relatively easily, which makes reaction pathways available which might not be accessible otherwise. Microscopic, state-resolved dynamics are probed directly, which circumvents difficulties and the associated errors in converting from PES

calculations to dynamic information.[12] In a similar vein, it is intuitively more logical to think of dynamics in a time-dependent framework than as the Fourier transform of frequency-resolved results. Theoretical modelling of pump-probe experiments is further simplified by the fact that in many cases the wavepacket behaves as a classical particle, as first predicted by Schrödinger[79] and Ehrenfest.[80] It thus becomes possible to describe the time-dependent behaviour of the wavepacket using semiclassical methods; this has been applied very successfully.[14-16,18-22]

Another area of much interest is the control of photochemical reactions; there are many theoretical[12,81-91] and experimental[11,92-97] studies of the problem. Ultrashort pulses are potentially very useful for this purpose for a number of reasons. The short temporal duration is faster than the time scale of most molecular motion, allowing the possibility of reaching a particular state or mode before intramolecular vibrational redistribution (IVR) can occur. Sequences of pulses can thus be used to control the exit channel of a particular reaction.[8,11,82-85] This method becomes even more powerful when combined with the 'tailoring' of pulses by control of phase,[92,93] temporal and/or frequency components[11,85,87-89] and chirp.[88,97,98]

The laser u

ased laser (C

the 514 nm

ative propag

ethoxyborobora

ethoxy fluore

ayers are bet

a continuous

ethoxy relati

remains a satu

Diethyloxa

will be absorb

ransition satur

arget and eas

he gain is sat

Sections will

reduces a syst

uterm collidi

Each trip un

2. LASER SYSTEM

2.1 The Oscillator

The laser used to generate femtosecond pulses is a home-built colliding pulse mode-locked laser (CPM). The heart of this system is a gain dye jet which is optically pumped by the 514 nm line of a continuous wave (cw) Ar^+ laser; broad-band fluorescence from the dye propagates in both directions around a ring cavity. The dye used is rhodamine 6G tetrafluoroborate, a xanthene-type dye which absorbs light between 450 and 550 nm to produce fluorescence over the visible region of the spectrum. Typical Ar^+ pumping powers are between 5.0 and 7.0 W over all lines. The light that is produced in this manner is continuous wave and multimode, each longitudinal mode having a phase that is arbitrary relative to the others. Pulse formation is caused by the second jet, which contains a saturable absorber. This is a dye that has an intensity-dependent absorption; 3,3'-diethyloxadicarbocyanine iodide (DODCI) is used. Light of relatively low intensities will be absorbed, but as the intensity of the incident light increases, the absorption transition saturates and allows some of the light to be transmitted. This is amplified at the gain jet and easily saturates the absorber at the next round trip; the process continues until the gain is saturated. Once this occurs, all the modes allowed by the cavity in both directions will have a maximum in the saturable absorber jet, at the same time. This produces a system of counter-propagating pulses which coincide in time and space, hence the term colliding pulse. The saturable absorber will absorb the leading edge of the pulses on each trip until the dye becomes saturated by the more intense portions of the pulse.

The trailing edge will be chopped at the gain jet, which is also saturated by the intense portions of the pulse; the trailing edge will consequently not be amplified. The net result is a shortening of the temporal width of the pulse and a concomitant spread in the spectrum. Stable operation of the mode-locked laser requires that the intensity at which the gain dye saturates is higher than the intensity required to bleach the saturable absorber. The optimal arrangement is thus to allow the pulses to coincide in the saturable absorber and to be as far away from each other as possible at the gain dye jet. This can be achieved by ensuring that the saturable absorber and gain dye jets are 1/4 of the cavity length away from each other.

The cavity length of the CPM used for these experiments is 3.3 m, which produces a repetition rate of 100 MHz. The light produced by the CPM oscillator is centred at 624 nm and has an average power of 20 mW, which corresponds to 240 pJ per pulse. In order to do spectroscopy, we need higher pulse energies. This requires amplification of the pulses.

2.2 The Amplifier

To amplify the output from the CPM, a dye-based amplifier was constructed; a schematic is shown in Figure 2.1. Light from the CPM passes through four dye cells, which are transversely pumped using light at 532 nm produced by frequency-doubling the output of a Nd:YAG laser. The amplification mechanism is sketched in Figure 2.2. Absorption (a) of a nanosecond pulse at 532 nm excites the gain dye to the S_1 electronic

Figure 2.1
a second
the pump

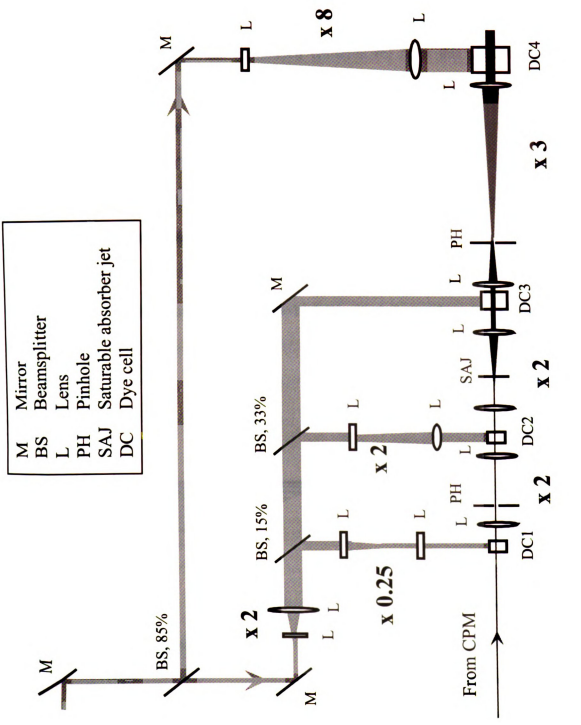

Figure 2.1 Schematic of the amplifier. Four dye cells are transversely pumped by the second harmonic of the Nd:YAG laser. Telescopes are used to expand both the pump and amplified beams.

state; a number of rovibronic levels are excited, which undergo collisional relaxation (b) to lower energy rovibronic levels. Stimulated emission (c) from this state to excited vibrational levels of the ground state amplifies the CPM beam at 624 nm. Because the dye is in solution and has such a large molecular structure, a large number of rovibronic states are accessible to the CPM beam. This is important to ensure that the bandwidth of the amplified beam is not limited by the gain dye. Following stimulated emission, dye molecules eventually relax back down to the ground state.

The Nd:YAG laser is run at 30 Hz and ≈ 10.5 W with 5-7 ns pulses; this corresponds to an average pulse energy of 300 mJ. The flow through the dye cells is such that the dye is completely replaced thirty times a second, so that each pulse of the YAG laser excites a fresh portion of dye. This reduces thermal distortion resulting from heating of the solution by the pumping laser.

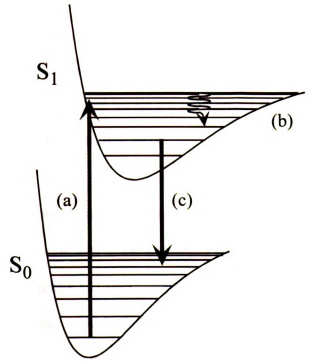

Figure 2.2 Sketch of the amplification mechanism

The dye cells are of the Bethune prism type.[99] This is a standard 45° right angle fused

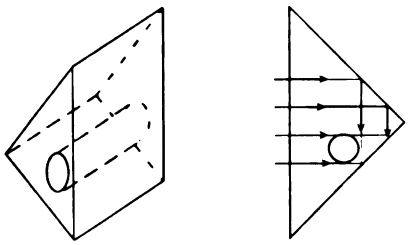

Figure 2.3 Detail of the Bethune cells.

silica prism with a hole drilled through it to allow the dye to circulate, see Figure 2.3. The geometry of these cells is such that light incident on the front (plane) face of the prism is reflected internally so that dye inside the channel is illuminated evenly from all sides. This is advantageous because it minimises distortion in the amplified beam caused by uneven excitation of the gain dye; it also renders the amplifier less sensitive to imperfections in the mode of the pumping laser. The output beam profile is also improved by the use of spatial filters. Two diamond pinholes are used for this purpose; one between the first and second and the other between the third and fourth stages of the amplifier. Diffraction rings from the pinholes are used to help in properly aligning the input beam through the dye cells. Cylindrical lenses are used for all stages except the third to focus the Nd:YAG beam to a line at the dye cells.

The gain dyes used in the amplifier were Kiton red in the first stage and sulforhodamine 590 in the remaining three; in every case, the solvent is water containing 15% Ammonyx LO (lauryldimethylamine oxide). Kiton red is chosen for the first stage because it has a lower absorption at 624 nm than sulforhodamine, which is more suitable for the later dye stages because it minimises distortion due to wavelength-dependent gain.[100,101] Dye concentrations are chosen to give the maximum possible gain at each stage with as little absorption of the femtosecond pulses as possible. If α is the absorption

coefficient in mJ/mm^2 for the pump light and 2r the diameter in mm of the beampath through the dye cell, it was found that a concentration which gives $\alpha r = 1$ is optimum.[99,102]

Spontaneous emission from the dye molecules occurs in the cells; this fluorescence can also be amplified, to produce amplified spontaneous emission (ASE). Because this is not a coherent process, it produces noise in the output of the amplifier and limits the gain. ASE is reduced by ensuring that r « L, where L is the pathlength of the CPM beam through the dye cell,[100,103] and by the use of a saturable absorber jet after the second stage. The saturable absorber acts as a temporal filter in a similar way to the DODCI jet used in the CPM. Malachite green dissolved in ethylene glycol is used, because it has a picosecond absorption recovery time[104] and thus discriminates against the ASE, which has a nanosecond pulsewidth, relative to the femtosecond pulses. Correct synchronisation between the femtosecond and amplifying lasers is necessary to ensure amplification, and is achieved by the use of a photodiode to detect the femtosecond pulses from the CPM. The electronic signal from the photodiode is amplified and used to trigger the Q-switch impulse of the YAG (see Figure 2.4). The time delay between the pulse arriving at the photodiode and the triggering of the Q-switch on the YAG is manually adjusted using a commercial SM-1 unit.

The velocity with which light will propagate through a medium is determined by the frequency-dependent refractive index $n(\omega)$ of the medium. The difference between this velocity and the speed of light in vacuum can be expressed in terms of a phase shift $\phi(\omega)$:

Figure 2.4 Experimental setup. A pulse from the CPM is collected by a photodiode. The Nd:YAG laser is triggered by the amplified pulse from the diode; an SM-1 unit is used to synchronise the pulses. After amplification, the CPM beam is recompressed and steered to a Mach-Zehnder interferometer having a fixed arm and a scanning arm. One arm is frequency doubled, and the two beams are linearly recombined before being focussed into the sample cell. Signal is collected as fluorescence by a monochromator and PMT then averaged in a boxcar before being sent to the computer. The boxcar is also triggered by the CPM.

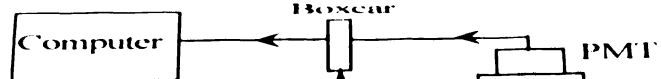
Boxcar
Computer
PMT

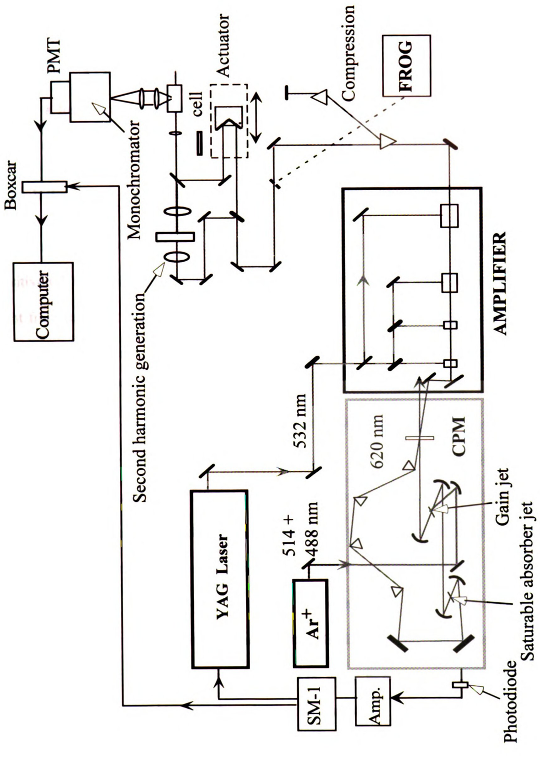
Computer
Boxcar
PMT
Monochromator
Second harmonic generation
cell
Actuator
Compression
FROG
AMPLIFIER
532 nm
620 nm
CPM
Gain jet
Saturable absorber jet
YAG Laser
514 +
488 nm
Ar$^+$
SM-1
Amp.
Photodiode

Figure 2.4

here L is t

vacuum.[43,44]

ill be a fr

thers: this

v_g such tha

GVD may

positive G

ight from

of GVD, c

passes.[43,44]

phenomen

quite signi

amplifier.

lowers the

in the amp

after amp

pulses to

be compe

can introd

At the

$$\varphi(\omega) = -\frac{L}{c}\omega n(\omega), \qquad (2.1)$$

where L is the pathlength of the light through the medium and c the velocity of light in vacuum.[43,105] As the amount of material through which the pulse travels increases, there will be a frequency-dependent phase shift in each frequency component relative to the others; this is termed group velocity dispersion or GVD. If we define the group velocity v_g such that $v_g = \frac{\omega}{\phi'(\omega)}$, where $\phi'(\omega) = \left(\frac{\partial\phi}{\partial\omega}\right)_L$, GVD is produced by non-zero $\phi''(\omega)$. GVD may be either positive or negative; in general most transparent media exhibit positive GVD for visible light, in which the phase shift increases with frequency. As the light from the CPM travels through the amplifier, it will experience a substantial degree of GVD, or chirp, as a result of the large amount of glass and water through which it passes.[43,100,102,104,106] The effect of GVD is to temporally broaden the pulse.[106] The phenomenon becomes more important as the spectral width of the pulses increases and is quite significant for femtosecond pulses, which have a substantial bandwidth. Inside the amplifier, this is actually an advantage because it temporally broadens the pulses and thus lowers the peak intensity, which reduces problems due to high intensity nonlinear effects in the amplifier media. However, a compression stage is necessary to regain short pulses after amplification. A double-pass prism pair arrangement is used, which allows the pulses to be recompressed by introducing negative GVD. However, only linear chirp can be compensated for in this way, so care should be taken to ensure that processes which can introduce nonlinear chirp into the pulses are minimised.

At the high peak intensities inherent with a femtosecond pulse, nonlinear optical

processes be

ead to dist

ehaviour o

ight balanc

ndesirable

To redu

ulses thro

pproximate

n output d

he early st

for exampl

pulses.

an be a pr

ible burnin

ntensities

aser is sele

pulses relat

2.3 Pulsev

The puls

epetition ra

processes become significant. This can be a problem because many of these processes lead to distortion of the beam profile and can affect both the temporal and spectral behaviour of the laser.[43,99-104,106,107] Thus in the design of the amplifier one must strike the right balance between amplification of the pulses and limiting those processes which are undesirable.

To reduce intensity-dependent distortion effects, the amplified beam is expanded as it passes through successive stages of the amplifier. The beam from the CPM has an approximate diameter of 0.75 mm; this is expanded by a factor of 12 in total, resulting in an output diameter of 9 mm. Relatively low intensities of pumping laser are incident on the early stages of the amplifier to reduce nonlinear frequency generation mechanisms, for example self-phase modulation (SPM), which also cause nonlinear chirp in the pulses.[100,104] This has the further advantage of reducing gain saturation in the dyes, which can be a problem because it limits the gain and distorts the pulse profile, through spectral hole burning for example.[104] As the beam becomes larger in diameter, greater pump intensities can be used. In the last stage of the amplifier, the intensity of the pumping laser is selected so as to saturate the gain dye; this renders the intensity of the output pulses relatively insensitive to fluctuations in the power of the Nd:YAG laser.

2.3 Pulsewidth

The pulses produced from the amplifier typically have a power of 8 - 12 mW; at a repetition rate of 30 Hz, this corresponds to ≈ 300 μJ per pulse, an amplification factor of

ij. This is

nsideratio

spersive n

ecompress

GVD: a pri

angemen

here d is t

ght travels

To ensu

mporal an

this is a ma

determined

purpose.

Frequen

nonlinear op

dispersing a

and time:

10^6. This is more than adequate for most spectroscopic measurements. There is another consideration, however; the temporal width of the pulses. GVD introduced by the dispersive media of the amplifier may broaden them to as much as 600 fs. In order to recompress the pulses we must compensate for this broadening by introducing negative GVD; a prism pair is used, in the arrangement shown in Figure 2.4. For this type of arrangement, the expression for ϕ'' is as follows:[108]

$$\phi_p'' = \frac{4\lambda^3}{\pi c^2}\left\{-dn'^2 + L\left[\frac{nn''}{1+n^2} + n'^2\left(1 - \frac{1}{n^2(1+n^2)}\right)\right]\right\} \tag{2.2}$$

where d is the distance between the prisms at the apices and L is the amount of glass the light travels through.

To ensure proper recompression of the amplified pulses and to determine their temporal and spectral width, a frequency resolved optical gating (FROG) system is used; this is a method by which the spectral and temporal intensity profile of a pulse can be determined in a single shot.[109,110] A Clark-MXR FRG-1 system was purchased for this purpose.

Frequency resolved optical gating takes advantage of the instantaneous response of a nonlinear optical medium to the intensity of light incident on it. The method works by dispersing an autocorrelation trace, thus producing a trace of intensity versus frequency and time:

$$I(\omega,\tau) = \left|\int_{-\infty}^{\infty} E(t)g(t-\tau)\exp(-i\omega t)\,dt\right|^2, \tag{2.3}$$

Bea

Figu

where $E(t)$

delay.

Figure 2.5

significant

as to be at

a cylindric

plate is us

produced:

quartz, thus

probe beam

rotated by

will be an

each positi

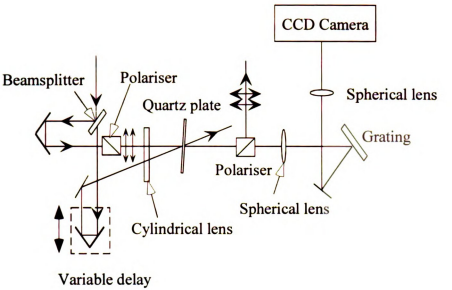

Figure 2.5 Schematic of the frequency resolved optical gating (FROG) system.

where $E(t)$ is the electric field of the incident pulse and $g(t-\tau)$ is a gate pulse with variable delay.[109,110] The Clark system uses a polarisation grating effect; a schematic is shown in Figure 2.5. The beam is split into pump and probe pulses, with the pump being significantly more intense than the probe. The polarisation of the probe beam is rotated so as to be at 45° relative to the polarisation of the pump. Each beam is then focussed using a cylindrical lens and overlapped in a second-order nonlinear optical medium (a quartz plate is used). When the pulses coincide in space and time, an optical Kerr effect is produced; the pump pulse produces an anisotropic change in the refractive index of the quartz, thus rotating the polarisation of the probe.[111] A second polariser in the path of the probe beam is crossed with the first so that only the portion of the light field that was rotated by the quartz plate is transmitted. Because each beam is focussed to a line, there will be an intensity autocorrelation across the medium produced by the delay between each position on the line. This encodes temporal pulse information horizontally.

sbsequen

bequency

me to dete

ases for

shown in F

(a

λ

Figure
negative
chirped
prism P2

properly a

CPM and a

Subsequent dispersion of the autocorrelation trace produces a spectrogram with frequency information encoded vertically. The result is the FROG trace, which allows one to determine the time-dependent frequency profile of the input pulses. Typical FROG traces for Gaussian pulses which are unchirped and positively and negatively chirped are shown in Figure 2.6.

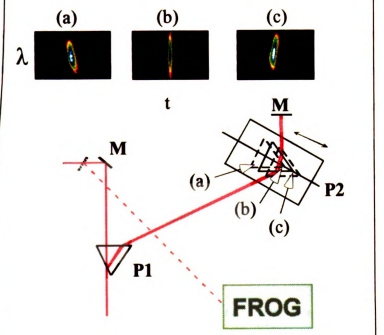

Figure 2.6 Typical FROG traces, showing (a) negatively chirped, (b) unchirped and (c) positively chirped pulses. The chirp is altered by translating the prism P2 across the beam as shown.

By this method, the degree of chirp remaining in the pulses after recompression can be monitored; linear chirp is compensated for by lateral translation of one of the compression prisms. A certain amount of nonlinear chirp may also be present; this cannot be compensated for in a simple fashion, but with a properly adjusted oscillator and amplifier will be minimal. The pulses produced by our CPM and amplifier setup are typically approximately 60 fs in duration.

2.4 Exp

After

arrangem

flow va

moveable

collinear

a second

sample co

laser. Det

boxcar li

spectrogr

250 nm.

be detec

2.4 Experimental Setup and Detection

After recompression, the beam is steered to a Mach-Zehnder interferometer arrangement (see Figure 2.4). A beamsplitter is used to divide the beam intensity; to allow variable pathlength, a portion of the light is sent to a retroreflector mounted on a moveable platform. The other beam traverses a fixed path and the two beams are then collinearly recombined. If necessary, one or both beams can be frequency doubled using a second harmonic generation (SHG) crystal. The overlapped beams are focused into a sample cell and the fluorescence produced is collected perpendicular to the path of the laser. Detection is performed by a monochromator and PMT and the signal collected by a boxcar linked to the computer. The spectrometer used is a SPEX 270M imaging spectrograph with two gratings, one with a blaze wavelength at 630 nm and the other at 250 nm. The appropriate grating is selected depending on the wavelength of the signal to be detected.

3.1 Intr

3.1.1 Pho

Photo

he form

roductio

from CH

involved

of two e

ype of p

ground-b

mention

they proc

3.1.2 Co

Multi

stepwise

kinetic st

not

the poten

or not m

plateau o

3. PHOTOINDUCED MOLECULAR DETACHMENT

3.1 Introduction

3.1.1 Photoinduced Molecular Detachment

Photoinduced molecular detachment occurs when photolysis of a molecule results in the formation of another molecule as one of the fragments. Examples include the production of H_2 from photolysis of CH_3NH_2,[112] H_2O and H_2CO molecules[113] and IBr from CH_2IBr.[114] Unlike most photodissociation processes, where only one bond is involved, molecular detachment (also called concerted elimination) requires the breaking of two existing bonds in addition to the formation of a new one. Understanding of this type of process thus represents an interesting and challenging area of research. Since the ground-breaking work of Woodward and Hoffmann on pericyclic reactions,[115] much attention has been focussed on these reactions, particularly the mechanisms by which they proceed.[116-121]

3.1.2 Concerted Reactions

Multibond reactions can be divided into two categories; sequential (also called stepwise) and concerted. A reaction is defined as concerted if it proceeds via a single kinetic step, whether the bond breaking and formation processes are simultaneous or not.[115-117,119] However, since little is commonly known about the transition state region of the potential energy surface in many reactions, it is difficult to determine *a priori* whether or not more than one kinetic step is involved in a given reaction. The existence of a plateau or local minimum in potential energy along the reaction coordinate would

however be expected to result in formation of a species intermediate in some respect between reactant(s) and product(s). For this reason, a reaction is defined as concerted if it proceeds without forming a stable intermediate. In general, reactions which have an experimentally observable intermediate are considered to be non-concerted, *i.e.* stepwise. This observation may be direct, the appearance of a transient fluorescence for example, or it may be indirect, as in the measurement of fragment scattering angles and momenta from molecular beam experiments.

In order for a photodissociation reaction to be concerted, a number of conditions must obtain. The excitation must be in a restrictive Franck-Condon region to ensure that the parent molecules have a narrow spread along the reaction coordinate and move in phase as the reaction is initiated. The repulsive potential must be somewhat uncoupled from the rest of the molecule and the excitation energy sufficiently high above threshold to prevent redistribution of energy between other modes during dissociation. It is to be emphasised that concerted reactions are not necessarily simultaneous, *i.e.* bond breaking and/or formation processes may not all progress at the same rate. The important factor is that each fragment proceeds along a potential energy surface that is purely repulsive with respect to the parent molecule. Although many reactions are thought to be concerted, few have been unequivocally demonstrated to be so.[i]

The reaction of interest to this study is the molecular detachment of a halogen

[i] Exceptions include the elimination of molecular hydrogen from 1,4-cyclohexadiene[120] and from H_2S.[121]

olecule fr

here X a

thakalkar

rmation i

Most of th

form methy

and then ex

3.1.3 Meth

The spe

ssation o

ncerned

ates, $^{2}D_{3/2}$

ground $^{2}P_{3/2}$

The possibl

1. Although

wavelength

wavelengths

molecule from a dihaloalkane:

$$RCHXY + h\nu \rightarrow RCH + XY,$$

where X and Y are halogens. Molecular photodetachment of halogen molecules from dihaloalkanes has been investigated in several systems.[113,114,122-128] In general, molecule formation is observed only at high excitation energies and is usually a minor channel. Most of these studies have specifically examined the molecular photodetachment of I_2 from methylene iodide (CH_2I_2).[113,122-127] We will begin with a discussion of this molecule and then examine its analogues.

3.1.3 Methylene Iodide

The spectroscopy and photodissociation of CH_2I_2 have received a great deal of attention over the past two decades or so.[72,124-126,128-141] Most of these studies are concerned with the photodissociation dynamics of low–lying excited electronic states,[72,129-139] which dissociate to produce CH_2I and I fragments with I in either its ground $^2P_{3/2}$ state or its spin–orbit excited $^2P_{1/2}$ state.

The possible photolysis products of CH_2I_2 and corresponding energies are shown in Table I. Although it is thermodynamically possible to form I_2 when CH_2I_2 is excited at any wavelength below 333 nm,[132,133,135] this product has only been observed for excitation wavelengths in the range 125 - 200 nm.[122-125,133]

Table I. Pho

Channel
1
2
3
4
5
6
7
8
9

Upon h

and I_2, *i.e*

electronica

showed tha

its maximu

the mean

formation

emitting a

in the 18(

addition to

Table I. Photodissociation reaction pathways of CH_2I_2.[130]

Channel	Products	Energy Required (eV)	cm^{-1}
1	$CH_2I + I\ (^2P_{3/2})$	2.22	17,900
2	$CH_2I + I^*\ (^2P_{1/2})$	3.17	25,600
3	$CH_2(\tilde{X}\ ^3B_1) + I\ (^2P_{3/2}) + I\ (^2P_{3/2})$	4.94	39,800
4	$CH_2(\tilde{X}\ ^3B_1) + I\ (^2P_{3/2}) + I^*\ (^2P_{1/2})$	5.88	47,400
5	$CH_2\ (\tilde{a}\ ^1A_1) + I_2\ (X\ ^1\Sigma_g)$	3.72	30,000
6	$CH_2\ (\tilde{b}\ ^1B_1) + I_2\ (X\ ^1\Sigma_g)$	4.60	37,100
7	$CH_2\ (\tilde{X}\ ^3B_1) + I_2\ (A\ ^3\Pi_u)$	4.84	39,000
8	$CH_2\ (\tilde{X}\ ^3B_1) + I_2\ (B\ ^3\Pi_u)$	5.33	43,000
9	$CH_2\ (\tilde{X}\ ^3B_1) + I_2\ (D'\ ^3\Pi_{2g})$	8.4	67, 750

Upon high energy excitation, CH_2I_2 undergoes molecular detachment to yield CH_2 and I_2, *i.e.* $CH_2I_2 \rightarrow CH_2 + I_2^{\bullet}$.[122-126] The iodine molecule produced is highly electronically excited and fluoresces in the 340 nm region of the spectrum. Black[126] showed that the 340 nm fluorescence, which is due to the I_2 $D' \rightarrow A'$ transition, reaches its maximum intensity within 10 ns of excitation, which is considerably less than 50 μs, the mean collision time under the experimental conditions. This suggests that I_2 formation is a primary event. When CH_2I_2 was irradiated with a Kr resonance lamp (emitting at 116.5 nm and 123.6 nm), Okabe *et al.*[124] observed weak fluorescence bands in the 180–240 nm (I_2 $H \rightarrow X$), 250–300 nm (I_2 $F \rightarrow X$) and 450–500 nm regions in addition to the dominant $I_2(D' \rightarrow A')$ fluorescence between 290 and 345 nm. The

quantum yield for the strongest I_2 fluorescence was measured to be less than 1%.[124,126] The 250–300 nm and the 450–500 nm fluorescence systems were found to be at least another order of magnitude weaker than the 290–345 nm fluorescence, while the 180–240 nm fluorescence is the weakest of all.[124]

I_2 fluorescence resulting from two–photon excitation of CH_2I_2 at 248 nm as obtained by Fotakis *et al.*[125] revealed a completely different intensity pattern, with the F $\rightarrow$ X fluorescence being the strongest. The two photon absorption was thought to cause a two – electron excitation of CH_2I_2.[125] Fotakis *et al.* also observed extensive fragmentation of CH_2I_2, leading to the formation of CH and C fragments.

The results of a study of the molecular detachment of a halogen molecule from dihaloalkanes will be presented. Femtosecond pump-probe methods were used in an attempt to elucidate the mechanism and dynamics of this reaction.

3.2 Experimental

All experiments were performed on neat vapour (~ 0.1 – 10 Torr) of the relevant alkyl halide in a static quartz cell. The cell is comprised of a bulb, which is used as a reservoir for the condensed phase of the sample of interest, and a tube 2-4" in length, which has flat windows and acts as the laser interaction region. After samples have been loaded, the cell can be attached to a vacuum line for evacuation and then closed off using a Teflon-sealed Kontes tap. When necessary, cold baths were used to lower the vapour pressure of the sample. Copper or dehydrated sodium thiosulphate were used as scavengers to

prevent the accumulation of molecular halogens. The pump pulse for these experiments was the 312 nm second harmonic of the amplified CPM, which initiated the reaction by multiphoton excitation of the sample vapour. The dissociation products were detected by fluorescence. Spectra were recorded under excitation with 312 nm pulses only, and calibrated with Hg lamp emission. The 624 nm pulse at the fundamental of the CPM was used to deplete the population of halogen molecules in the fluorescent state. This acts as a probe of the temporal evolution of the reaction; sweeping the delay between pump and probe pulses thus allows a transient which reflects the time-resolved dynamics of the reaction to be collected. For each sample, the intensity of the probe beam was attenuated to the point at which no fluorescence could be detected when only the probe beam was incident. At each pump-probe time delay, signal is collected for ten laser shots; pulses that have an intensity greater than one standard deviation from the mean are discarded. Typical transients contain data from two hundred time delays and are averages of a hundred scans.

3.3 Results and Discussion

3.3.1 Methylene Iodide

The dispersed fluorescence spectrum resulting from multiphoton excitation of CH_2I_2 at 312 nm is presented in Figure 3.1. Most of the spectral features can be assigned to fluorescence from nascent halogen molecules resulting from photodissociation of the parent. The principal fluorescent product is iodine in the D' state, which is an ion-pair state, *i.e.* it correlates to $X^+ + X^-$.[142-147] This is consistent with frequency-resolved studies

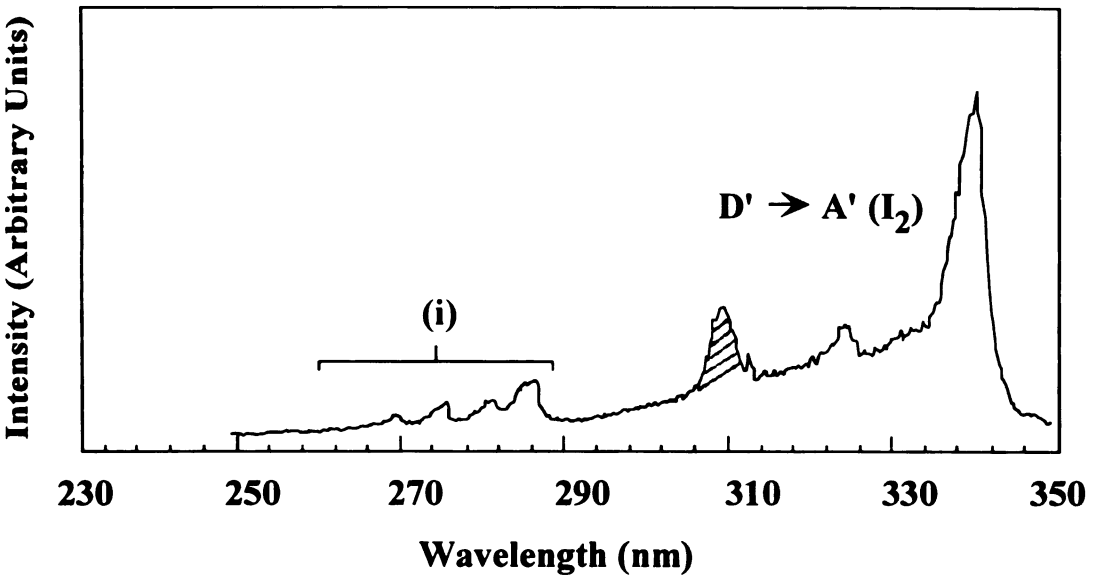

Figure 3.1 Dispersed fluorescence spectrum of I_2, produced by multiphoton dissociation of CH_2I_2 at 312 nm. The dominant fluorescence is between 290 and 350 nm and can be assigned to the I_2 D' → A' transition. A small amount of laser scatter is detected at 312 nm (shaded). The region marked (i) indicates fluorescence produced by other ion-pair states of I_2 (see text). The fluorescence intensity has not been corrected for detection efficiency of the spectrometer.

of photodissociation at high energies.[122-125] The D' state of homonuclear halogens is optically inaccessible from the ground state, but the D' → A' fluorescence is commonly observed when I_2 is excited in the presence of buffer gases.[142-144,148] Under these circumstances the D' state is populated by collisional relaxation from other ion-pair states; this process is very efficient. However, for the current experiments the pressure in the reaction cell is ~ 1 Torr. This precludes the possibility of forming I_2(D') by collisional relaxation, since the time between collisions at this pressure is ≈ 130 ns, which is much longer than the fluorescence lifetime of other ion-pair states (~ 10 ns).[149] In addition, under experimental conditions a collisional formation process would produce a rise time on the order of 100 ns. The observed signal had a very rapid (< 10 ns) rise time and was collected with a boxcar integrator having a 50 ns gate.

Fluorescence Intensity (Arb.)

Figure 3.2 shows dispersed fluorescence spectra of the I_2 D' $\rightarrow$ A' transition; the spectra were all produced by photoinduced molecular detachment of I_2 from CH_2I_2 in a static cell by multiphoton excitation at 312 nm. The 290 – 350 nm portion of the ambient temperature spectrum, as presented above (Figure 3.1), is displayed in Figure 3.2 (b). In order to verify that the observed vibrational distribution in the D' state is produced directly from the reaction and is not a consequence of collisional relaxation in the cell, the same spectrum was also recorded at 0 °C, and is shown in Figure 3.2 (a). To obtain this spectrum, the bulb containing liquid CH_2I_2 was kept in an ice bath but the laser interaction region was at ambient temperature, as before. The result of this is to lower the

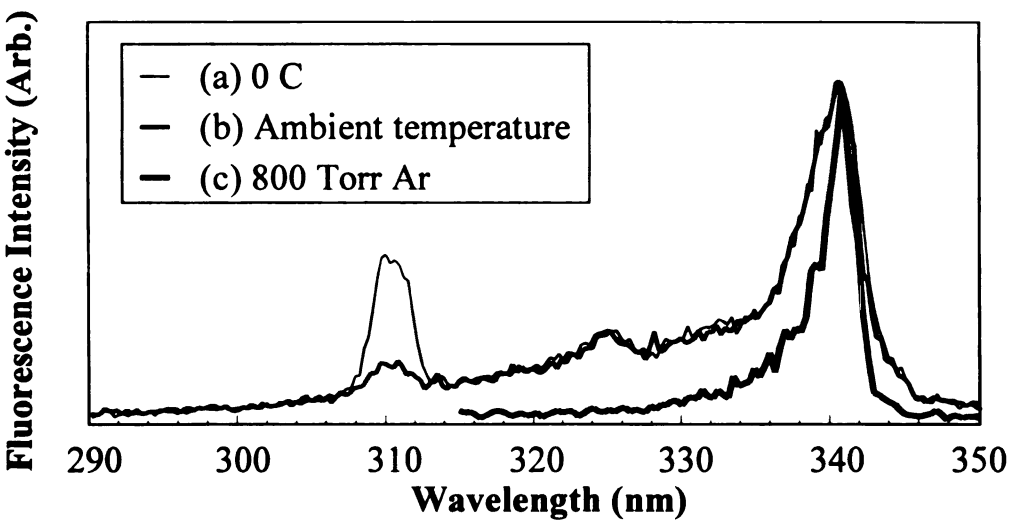

Figure 3.2 Dispersed fluorescence spectra of the D' state of I_2. The spectra were produced by photoinduced molecular detachment of I_2 from CH_2I_2 in a static cell by multiphoton excitation at 312 nm. The spectra are normalised and calibrated, but not corrected for detection efficiency of the spectrometer.

(a) Spectrum recorded at 0 °C.

(b) Ambient (room) temperature spectrum at 1 Torr.

(c) Ambient temperature spectrum in the presence of 80 Torr of Ar.

CH_2I_2 vapour pressure in the cell to ≈ 0.2 Torr while retaining the same energetics of reaction. Comparison of Figure 3.2 (a) and (b) reveals that the spectra are very similar; we can therefore conclude that there is a negligible amount of collisionally induced vibrational relaxation in the I_2 (D') molecules after formation. The D'→ A' spectrum that would be produced by collisionally relaxed molecules was also recorded; Figure 3.2 (c) shows the dispersed fluorescence obtained from a sample of CH_2I_2 in 80 Torr of Ar at ambient temperature. The high pressure in this cell is expected to produce a Boltzmann population of vibrational states in the D' electronic state of I_2. It is clear from Figure 3.2 (b) and (c) that the I_2(D') population resulting from the photodissociation of CH_2I_2 can not be represented by a Boltzmann distribution, *i.e.* is non-statistical. This is important because it indicates that molecule formation is a primary process, rather than the result of secondary bond formation produced by (for example) collisions in the cell.

The spectrum in Figure 3.1 also exhibits fluorescence bands between 250 and 290 nm; the integrated intensity of the fluorescence in this region relative to the 290 - 350 nm region is approximately 10 %. The $f\left(^3\Pi_{0g}^+\right) \rightarrow A\left(^3\Pi_{1u}\right)$,[150] $F\left(^1\Sigma_{0u}^+\right) \rightarrow X\left(^1\Sigma_{0g}^+\right)$,[150] $f'\left(^1\Sigma_{0g}^+\right) \rightarrow B\left(^3\Pi_{0u}^+\right)$,[151] $g\left(0_g^-\right) \rightarrow {}^3\Pi\left(0_u^-\right)$[150] and $G(1_g) \rightarrow A(1_u)$[150] transitions of I_2 fluoresce in this region. Okabe *et al.* also observed fluorescence between 250 and 300 nm and tentatively assigned it to the F → X transition.[124] The assignment of the states responsible for this signal will be discussed in detail later.

Time-resolved dynamics of the molecular photodetachment of I_2 from CH_2I_2 have been recorded and analysed, both in the 290 - 350 nm region corresponding to the D' → A' fluorescence and in the 250 - 290 nm region. These results are discussed separately.

A. The 300-350 nm Region; D'→A'

To confirm that the observed fluorescence does not originate from background I_2 in the cell, time resolved data of the signal at 340 nm was recorded for two cells, each containing CH_2I_2 or I_2. Figure 3.3 shows the situation for the I_2 cell. When I_2 absorbs a photon of energy 2 eV (provided by the 624 nm pulse), it is excited to the B state, as shown in Figure 3.3 (a). Absorption of an additional 4 eV from the 312 nm pulse causes excitation to the ion-pair states E and $f(0_g^+)$. These states have strongly fluorescent transitions to the $A(1_u)$ and $B(0_u^+)$ states; the transient obtained by detecting the 340 nm fluorescence from the f → B transition is shown in Figure 3.3 (b).

Because ground state I_2 does not absorb at 4 eV, no fluorescence signal is observed from the iodine cell when the 312 nm pulse arrives first (negative time). As the pulses become overlapped in time (time zero), the ion pair states are populated and the fluorescence begins to appear. At positive times (624 nm pulse arriving first), modulation in the signal intensity can be seen as the pump-probe time delay is scanned. This is a Franck-Condon effect caused by vibrational oscillation of the wavepacket prepared by the 624 nm pulse on the potential energy surface of the B state, as discussed in Chapter 1.

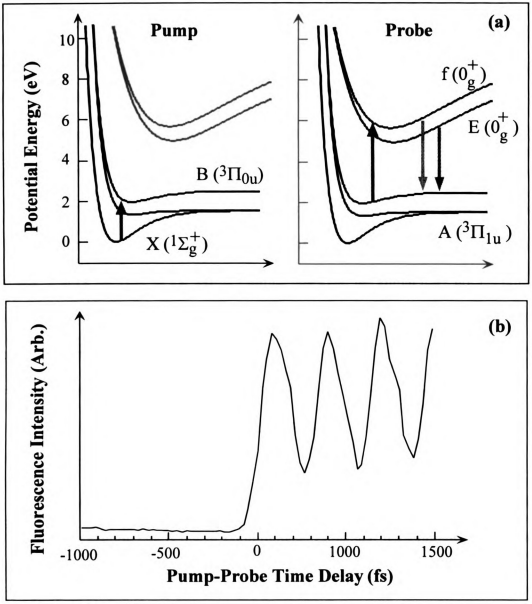

Figure 3.3 Excitation scheme and corresponding time-resolved (pump-probe) data for neat iodine vapour, showing how the observed transient is generated.

(a) A 624 nm (pump) pulse excites I_2 to the B state; subsequent absorption of a 312 nm pulse causes transition to the E and f ion-pair states. These have strong, bright transitions to the valence states A and B. The detected signal is f → B fluorescence at 340 nm.

(b) At negative times (probe pulse arriving before pump), neither the E nor f state is reached and no signal is observed. As the pulses become overlapped in time, it becomes possible to access the f state and molecular fluorescence is obtained. At positive times, vibrational coherence characteristic of I_2(B) is observed.[33]

By contrast, examine the transient produced from the CH_2I_2 cell, shown in Figure 3.4 (b). The pump pulse at 312 nm causes the parent molecule to dissociate, producing $I_2(D')$, which is the source of the fluorescence signal. At negative times (624 nm pulse arriving first), I_2 has not yet formed when the probe pulse arrives and a constant signal level is observed. At time zero, the signal from the CH_2I_2 sample shows significant enhancement in fluorescence intensity; this effect is not observed in the I_2 cell. At positive times, the 624 nm (probe) pulse depletes the population of the D' state, causing a drop in signal intensity. Unlike the case of the iodine sample, however, the signal does not become zero when the 312 nm pulse arrives first; it is simply at a lower level. Figure 3.4 (b) also clearly shows vibrational coherence in the I_2 fragment after photodissociation of CH_2I_2. Note that for the I_2 vapour cell, vibrational modulation is observed only when the 624 nm pulse precedes the 312 nm pulse, while in the CH_2I_2 cell the opposite is the case.

It is clear from the comparisons above that the I_2 fluorescence signal being produced from the CH_2I_2 sample is a result of photoinduced molecular detachment of I_2 molecules and not background iodine in the cell.

The observation of modulations at positive times in the intensity of the D' $\rightarrow$ A' fluorescence is very significant. The period of the oscillations is $\approx$ 300 fs, which corresponds to a vibrational period of I_2 in the D' state.[142,143,152] This is important because it indicates that a vibrationally coherent wavepacket remains in the nascent iodine product after dissociation; the observed modulations are due to oscillation of this wavepacket on the PES of the D' state. The initial coherence induced in the parent

Figure 3.4 Excitation scheme and corresponding time-resolved (pump-probe) data for CH_2I_2, showing how the observed time-dependent fluorescence is generated. (I. P. refers to the ionisation potential of the molecule).

(a) Initially, the molecule undergoes multiphoton absorption of the 312 nm (pump) pulse. This causes it to dissociate, producing I_2 in the D'($^3\Pi_{2g}$) state, which undergoes a fluorescent transition to A' ($^3\Pi_{2u}$), detectable at 340 nm.

(b) Absorption of a 624 nm (probe) pulse by the iodine depletes the population of the D' state. Depletion efficiency tracks the progress of the reaction and is monitored by detecting the D'→ A' fluorescence at 340 nm. Note that the probe transition may not be as represented; there are a number of optically accessible I_2 states 2 eV from the D' state.[170,148] At negative times (probe pulse arriving first), the fluorescence produced by the D' → A' transition is unaffected by the probe, and remains at a constant level. As the pulses begin to overlap in time, an intense enhancement is observed; this is due to a cooperative multiphoton effect (see text). At positive times, absorption of the 624 nm (probe) pulse depletes the population of the D' state, and the fluorescence intensity decreases. Observation of vibrational modulation in the depletion signal indicates that a coherent wavepacket is generated in the D' state of I_2. Note that for the I_2 transient, positive time corresponds to the 624 nm pulse arriving at the cell first; for the CH_2I_2 sample positive time is when the 312 nm pulse arrives first.

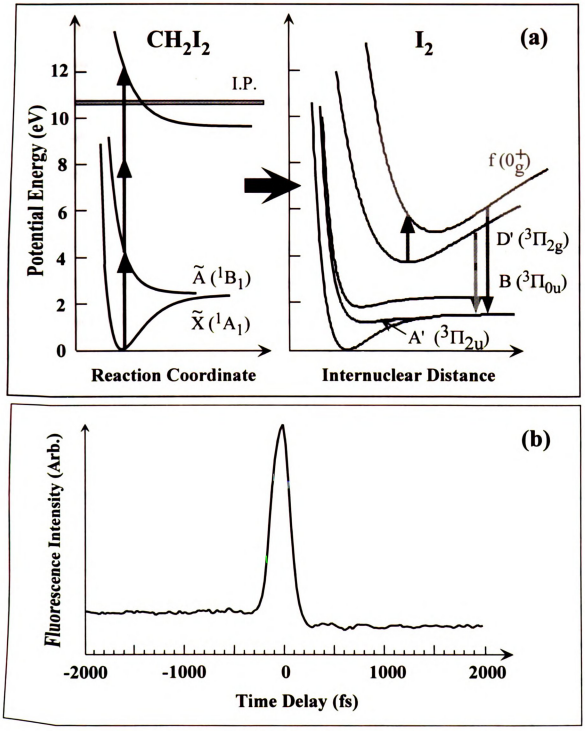
CH2I2
I2
(a)
I.P.
Potential Energy (eV)
12
10
8
6
4
2
0
f (0g+)
D' (3Π2g)
B (3Π0u)
Ã (1B1)
X̃ (1A1)
A' (3Π2u)
Reaction Coordinate
Internuclear Distance
(b)
Fluorescence Intensity (Arb.)
-2000
-1000
0
1000
2000
Time Delay (fs)

Figure 3.4

molecule can only survive in this way if the nascent product molecules vibrate in phase, *i.e.* they must be formed within a short time of each other (the limit is a vibrational period) and on the same region of the reactive PES. Intermediate formation or redistribution of energy during the reaction would disrupt this coherence, preventing the observation of vibrational modulations in the signal. This phenomenon therefore indicates that the dissociation reaction is concerted.

Figure 3.5 shows pump-probe data collected at 340 nm from the CH_2I_2 cell, along with a fit to the observed vibrational dynamics. The pump and probe lasers were polarised parallel to each other. The vibrational modulation dephases quickly and does not seem to recur (see Figure 3.3), so it was decided to fit the data using a damped sinusoidal function of the form:

$$A + Be^{-t/\tau}\cos(\omega t + \phi) \tag{3.1}$$

where A and B are experimentally determined parameters, τ is the dephasing time, ω the vibrational frequency and ϕ the phase. The exponential factor accounts for the effective dephasing of the vibrational coherence and the cosine factor describes the signature of the vibrational motion. The data shown in Figure 3.5 were fit using this model and were found to have an oscillation frequency of 92.2 cm^{-1}, corresponding to a vibrational period of 362 fs. This is the oscillation period of an iodine molecule in v = 28 of the D' state. Fourier transform analysis of the same data revealed a major contributing frequency at 97.7 cm^{-1}, less than 6 % from the fit result. The dephasing time from the sinusoidal fit was $\approx$ 1 ps, which is also corroborated by the Fourier transform.

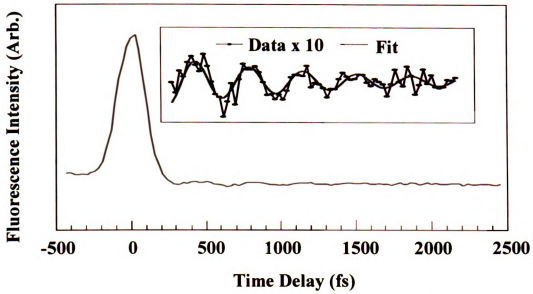

Figure 3.5 Time-resolved data and vibrational fit to the D' → A' fluorescence at 340 nm and positive times. The data was collected with the probe laser polarised parallel to the pump and fit to a function $A+Be^{-t/\tau}\cos(\omega t+\phi)$. The fit displayed was obtained with an oscillation frequency ω of 92.2 cm^{-1}, corresponding to a vibrational period of 362 fs. The dephasing time τ was ~ 1 ps.

The theoretical models of wavepacket propagation discussed in Chapter 1 (see Equations 1.9 particularly) apply only to the case where the probe pulse does not overlap the pump. They are unable to describe the processes that occur when pump and probe pulses coincide. The situation in this case is far more complicated and the simplifying assumptions used in Chapter 1 are not valid. When pump and probe pulses are incident on a system at the same time, coherence effects occur.[8] Additionally, the intense radiation present in the time zero region causes a number of other nonlinear effects, such as coupling of electronic states by the electric field and cooperative multiphoton absorption.[153] These effects are only possible before the fragments have separated, so when they are observed they can be used to determine dissociation time. Figures 3.4 (b) and 3.5 show that the 340 nm fluorescence signal from the CH_2I_2 cell shows a large enhancement at time zero. This is of interest both because it can be used to yield

information about the electronic structure of the parent molecule and because it affords a measure of the lifetime of the transition state for the molecular photodetachment reaction. When pump and probe pulses coincide, the CH_2I_2 molecules absorb 312 nm photons and 624 nm photons simultaneously, which leads to an enhancement in the fluorescence signal if it opens up another reaction pathway for the production of $I_2(D')$. We need to consider possible causes of the observed enhancement.

Since the threshold for production of $I_2(D')$ from the photodissociation of CH_2I_2 is 9.4 eV[124,126] and the energy of a 312 nm photon is 4 eV, multiphoton absorption is required to produce the observed fluorescence signal. Reliable power dependence measurements for high order nonlinear processes of this type are inherently difficult because of the necessity for a wide dynamic detection range and because these types of processes can easily become saturated. However, absorption of two photons of 312 nm light is equivalent to an excitation of 8 eV, which is below the thermodynamic threshold for this reaction. Absorption of four photons, on the other hand, provides 16 eV of energy, which is well above the ionisation potential of this molecule. Three-photon excitation is therefore the most likely and the ensuing discussion is written assuming that this is the case.

Figure 3.6 shows a schematic of the possible excitation schemes that can lead to enhancement of the time zero fluorescence signal. The decay time of the time zero fluorescent enhancement is directly related to the lifetime of the initial excited state of the parent molecule accessed by the pump transition (which we will call the pump-excited

state). The molecular dynamics are manifested as an asymmetry in the time zero peak; the decay time (on the positive side of time zero) is slower than the rise time. This allows us to determine an upper limit for the lifetime of the pump-excited state. It should be noted that the pump – probe data at time zero measure the statistical lifetime of the pump-excited state, not the time taken to reach a particular region of the potential energy surface. This data thus contains no direct information about the exit channel dynamics, but can be used to measure an upper limit for the dissociation time of the molecules.

In order to have the observed effect, the process responsible for the fluorescence enhancement must be of the general type shown in Figure 3.6, *i.e.* one or more 312 nm (pump) photons causes a transition to an excited electronic state. Subsequent absorption of 624 nm (probe) photons produces CH_2I_2 in a sufficiently high energy state to produce $CH_2 + I_2$ (D'). There are a number of possibilities for this excitation scheme; the case when the transition state of the photoinduced molecular detachment reaction is accessed by a three-photon pump transition is shown in Figure 3.6.(c). However, other excitation processes are also possible at time zero. If the initial excitation is provided by absorption of one 312 nm photon, it requires three photons of 624 nm light to reach 10 eV, above the observed threshold for production of I_2 in the D' state;[124] four (plus the initial one photon at 312 nm) provides the same energy as three photons of 312 nm light. This is shown as scheme (a). In either case, the state being probed is 4 eV above the ground state; observed molecular dynamics would give the statistical lifetime of this state. On the other hand, Figure 3.6 (b) shows the situation if the pump-excited state is reached by two pump

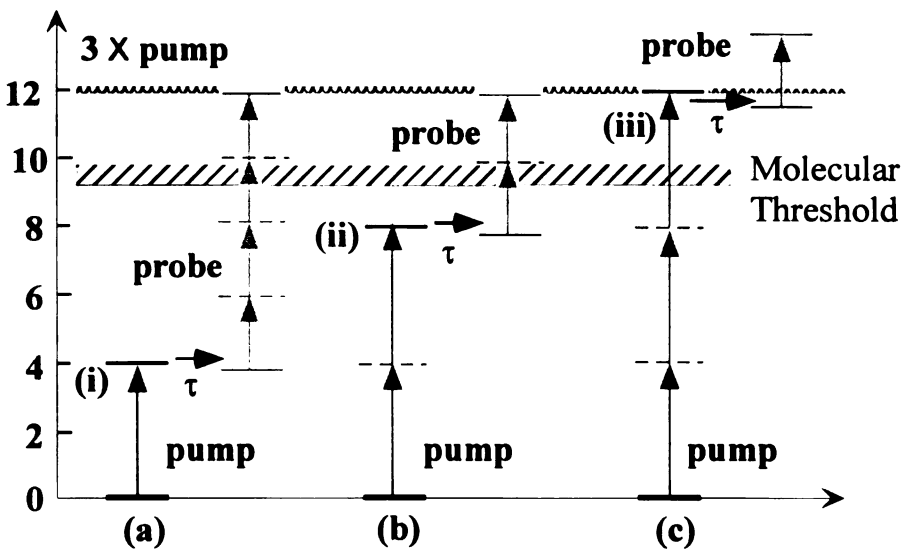

Figure 3.6 Possible excitation schemes to produce time zero fluorescence enhancement. The threshold indicated is the observed excitation threshold for production of CH_2 and $I_2(D')$. The upper line on the figure corresponds to 12 eV, the excitation energy corresponding to a three-photon pump transition.

(a) One photon excitation with the 312 nm (pump) pulse requires three photons of 624 (probe) nm light to reach the threshold for production of $I_2(D')$. An additional photon of the probe produces an excitation of 12 eV. Single-photon absorption at 312 nm is equivalent to an excitation of 4 eV, which is sufficient to reach the $\tilde{A}$ ($^1B_1$) state of CH_2I_2 (marked (i) in the Figure).

(b) An initial absorption of two pump photons corresponds to an excitation of 8 eV, requiring one photon of 624 nm light to reach the threshold and two to be equivalent to an excitation of 12 eV. The pump-excited state, marked (ii), is unknown.

(c) A three-photon pump corresponds to an initial excitation of 12 eV. This is the pathway of the most interest to us because the dynamics observed between the pump and probe pulses correspond to the transition state of the photoinduced molecular detachment reaction. The state (iii) is the dissociative state under investigation.

photons. There are again two possibilities; a one-photon probe transition will exceed the threshold for production of I_2 (D'); a two-photon probe transition accesses the same state that is reached by three photons at 312 nm. If this were the excitation scheme, the lifetime of the state 8 eV above the ground state would be reflected in the molecular dynamics. The scheme shown in Figure 3.6 (c) represents pump excitation to the state of CH_2I_2 that we wish to examine. The lifetime of this state is probed by excitation by the 624 nm pulse to a higher energy state.

We have observed a significant enhancement to the fluorescence at time zero even for quite low intensities of 624 nm pulses. This implies that the scheme shown in Figure 3.6 (a) is probably not a likely alternative, since it requires at least three 2 eV photons to be absorbed as the probe. Scheme (c) would allow the lifetime of the transition state to be determined; scheme (b) would yield molecular dynamic information characteristic of the lifetime of another electronic state than the one of interest. We cannot determine at this time which is more likely. However, it should be noted that because we are measuring an upper limit for the dissociation time, the process that produces the depletion signal cannot be slower than the dissociation time measured using the transition state dynamics.

In order to analyse the transition state dynamics of the reaction, a kinetic model was constructed for the behaviour of the fluorescence signal as a function of delay time between the pump and probe pulses. Figure 3.7 illustrates the model. The observed transient can be modeled as the sum of two contributions. The molecular detachment signal (a) will exhibit a step at time zero due to depletion by the 624 nm pulse. The time

zero fluorescent enhancement (b) can be represented as a Gaussian - type peak decaying exponentially at positive time.

Figure 3.7 (a) illustrates the depletion signal. Three photons of 312 nm light are absorbed by CH_2I_2, which causes the molecule to dissociate, producing I_2 in the D' electronic state. Detection of fluorescence from the D' $\rightarrow$ A' transition at 340 nm allows reaction dynamics to be probed by monitoring the amount of D' state population depleted by a second femtosecond pulse at 624 nm. When the 624 nm (probe) pulse arrives before the 312 nm (pump) pulse (negative time), it does not affect the intensity of the fluorescence. Since it is the nascent product that is being probed, depletion starts to become possible once the probe pulse arrives after the molecules have formed, in other words once the delay time between pump and probe pulses is sufficient for dissociation to have occurred in the meantime. We have assumed that this begins to happen at time zero, *i.e.* when the pulses are overlapped in time. Assuming a delta function pulse, if the molecular response were instantaneous the result would be a step function. To model the dissociation time, the step function is multiplied by an exponential decay. This produces a constant signal at negative times, followed by a gradual drop in signal level beginning at time zero as depletion becomes possible. To account for the temporal width of the pulses, this function is convoluted with a Gaussian; the resulting curve is shown in Figure 3.7 (a).

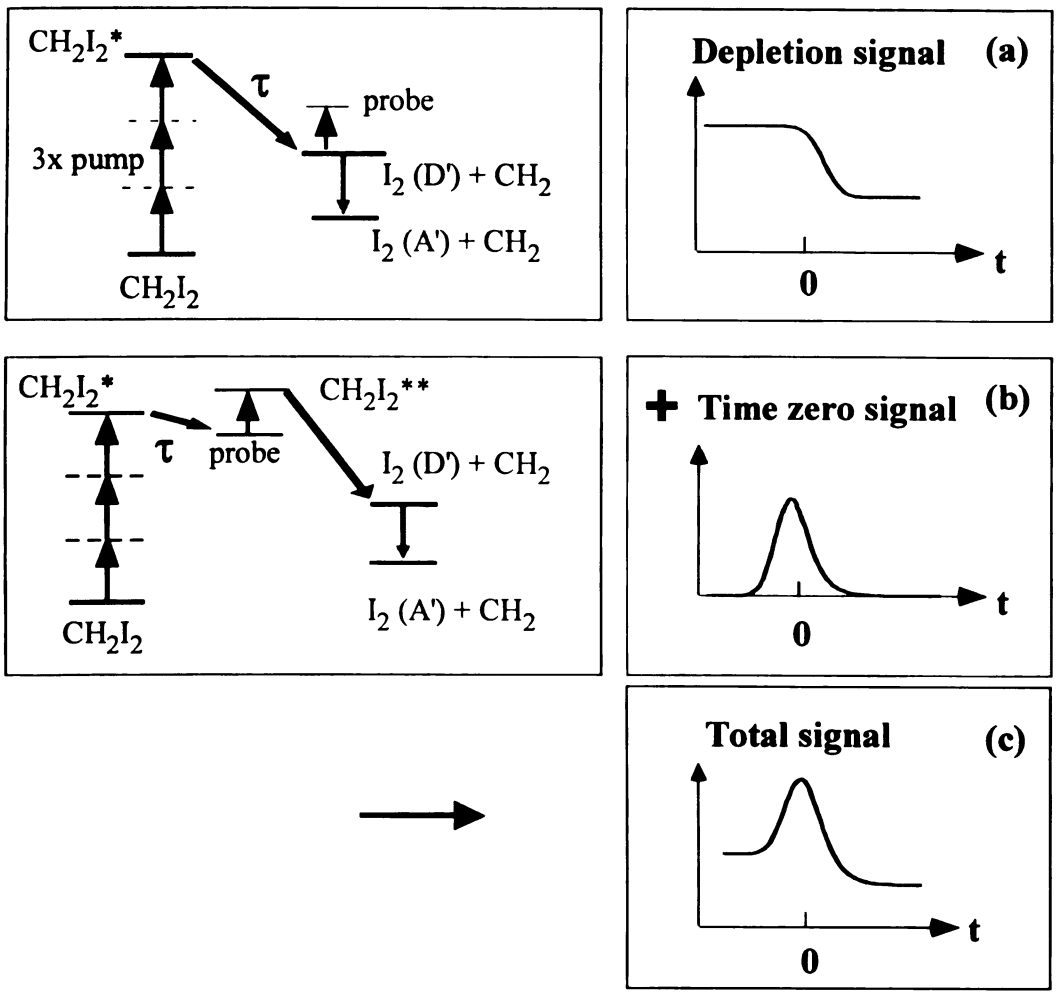

Figure 3.7 Kinetic model for the dissociation of CH_2I_2. The model assumes that the signal is comprised of two contributions:

(a) Depletion signal, produced by the molecular detachment process. Excitation of CH_2I_2 with three photons of 312 nm light produces an excited molecule, which dissociates into CH_2 and I_2(D'). Depletion of the D' fluorescence with a 624 nm pulse probes the dynamics of formation of I_2(D').

(b) Time zero signal. When the pump and probe pulses coincide, it is possible for CH_2I_2 to absorb probe photons prior to dissociation, which produces a highly excited parent molecule. This increases the amount of D' → A' fluorescence observed because it opens another pathway for production of I_2(D'). The statistical lifetime τ of the pump-excited state determines for how long after the initial excitation the molecule can absorb the probe.

(c) The overall signal is a weighted sum of these two contributions, each of which is convoluted with a Gaussian to simulate the pulsewidth.

To model the intense time zero feature, a similar approach was used. In this case, there is no signal at negative times. When pump and probe pulses coincide, a cooperative (multiphoton) effect occurs and fluorescence is produced. As with the depletion process discussed above, we have assumed that this occurs at time zero and that the point at which signal levels reach their maximum value corresponds to time zero. As the time delay between pump and probe pulses increases, the molecules begin to dissociate and the multiphoton signal enhancement is no longer possible. Thus the time zero feature can be represented as a half exponential function; no signal at negative times, then a step to maximum signal levels at time zero, followed by an exponential decay. Again, this is convoluted with a Gaussian to account for the temporal pulsewidth; the result is shown in Figure 3.7 (b). The overall signal should then behave as a weighted sum of contributions from the depletion and time zero features as shown in Figure 3.7 (c). For simplicity, variations in the signal caused by rotational and vibrational motion of the nascent products were not included. The model does not take into account the possible presence of other states, but should provide a reliable upper limit on dissociation time for a given pulsewidth. The details of the mathematical formulation are included in Appendix A.

In order to better understand the factors affecting dissociation time, pump-probe data were obtained to measure the dissociation time of methylene iodide CH_2I_2 and 1,1-diiodobutane $C_3H_7CHI_2$. The results are shown in Figure 3.8. Both transients were taken with the polarisation vector of the probe laser aligned parallel to the pump. The data were fit using a non-linear least squares procedure and the model described above. The dissociation time of $C_3H_7CHI_2$ was found to be $\tau \leq 87 \pm 5$ fs, indicating that molecular

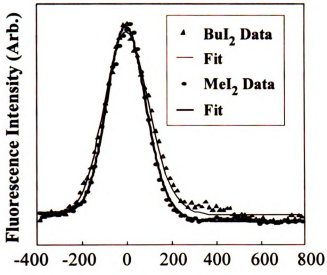

Figure 3.8 Time-resolved data of the molecular photodetachment of I_2 from CH_2I_2 and n-$C_4H_8I_2$. The difference in dissociation time between the two molecules can be accounted for by the difference in mass of the alkyl fragment. The relatively poor fit to the $C_4H_8I_2$ dynamics at positive times is due to the presence of a vibrational oscillation at early times.

detachment is prompt. Fitting of the CH_2I_2 time zero transient using the same method produced a dissociation time $\tau \leq 47 \pm 3$ fs. If there is some redistribution of energy occurring during the reaction, we would expect the effect to be substantially greater in the larger molecule, both because the larger reduced mass allows more time for any redistribution to occur and because there is a greater density of vibrational states in the molecule, allowing for more efficient intramolecular coupling. If we assume that the products of each reaction have the same amount of kinetic energy and that the difference in dissociation time is caused only by the difference in reduced mass μ, we can use the following relationship to predict the expected difference in dissociation time:

$$\left(\frac{\tau_{MeI_2}}{\tau_{BuI_2}}\right) = \sqrt{\frac{\mu_{MeI_2}}{\mu_{BuI_2}}}. \qquad (3.2)$$

Based on the reduced mass of each molecule, this expression yields $\tau_{MeI2}/\tau_{BuI2} = 0.538$. The observed ratio obtained from the fit is 0.54 ± 0.08. Thus the difference in

dissociation time can be completely accounted for by the mass difference, *i.e.* there appears not to be a significant intramolecular redistribution of energy occurring during dissociation even for a system like gem-diiodobutane in which there is a moderately large density of states.

To estimate the amount of available energy that is partitioned into center–of–mass translational motion of the fragments we use τ as an upper limit for the dissociation time of each molecule. For the purposes of the model, we will assume τ to be the time taken for the fragments to move a distance L apart, at which point dissociation will be considered to be complete. The amplitude of the C – I stretch is $\approx$ 1 Å, so it is reasonable to assume that the carbon-iodine bonds are completely broken once the fragments have moved more than 2 Å away from the equilibrium distance. A simple impulsive model can then be employed to estimate the translational energy E of the fragments by assuming that they reach terminal velocity instantaneously:

$$E = \frac{1}{2}\mu\left(\frac{L}{\tau}\right)^2 \tag{3.3}$$

where μ is the reduced mass of the carbene and I_2 moieties, assuming they form a pseudodiatomic (essentially the mass of the alkyl fragment). Using this expression and a length parameter of L = 2.0 Å and a dissociation time τ of 47 fs, the total kinetic energy of the fragments produced by dissociation of CH_2I_2 is estimated to be 1.26 eV.

Analysis of the rotational excitation in the nascent product molecules is also of value, both to determine the partitioning of energy in the fragments and to help elucidate

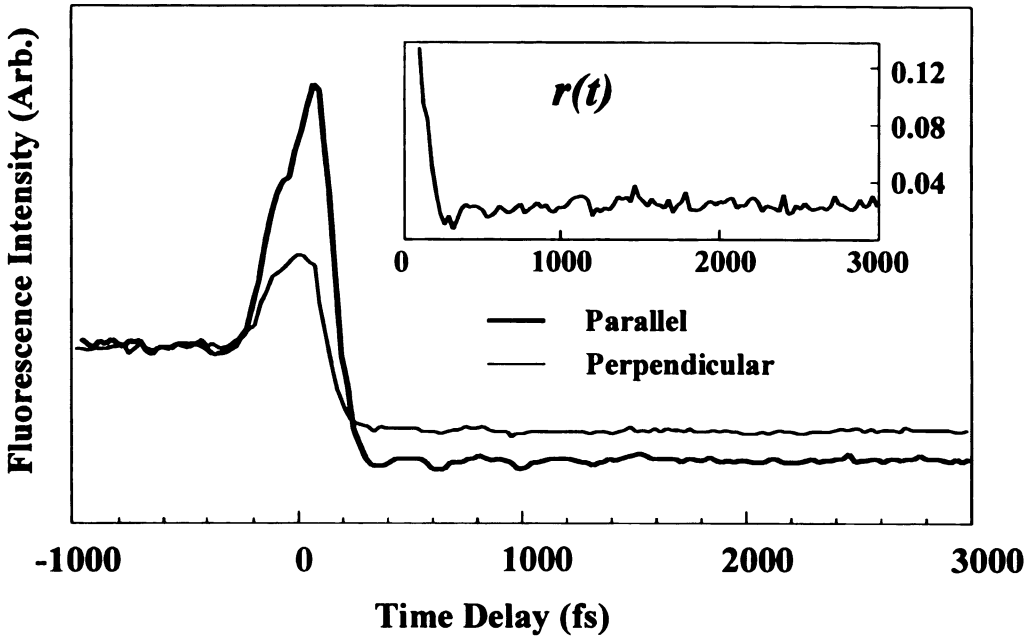

Figure 3.9 Time-resolved data of the CH_2I_2 dissociation obtained at 340 nm with parallel (a) and perpendicular (b) configurations; 'parallel' and 'perpendicular' refer to the polarisation of the probe beam relative to the pump. Note the much smaller intensity of the time zero feature in the perpendicular polarisation configuration. The anisotropy data is ambiguous; no reliable conclusions about the rotational population of the products can be drawn from analysis of this data.

the reaction mechanism. For this reason, the anisotropic contribution to the signal was extracted using the formula[36]

$$r(t)=\frac{I_{\parallel}-I_{\perp}}{I_{\parallel}+2I_{\perp}}, \tag{3.4}$$

where $\parallel$ and $\perp$ denote the polarisation of the probe laser relative to the pump and I represents the intensity of the fluorescence at each pump-probe time delay. Figure 3.9 shows transients obtained from the CH_2I_2 cell when the probe laser was polarised parallel (a) and perpendicular (b) to the pump. The purely anisotropic contribution to the signal $r(t)$ is shown as an inset. Unfortunately, the anisotropy signal is on the same scale as the noise, so it isn't possible to obtain reliable information about the rotational dephasing

time of the molecules from the extracted r(t). This may be because the rotational dephasing occurs very rapidly and is buried under the time zero feature, or there may be such a long, slow dephasing that it is difficult to observe. The fact that time zero enhancement is greater when the 624 nm pulse is polarised parallel to the 312 nm pulse than when it is perpendicular further confirms that this feature is due to a co-operative process.

B. The 250 – 290 nm Region

As with the D'→A' fluorescence, time resolved data was obtained in this region by multiphoton dissociation with femtosecond pulses at 312 nm to produce molecular iodine in a fluorescent ion-pair state. A probe pulse at 624 nm then allows the reaction and nascent product dynamics to be monitored by depletion of this state. Figure 3.10 shows transients recorded at two wavelengths in this region; 285 nm and 272 nm. The dynamic data collected at 340 nm indicated that the molecular halogen detachment from CH_2I_2 is extremely fast. Examination of the transients shown in Figure 3.10 also demonstrates the promptness of the dissociation process. The rapid onset of the depletion at 272 nm and of decay in the time zero signal at 285 nm both show that the reaction is essentially instantaneous within the time resolution of the pulses (≈ 50 fs). Both transients exhibit fluorescence depletion and vibrational coherence at positive times, but whereas the 285 nm data has a large time zero enhancement, the 272 nm data does not. Additionally, there is no discernible anisotropy in the fluorescence detected at 285 nm but a substantial degree in the 272 nm channel (*vide infra*). These differences reveal that the fluorescence

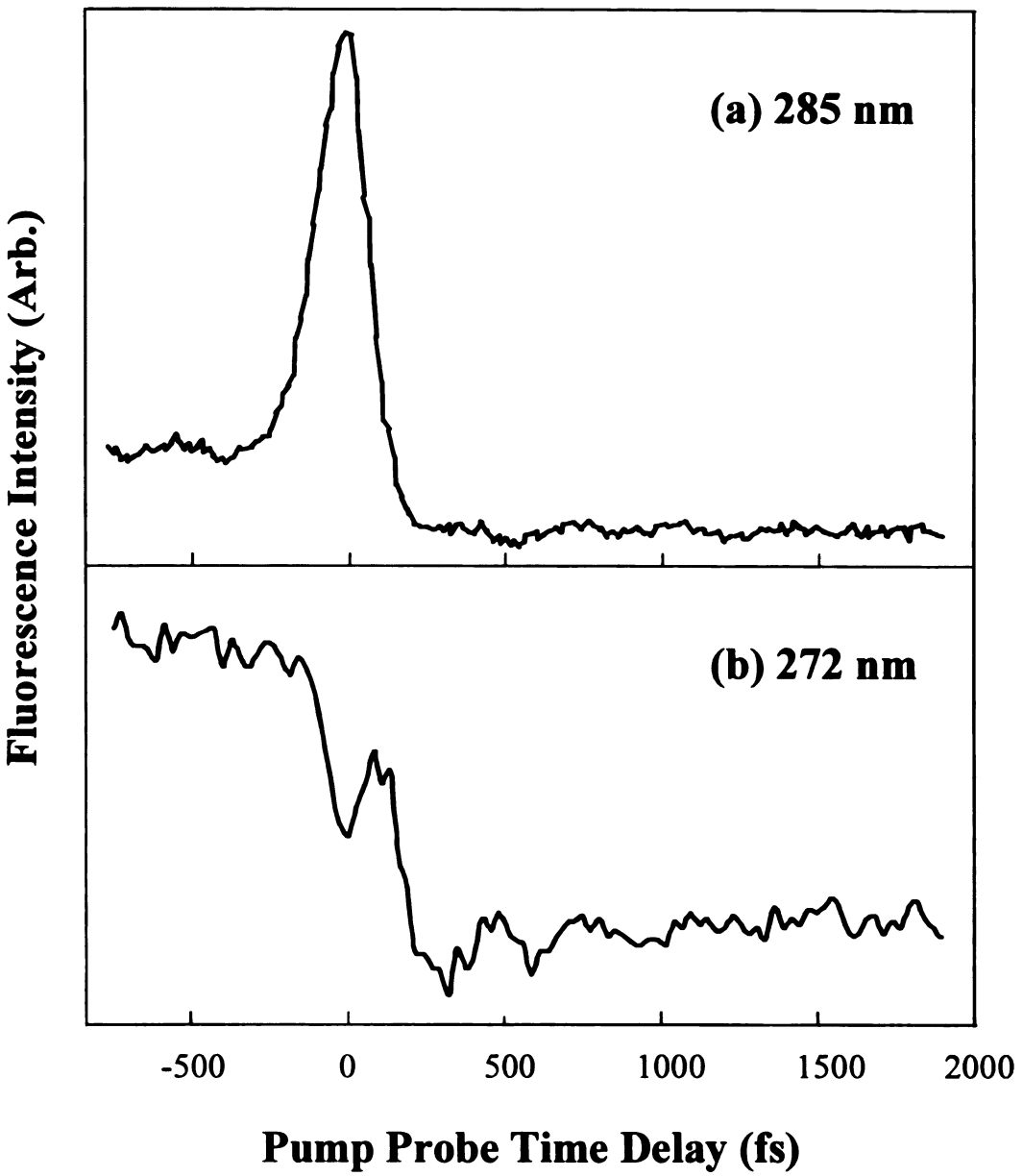

Figure 3.10 Pump-probe data obtained by selective detection of the I_2 fluorescence signal at 285 nm (a) and at 272 nm (b). Both transients were obtained with the pump and probe beams polarised parallel to each other. Both exhibit vibrational coherence. However, the 285 nm transient exhibits a large time zero spike and the 272 nm transient does not.

between 250 and 290 nm originates from at least two electronic states of molecular iodine and is being formed by two distinct reaction pathways. In the section below, the time-dependent signal at 272 nm will be analysed.

Figure 3.11 shows time-resolved data of the molecular detachment of I_2 from CH_2I_2 detected at 272 nm. The data are recorded with the probe polarised parallel (a) and perpendicular (b) to the pump. As with the time-resolved data obtained at 340 nm, vibrational coherence can be seen in the data. Unlike the 340 nm data, however, there is a substantial difference between the two transients. This is caused by alignment of the molecules in the gas phase. Those parent molecules that have a transition dipole aligned with the polarisation vector of the laser will undergo reaction, producing a nascent product population selectively aligned in a particular direction. The ability of the probe pulses to deplete the newly-prepared fluorescent state then depends on the orientation of its polarisation vector relative to that of the pump pulse. As the molecules rotate, the probability of the probe transition will therefore vary as a function of time delay between pump and probe. Figure 3.11 indicates that there is a large degree of anisotropy in the formation of the product molecules detected at 272 nm. The anisotropy decays very rapidly, within $\approx$ 500 fs of time zero. Note also that the depletion efficiency immediately after time zero is greater when the pump and probe pulses are polarised perpendicular to each other than when they are parallel. This is somewhat counterintuitive and indicates that the pump and probe transitions are perpendicular to each other. The fast decay implies a high degree of rotational excitation in the I_2 fragment.

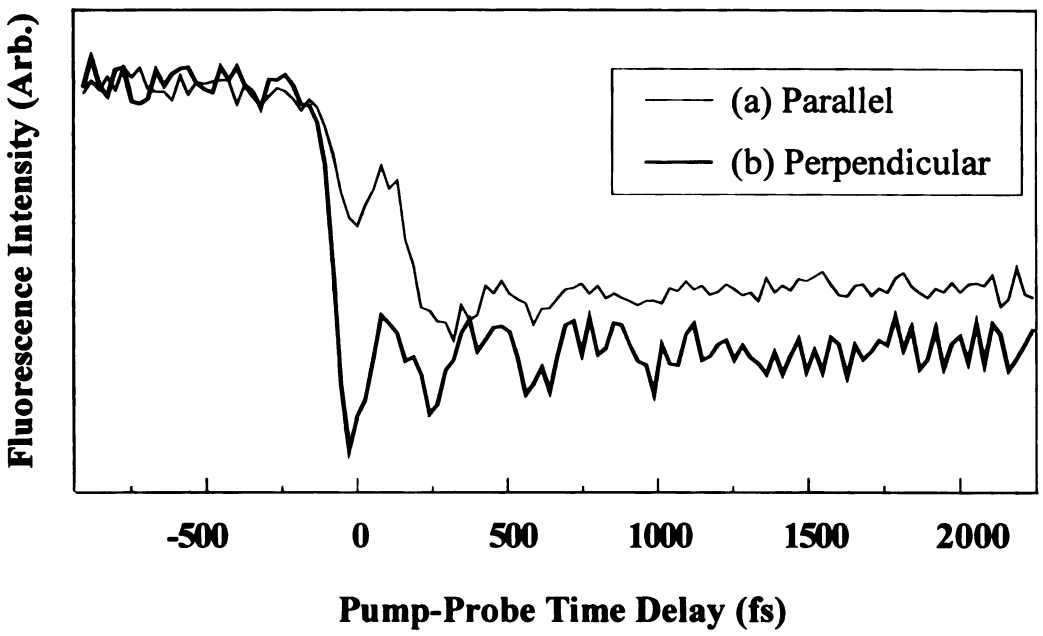

Figure 3.11 Time-resolved data at 272 nm of the CH_2I_2 dissociation, obtained with the probe polarised parallel (a) and perpendicular (b) to the probe. The difference between the two transients clearly indicates rotational anisotropy in the I_2 product. Notice both the rapid anisotropy decay time and the fact that depletion is more efficient immediately after time zero in the perpendicular polarisation configuration.

The time-dependent rotational anisotropy is extracted from the data using the form of (3.4) above; the isotropic component of the signal is likewise extracted from the data using

$$I_{\text{isotropic}} = I_{\parallel} + 2I_{\perp}. \tag{3.5}$$

Isolation of the data in this way into isotropic and anisotropic contributions allows us to analyse the rotational and vibrational dynamics of the nascent molecules separately. Presented in Figure 3.12 (a) and (b) are respectively the purely anisotropic and isotropic contributions derived from the 272 nm transients shown in Figure 3.11.

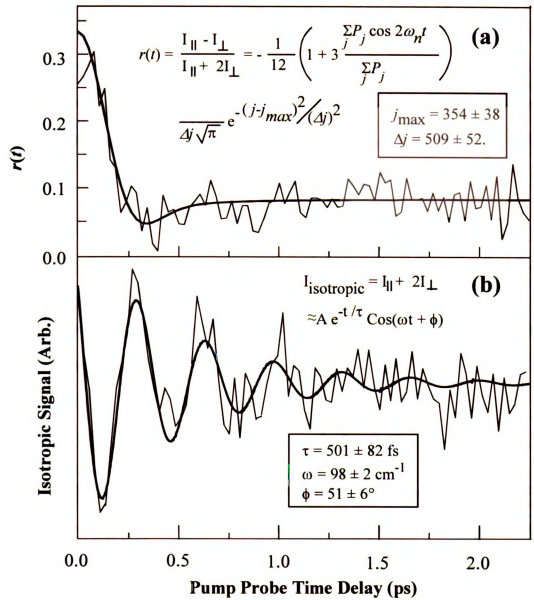

Figure 3.12 Purely isotropic and anisotropic components of the time-resolved data presented in Figure 3.11.

(a) The pure rotational contribution as given by the time dependent rotational anisotropy $r(t)$.

(b) The pure vibrational contribution as given by the isotropic signal $I_{\parallel} + 2I_{\perp}$.

The thicker lines show least–squares fits to the pure vibrational and pure rotational contributions.

A quantitative analysis of the rotational dephasing in the 272 nm data can be performed on the purely anisotropic contribution presented in Figure 3.12 (a). A formulation of time–dependent rotational anisotropy for the case of one–photon pump and one–photon probe has been given by Baskin and Zewail[21] for a (||, ||) transition case. As discussed in the Introduction, extension of the formulation to the (||, ⊥) case yields[37]

$$r(t) = -\frac{1}{20}\left(1 + 3\frac{\sum_j P_j \cos 2\omega_n t}{\sum_j P_j}\right) \tag{3.6}$$

where $r(t)$ is the anisotropic contribution to the signal at pump-probe time delay t and P_j denotes the relative rotational population distribution, which is assumed to be a Gaussian function given by

$$P_j = \frac{1}{\Delta j\sqrt{\pi}}\exp\left[-\frac{(j - j_{\max})^2}{(\Delta j)^2}\right]. \tag{3.7}$$

The j dependent nutational frequency $\omega_j = 4\pi B_j$, where B is the rotational constant of the nascent molecular product in rotational quantum level j. However, analysis of the $r(t)$ shown in Figure 3.12 (a) using this formulation failed to reproduce the experimental data. This is due to the multiphoton nature of the pump transition. A three–photon pump transition would be expected to produce a greater degree of alignment than is expected for a one–photon transition because it produces a $\cos^6\theta$ distribution in the nascent products rather than a $\cos^2\theta$ distribution. This narrower initial alignment causes the dephasing of rotational anisotropy to appear faster than it really is.

In order to model time–dependent rotational anisotropy experiments in which the excitation is a multiphoton process, the existing treatment[21] has been extended to apply to the current experiment, which was assumed to involve three-photon pump and single photon probe transitions. If all the pump transition dipoles are aligned parallel to each other, Equation (1.19) becomes:

$$I_S(t) = A(t)\left\langle |\hat{\mu}_1(0)\cdot\hat{\varepsilon}_1|^6 |\hat{\mu}_2(t)\cdot\hat{\varepsilon}_2|^2 \right\rangle \tag{3.8}$$

where $A(t)$ contains the isotropic contribution to the signal. For this case, if the probe dipole is perpendicular to the pump dipole at time zero we find that the rotational anisotropy can be expressed as:[154]

$$r(t) = -\frac{1}{12}\left[1+3\frac{\sum_j P_j \cos 2\omega_n t}{\sum_j P_j}\right], \tag{3.9}$$

where the symbols are defined above.

To obtain the experimental r(t) and $I_{isotropic}$ curves shown in Figure 3.12, the average fluorescence intensity at negative time delays (probe pulse absorbed before pump) was subtracted from each transient before performing proper normalisation to the asymptotic limits at long time delays. A least–squares fit of the observed $r(t)$ data using the above formulae is also presented in Figure 3.12 (a). The fit corresponds a center j_{max} of the rotational distribution of the I_2 fragment = 354 ± 38 and a 1/e width of the distribution Δj = 509 ± 52.

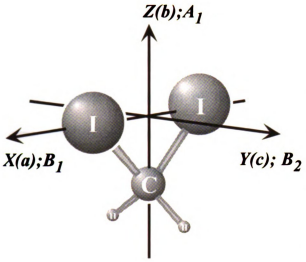

Figure 3.13 Model of the CH_2I_2 molecule in the centre of mass frame, showing the principal (*X*, *Y* and *Z*) and rotational (*a*, *b* and *c*) axes and their transformation under C_{2v} symmetry.

Figure 3.13 shows a model of CH_2I_2 in the centre-of-mass frame. Note that because of the large mass of the iodine atoms compared to carbon and hydrogen, the centre of mass of the molecule is very close to the midpoint between the iodine atoms. Because of this, upon dissociation into I_2 and CH_2, rotational motion of CH_2I_2 about the *X* axis will be manifested as translational motion of the CH_2 fragment. Similarly, rotational motion about the *Y* (*c*) axis will be partitioned into I_2 rotation and CH_2 translation. On the other hand, most of the rotational energy of the parent about the *Z* (*b*) axis, the symmetry axis of CH_2I_2, remains as rotational energy of the I_2 fragment because the moment of inertia of I_2 is significantly larger than that of CH_2. Thus the rotational motion of the parent molecule becomes translational motion of the CH_2 fragment and rotational motion of the I_2 fragment after dissociation. The CH_2 fragment is therefore expected to have relatively high translational and vibrational excitation but low rotational excitation. A room temperature sample of CH_2I_2 would be expected to have a rotational population centred at $j \approx 100$, so the results above indicate a difference of about 250 $\hbar$ in angular momentum between the parent CH_2I_2 and the I_2 fragment. Conservation of angular momentum demands that

$$\mathbf{J}_{CH_2I_2} = \mathbf{J}_{CH_2} + \mathbf{J}_{I_2} + \mathbf{L}, \tag{3.9}$$

where $\mathbf{J}_x$ is the angular momentum of the appropriate species and **L** indicates that portion of the angular momentum of the parent that is converted on dissociation to linear momentum in the fragments. Due to the large masses of the iodine atoms, the magnitude L of the 'orbital' angular momentum can be well approximated as that of the CH_2 fragment only,

$$L \approx m_{CH_2} \mathrm{v}_{CH_2} b \tag{3.10}$$

where m_{CH_2} and v_{CH_2} denote respectively the mass and velocity of the CH_2 fragment and the "impact parameter" b represents the perpendicular distance between the velocity vector $\mathbf{v}_{CH_2}$ and the center of mass of CH_2I_2. Since $\mathbf{J}_{CH_2}$ is negligible, we find from (3.9) that $L \approx 250\hbar$. This, along with the broad spread of rotational population Δj, indicates a high degree of rotational excitation in the nascent I_2 after dissociation.

The isotropic transient shown in Figure 3.12 (b) clearly exhibits oscillations at positive time delays. As with the data collected at 340 nm, this indicates that the reaction mechanism responsible for formation of molecular iodine in this channel is concerted, *i.e.* happens in a single kinetic step. To obtain quantitative information about the vibrational coherence, the isotropic data were modelled using the same exponentially decaying cosine function (3.1) used for the D' → A' fluorescence (*vide supra*). Least–squares fit of the experimental isotropic data in Figure 3.12 (b) using the functional form of (3.1) gives

rise to the following parameters: $\tau = 501 \pm 82$ fs, $\omega = 98 \pm 2$ cm^{-1} and $\phi = 51 \pm 6°$. The fitted result is shown in Figure 3.12 (b).

Most ion–pair states of I_2 have vibrational frequencies on the order of 100 cm^{-1}; the fitted value of 98 cm^{-1} therefore seems reasonable if the species being probed is the I_2 fragment. Also, the fitted vibrational frequency should provide a lower bound to the nominal vibrational frequency of the fluorescent state, particularly so because anharmonicity tends to reduce the effective vibrational frequency of higher–lying vibrational levels. This allows us to eliminate as the source of the 272 nm fluorescence those I_2 states that have vibrational frequencies smaller than 98 cm^{-1}.

There are several known emission systems of I_2 that fall into the 250–290 nm spectral region, notably the $F0_u^+ \rightarrow X0_g^+$, $f0_g^+ \rightarrow A1_u$, $f0_g^+ \rightarrow B''1_u$, $f'0_g^+ \rightarrow B0_u^+$, $G1_g \rightarrow A1_u$ and $g0_g^- \rightarrow 2431\ ^3\Pi_{0u}^-$ [150,151,155,156] transitions. Since the vibrational frequencies of both the $F0_u^+$ (96.31 cm^{-1}) and the $f'0_g^+$ (96.98 cm^{-1}) states are smaller than the fitted vibrational frequency of 98 cm^{-1}, they are quite unlikely to be responsible for the observed vibrational coherence based upon the above criterion, although similar features observed by Okabe *et al.*[124] and Fotakis *et al.*[125] have been tentatively assigned to the $F0_u^+ \rightarrow X0_g^+$ fluorescence of the nascent I_2 fragment. However, there is a sizeable uncertainty (2 cm^{-1}) in the present determination of the vibrational frequency, which does not permit the involvement of the $F0_u^+$ and $f'0_g^+$ states to be unequivocally eliminated.

The remaining three upper states have quite similar vibrational frequencies, *i.e.* 104.14 cm^{-1} for $f0_g^+$, 106.60 cm^{-1} for $G1_g$ and 105.70 cm^{-1} for $g0_g^-$. Taking into consideration the anharmonicity constants of 0.2113 cm^{-1}, 0.2134 cm^{-1} and 0.4900 cm^{-1} for the f, G and g states respectively, we can estimate that a vibrational frequency of 98 cm^{-1} corresponds to vibrational levels 14, 19 and 7 respectively in these states.

If the f $\left(^3\Pi_{0g}^+\right)$ state is responsible for the vibrational coherence at 272 nm, the f $\rightarrow$ B fluorescence would be expected to contribute to the coherences observed in the 340 nm region. This will have two effects; the dispersed fluorescence spectrum in this region will be comprised of contributions from both transitions, and the observed dephasing would be due in part to the additional contribution to the time-resolved signal.

First, a least-squares fit to the fluorescence in the 290 - 350 nm region of the spectrum was attempted, taking into account the possible contribution to signal in this region of fluorescence from the f $\rightarrow$ B transition. Figure 3.14 shows the results, along with the fit obtained without accounting for the f $\rightarrow$ B fluorescence, for comparison. The fit shown in Figure 3.14 (a) was determined by assuming that all the fluorescence in this region was produced by the I_2 (D' $\rightarrow$ A') transition. Figure 3.14 (b) shows the I_2 f$\rightarrow$ B fluorescence in the same region, produced by excitation of neat I_2 vapour at 612 nm. In Figure 3.14 (c), the same data as in (a) are fit again, this time incorporating $\approx$ 30 % (optimized for fit) of f $\rightarrow$ B fluorescence. The fits were both obtained by using a least-squares routine and by assuming a Gaussian distribution of vibrational levels in the D'

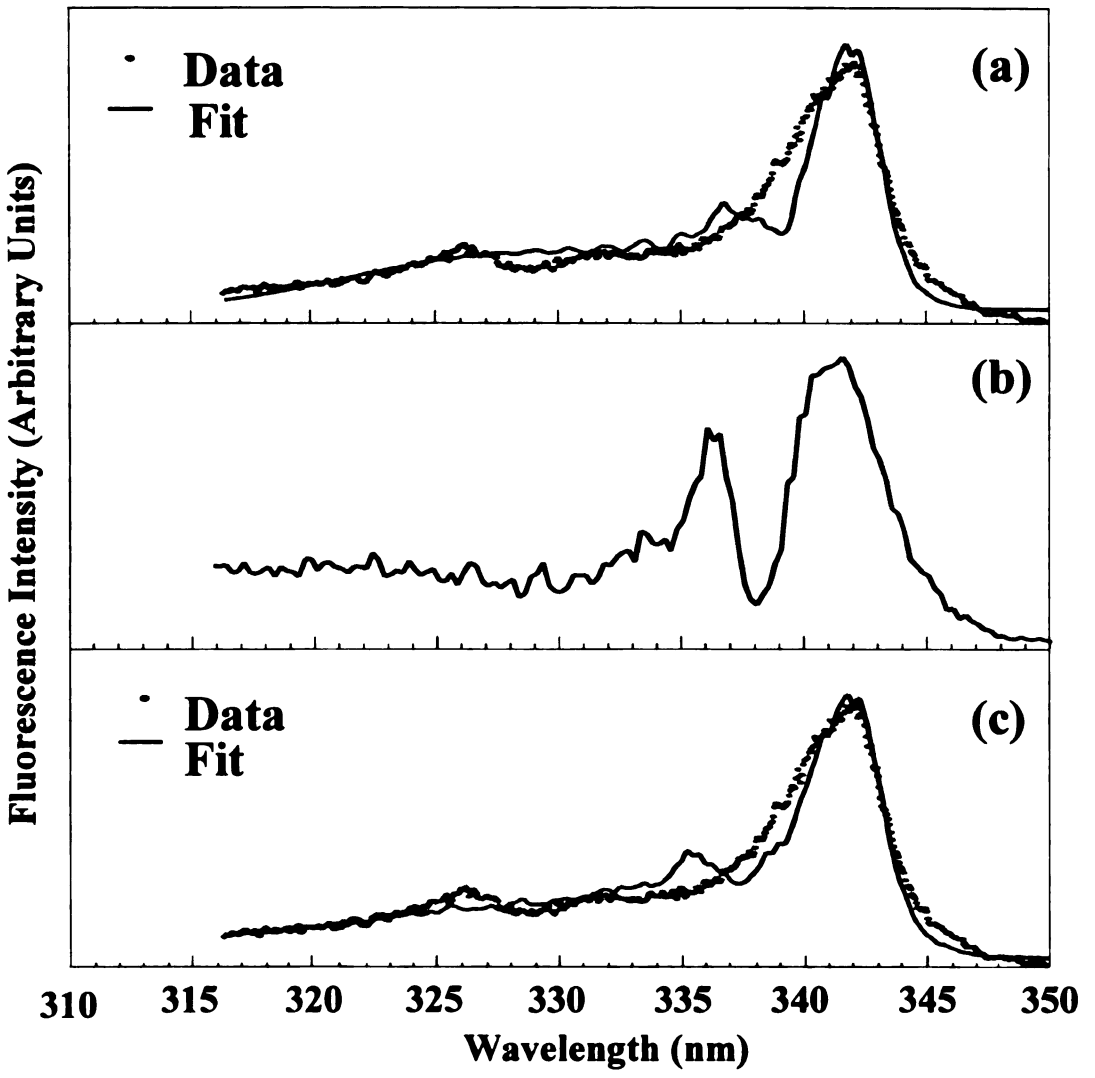

Figure 3.14 Fit to the dispersed I_2 D'→ A' fluorescence spectrum produced from the dissociation of CH_2I_2.

(a) Fit obtained using only D'→ A' fluorescence.

(b) The f → B fluorescence spectrum obtained from excitation of neat I_2 vapour.

(c) Fit to the observed fluorescence in the 300-350 nm range, taking into account the possibility of contribution from the f → B transition. The spectrum shown in (b) was scaled by a factor determined by optimisation and incorporated into the fit.

state; the observed fits correspond to a central vibrational level v_{max} = 8 in Figure 3.14 (a) and 7 in Figure 3.14 (c).

To assess the possibility of a contribution from the f → B transition to the time-resolved data collected at 340 nm, the vibrational dynamics shown in Figure 3.5 were fit using a bimodal-type model. Figure 3.15 shows the results of this fit, along with the original damped cosine fit for comparison. The displayed fit was obtained by assuming a bimodal Gaussian distribution of vibrational levels. One mode is centred at v' = 18 in the D' state with a FWHM of 7. This corresponds to a vibrational spacing of 96.5 cm^{-1}, which

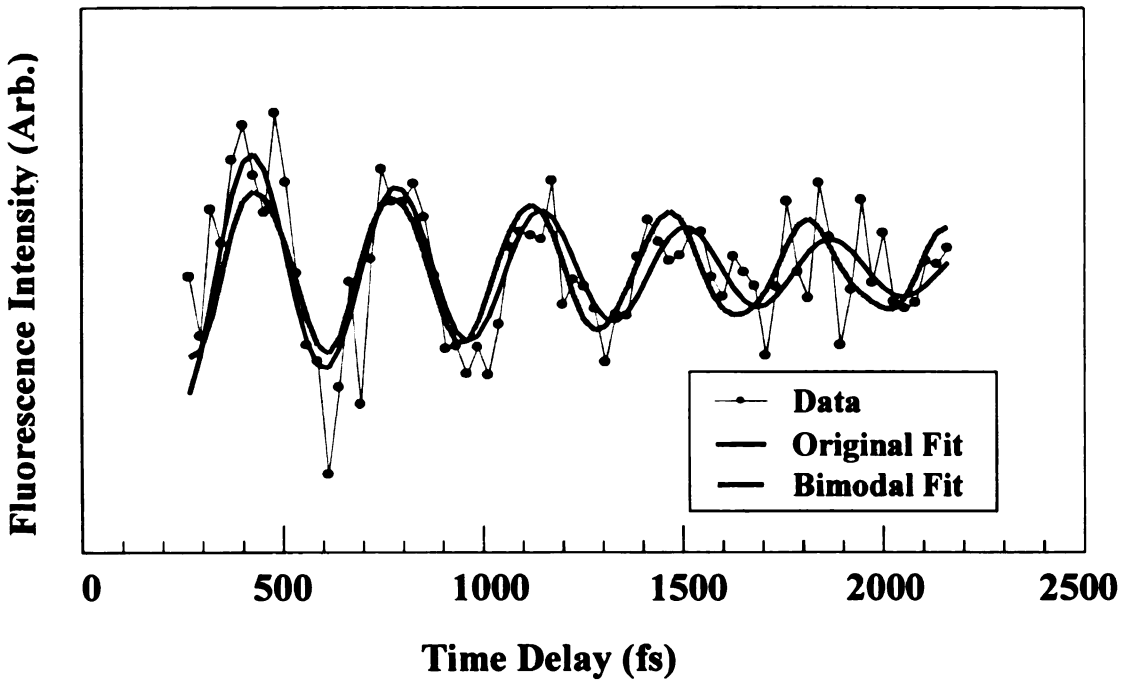

Figure 3.15 Fits to the vibrational coherences in the I_2 D'→ A' fluorescence at positive pump-probe delay times.

(a) Original, exponentially damped sinusoidal fit shown above (Figure 3.5).

(b) Bimodal Gaussian fit. One mode has an oscillation frequency of 96.5 cm^{-1} and a FWHM of 7. The second mode has an oscillation frequency of 104 cm^{-1} and a FWHM equivalent to a single D' vibrational level.

reflects an oscillation period of 346 fs and is close to the result from the damped sinusoidal model discussed above (*vide supra*). The second mode has an oscillation frequency of 104 cm^{-1} and a FWHM equivalent to a single D' vibrational level. This mode appears to be contributing approximately 15 % of the time-dependent signal at 340 nm, which is consistent with the intensity of the f $\rightarrow$ B fluorescence expected in this region.

Clearly, there is a discrepancy between the apparent vibrational population of the D' state obtained from fitting the dynamic data (v' = 18) and dispersed fluorescence spectrum (v' = 8), even when the possibility of another contributing process is accounted for. The reason for this is not clear.

3.3.2 Other Compounds

In addition to methylene iodide, photoinduced molecular detachment experiments were performed on other gem-dihaloalkanes. Figure 3.16 shows dispersed fluorescence spectra produced by multiphoton dissociation of CH_2Br_2 and CH_2Cl_2 at 312 nm. Both spectra were obtained from static cells. In both cases, fluorescence characteristic of the X_2 D' $\rightarrow$ A' transition was observed.[145,147,157] These results indicate that the reaction is general, *i.e.* the observation of molecular halogens in the D' state as a product of photoinduced molecular detachment from dihaloalkanes is not restricted to methylene iodide. Because of the elevated vapour pressures of CH_2Br_2 and CH_2Cl_2 at room temperature, it was necessary to reduce the pressure in the cells. This was done by

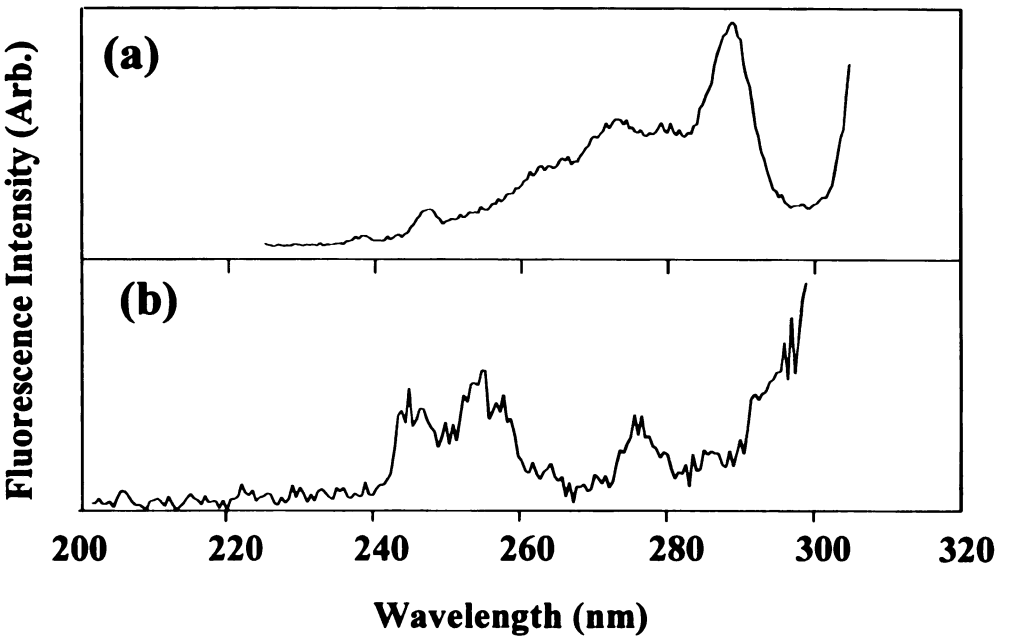

Figure 3.16 Dispersed fluorescence spectra of $X_2(D')$ produced by multiphoton excitation at 312 nm.

(a) From CH_2Br_2 at 0 °C.

(b) From CH_2Cl_2 at 0 °C. The increasing signal level at longer wavelengths is due to laser scatter.

maintaining the liquid reservoir of each cell in a cold bath; the CH_2Br_2 cell was kept at 0 °C in an ice bath and the CH_2Cl_2 cell at –41 °C in a mixture of dry ice and acetonitrile.

As with methylene iodide, time-resolved data of this reaction were obtained from each cell by multiphoton excitation by a 312 nm femtosecond pulse, followed by probing with a second pulse at 624 nm. Figure 3.17 shows the resulting transients for CH_2Br_2 and CH_2Cl_2. Each set of data was obtained at 0 °C. Signal was collected at the position of maximum intensity for the D' → A' fluorescence, corresponding to 287 nm for the CH_2Br_2 cell and 254 nm for the CH_2Cl_2 cell. A number of similarities can be seen with

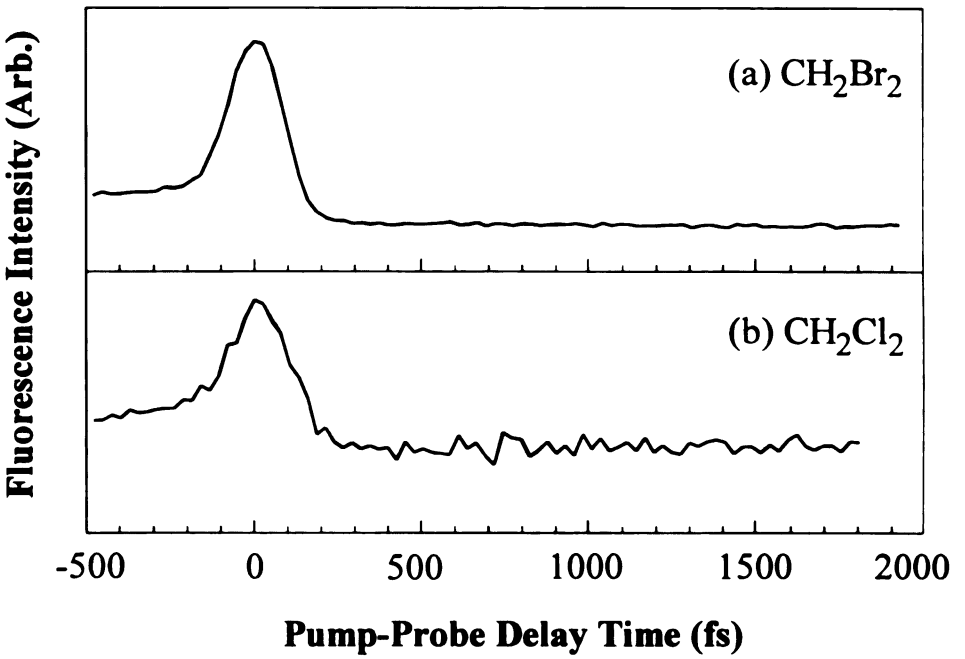

Figure 3.17 Transient data of photoinduced molecular detachment of $X_2(D')$ from dihaloalkanes. Both sets of data were recorded from static cells, with the polarisation vectors of pump and probe pulses parallel to each other.

(a) From CH_2Br_2 at 287 nm.

(b) From CH_2Cl_2 at 254 nm. The increased signal:noise ratio in this data, as in the spectrum in Figure 3.16 (b), is due to low signal levels.

the time-resolved data of the reaction to produce I_2 in the D' state (Figure 3.4), most notably that the fluorescence intensity in each case shows a substantial enhancement at time zero and depletion at positive times. As with the spectral data displayed in Figure 3.16, the signal level from the CH_2Cl_2 cell is comparatively low, resulting in a greater signal to noise ratio than was observed from the other systems.

Pump-probe data were obtained from the CH_2Br_2 cell at 287 nm with parallel and perpendicular polarisation vectors. The results are shown in Figure 3.18. Using the same methods already discussed, the isotropic and anisotropic portions of the signal at positive

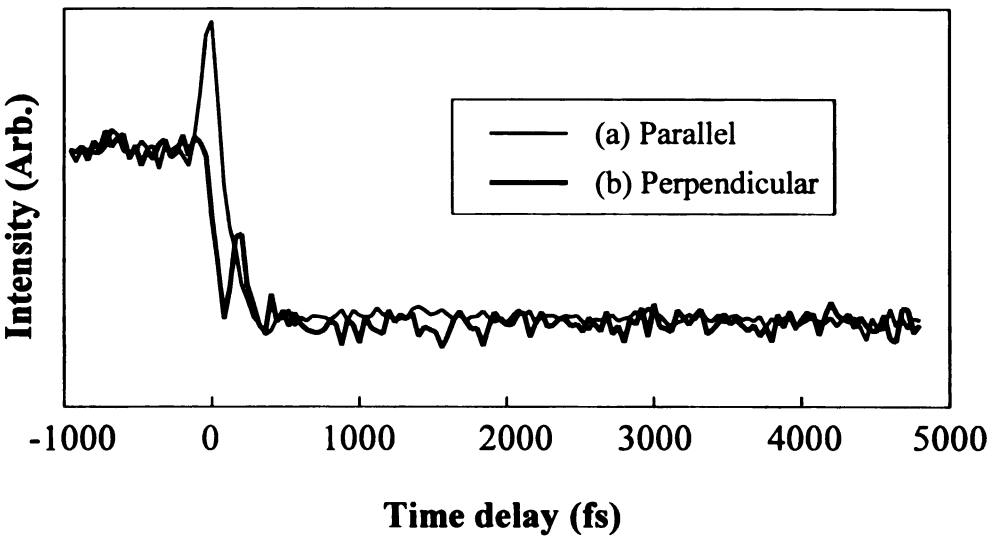

Figure 3.18 Time resolved data from the multiphoton dissociation of CH_2Br_2 using 312 nm femtosecond pulses. The transients were obtained at 287 nm, with the polarisation vector of the probe laser aligned parallel (a) and perpendicular (b) to the pump.

pump-probe delay times were extracted and are shown in Figure 3.19 (a) and (b). The rotational dephasing of the molecules was determined by fitting the anisotropic portion of the signal using Equation (3.8). The fit was obtained using a Gaussian distribution of rotational level population, centered at $j_{max} = 76 \pm 7$, with a FWHM Δ_j of 170 ± 20. A Br_2 molecule with $j = 76$ populated has 250 cm^{-1} of rotational energy. This indicates considerably less rotational excitation than was observed in the I_2 fragment at 272 nm (direct comparison with the I_2 D' rotational excitation isn't possible because the *r(t)* data at 340 nm could not be reliably analysed).

Similarly, molecular parameters of Br_2(D') were used to obtain a fit to the isotropic portion of the signal. Unlike the data collected from the CH_2I_2 cell, vibrational modulation at positive times can not be clearly seen in this data. There does however appear to be a single vibrational oscillation in the perpendicular data, which is probably

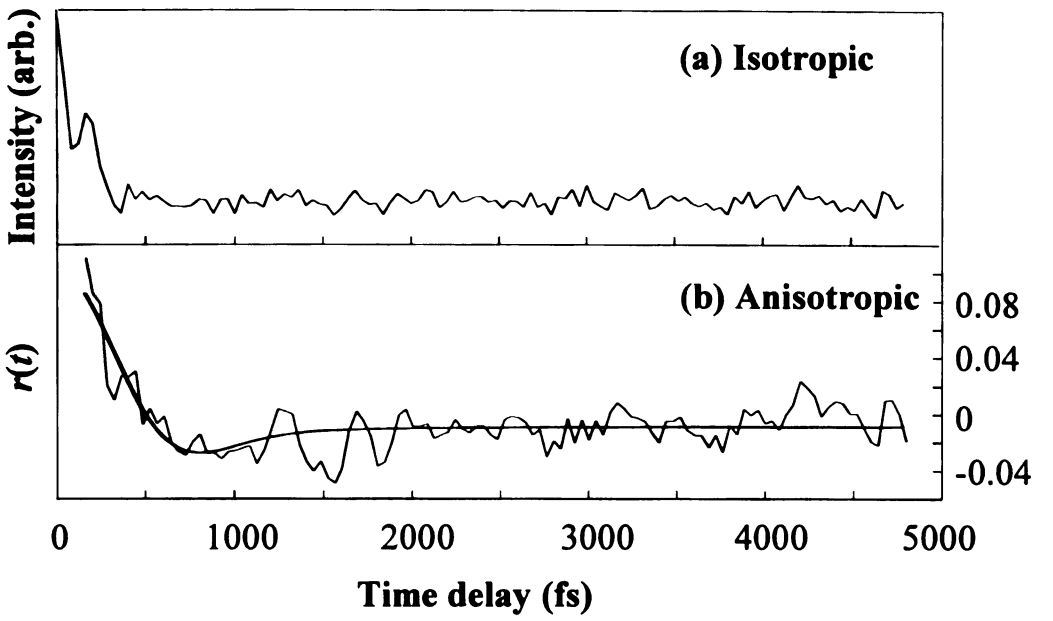

Figure 3.19 Anisotropic (a) and isotropic (b) portions of the 287 nm data from the CH_2Br_2 cell. The fit to the *r(t)* derived from the data is also shown. To obtain the *r(t)*, the data was properly normalised and a three-point smoothing applied.

hidden underneath time zero when pump and probe are polarised parallel to each other. Fourier transform analysis of the isotropic portion of the data yields contributing frequencies at 33, 104 and 222 cm^{-1}, corresponding to oscillation periods of 1000, 320 and 150 fs respectively. The fundamental frequency of Br_2 in the D' state is 150.86 cm^{-1}, so there is no apparent correspondence between this frequency and the results of the Fourier transform analysis. Analysis of several scans collected with the pump and probe lasers polarised parallel was also not able to yield consistent results, either by Fourier transform or by modelling the vibrations as described previously for the CH_2I_2 data.

Multiphoton excitation of CBr_2F_2 and CBr_2Cl_2 at 312 nm is also found to produce Br_2 in the D' state, see Figure 3.20 (b) and (c). Observation of spectra from CBr_2F_2 and CH_2Br_2 recorded at 0 °C seems to indicate a difference in vibrational population.[154]

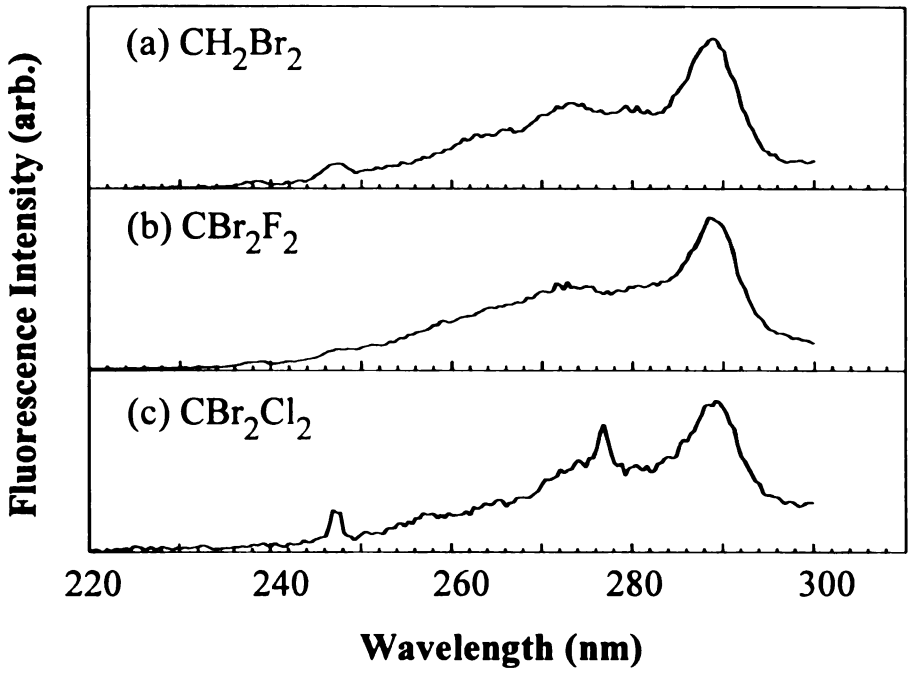

Figure 3.20 Dispersed fluorescence spectra from multiphoton excitation at 312 nm of CH_2Br_2 (a), CBr_2F_2 (b) and CBr_2Cl_2 (c). All three are produced by the Br_2 $D' \rightarrow A'$ transition.

However, the vapour pressure of CBr_2F_2 is 314 Torr at 0 °C,[158] which produces a gas phase collision frequency of 2.45 x 10^9 s^{-1}. This is sufficient to cause vibrational relaxation in the observed fluorescence spectrum. The spectra shown in Figure 3.20 (a) and (b) were recorded at 0 and -61 °C respectively; the two molecules have comparable vapour pressure at these temperatures (11.5 Torr for CH_2Br_2[158] and ≈ 12 Torr for CBr_2F_2.[ii] Examination of Figure 3.20 indicates that in fact the vibrational temperature in the D' state of Br_2 is similar whether the parent molecule was CH_2Br_2 or CBr_2F_2.

A comparison of the dissociation times of CBr_2F_2, CH_2Br_2 and CBr_2Cl_2 was also

[ii] Calculated using data from Reference 158 and a modified Clausius-Clapeyron of the

made, see Figure 3.21. The scans were collected consecutively, with the laser intensity kept constant as far as possible to avoid apparent differences in dissociation time caused by saturation of the transitions. Analysis of the time zero data using Equation (A3) and assuming the same pulsewidth for all three scans yielded dissociation times of 58.6 ± 1.4 fs for CH_2Br_2, 80.6 ± 4 fs for CBr_2Cl_2 and 29.7 ± 0.6 fs for CBr_2F_2, as shown in Figure (3.21).

The dissociation time of CBr_2F_2 is significantly faster than either of the other two molecules. The relative masses of CH_2Br_2 and CBr_2F_2 might lead one to expect that the latter molecule would dissociate more slowly, so this result is slightly surprising. The enthalpies of reactions (ii) and (iv) (see Table II) are quite similar, so the difference in dissociation time also apparently can't be explained by the thermodynamics of the systems involved. Since the ground states of CCl_2 and CF_2 are singlets,[160,161] the energies required to produce these fragments in the first excited (triplet) states were calculated and are also displayed in Table II. In this case however, the enthalpy of reaction (v) is substantially higher than the enthalpy of reaction (iii), which makes the result shown in Figure 3.21 even more difficult to explain. The most probable cause of the anomalous dissociation time is therefore almost certainly the high electron density of the fluorine atoms, which is expected to significantly affect the electronic states of the parent molecule. For this reason, the CBr_2F_2 data will not be compared with results from its analogues.

---

form $\log_{10}(p)=\frac{-0.2185A}{T}+B$ [159].

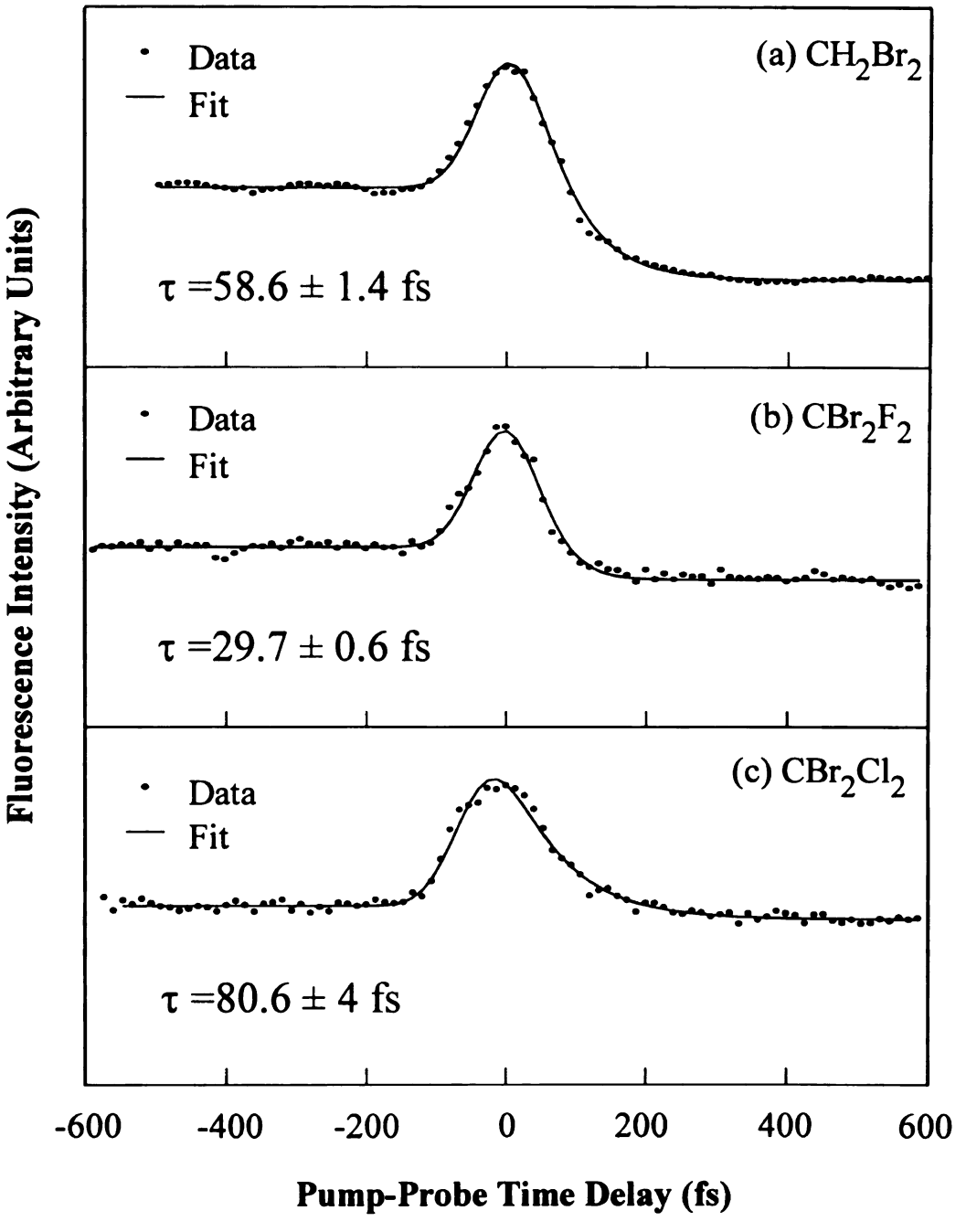

Figure 3.21 Time zero data for the molecular detachment of halogens from CX_2Br_2. Fits to the data are shown as continuous lines. The time data was obtained consecutively, with the same laser intensity for each scan.

(a) CH_2Br_2 at 0 °C.

(b) CBr_2F_2 at -47 °C.

(c) CBr_2Cl_2 at 0 °C.

Assuming that Equation 3.2 applies, the ratio of the dissociation times of CBr_2Cl_2 and CH_2Br_2 is expected to be ≈ 2, not 1.4 as measured experimentally. The reason for the difference could possibly be explained by the fact that the enthalpy required to form CCl_2 and $Br_2(D')$ from CBr_2Cl_2 is lower than is needed to produce CH_2 and $Br_2(D')$ from the dissociation of CH_2Br_2, as shown in Table II. This could have the effect of making less energy available for partitioning into fragment recoil in the latter reaction. This is somewhat speculative, however; the electronics of both reactants and products are also expected to play a role. Additionally, the assumption that the dissociation can be treated as a pseudodiatomic separation with no redistribution of energy during the reaction is rather naïve in the case of CBr_2Cl_2, where the mass of the two fragments is comparable and the C-Br and C-Cl vibrational frequencies similar.

Table II. Thermodynamics of the dissociation reaction $CX_2YZ \rightarrow CX_2(\tilde{X}) + YZ(D')$, where X = H or a halogen and Y and Z are halogens.[iii]

Reaction	**Enthalpy (cm^{-1})**	**eV**
(i) $CH_2Br_2 \rightarrow CH_2(\tilde{X}) + Br_2(D')$	85047	10.5
(ii) $CBr_2Cl_2 \rightarrow CCl_2(\tilde{X}) + Br_2(D')$	70735	8.8
(iii) $CBr_2Cl_2 \rightarrow CCl_2(\tilde{A}) + Br_2(D')$	79042	9.8
(iv) $CBr_2F_2 \rightarrow CF_2(\tilde{X}) + Br_2(D')$	68557	8.5
(v) $CBr_2F_2 \rightarrow CF_2(\tilde{A}) + Br_2(D')$	88398	11.0

[iii] Enthalpies of formation of reactants were taken from References 162 and 163 and of the products from Reference 162. The value of T_e for the D' state of Br_2 was taken from Reference 148; singlet-triplet splittings for the carbene fragments from References 160 and 161.

All the molecules discussed thus far have one thing in common; their C_{2v} symmetry. In the interest of observing the effects of breaking this symmetry, experiments were also conducted on gas-phase CH_2ICl.

Time-dependent data were observed from this cell at two wavelengths; 340 nm and 430 nm. The fluorescence spectra in these two regions are shown in Figure 3.22. The 430 nm fluorescence is probably due to the D' $\rightarrow$ A' transition, which is known to occur at this wavelength.[164,165] Fluorescence between 325 and 340 nm has been assigned to the $G(^3P_1) \rightarrow A(^3\Pi_1)$ transition of ICl;[166] it is possible that the observed fluorescence at 340 nm originates from this transition. However, it is known that ICl decomposes readily to produce I_2;[167] for this reason, the spectra from the CH_2ICl sample were compared with the dispersed fluorescence spectrum obtained from neat I_2 vapour. This is also shown in Figure 3.22. Comparison of the spectra from each source indicates that the fluorescence observed at 340 nm from the CH_2ICl sample may well include a contribution from the f $\rightarrow$ B transition of I_2, but that the 430 nm signal probably contains no contribution from I_2 fluorescence.

Figure 3.23 shows pump-probe data collected at each of these wavelengths from the CH_2ICl cell at 0 °C. Both sets of data exhibit intense time zero enhancement in the signal and depletion at positive pump-probe delay times. Although it is possible that the fluorescence detected at 340 nm is contaminated by a contribution from ambient I_2 (*vide supra*), this is not expected to significantly affect the measured dissociation time. The

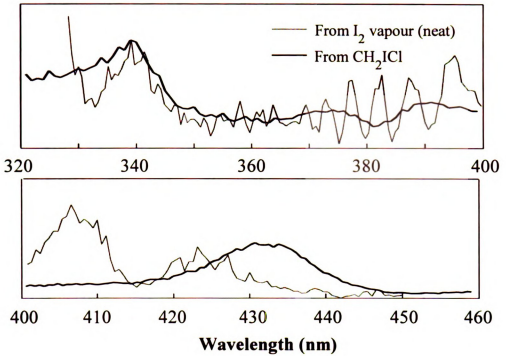

Figure 3.22 Dispersed fluorescence spectra from the multiphoton dissociation of CH_2ICl at 0 °C, showing both the 320 - 400 and the 400 - 460 nm regions. The fluorescence spectra produced in these regions from a sample of pure I_2 vapour are also shown for comparison.

reason for this supposition is that the time-resolved behaviour of I_2 f $\rightarrow$ B fluorescence under excitation with 612 and 324 nm pulses is quite different to what is observed in Figure 3.23 (see Figure 3.3). For this system, there is no intense feature at time zero such as the one shown in Figure 3.23 (a). Additionally, for I_2(f $\rightarrow$ B) the 624 nm pulse is the pump and the 312 nm pulse the probe; time-resolved data would then be observed in the region marked as negative time in Figure 3.23. The following analysis is therefore made assuming that the observed pump-probe transient is due only to the G $\rightarrow$ A transition of ICl.

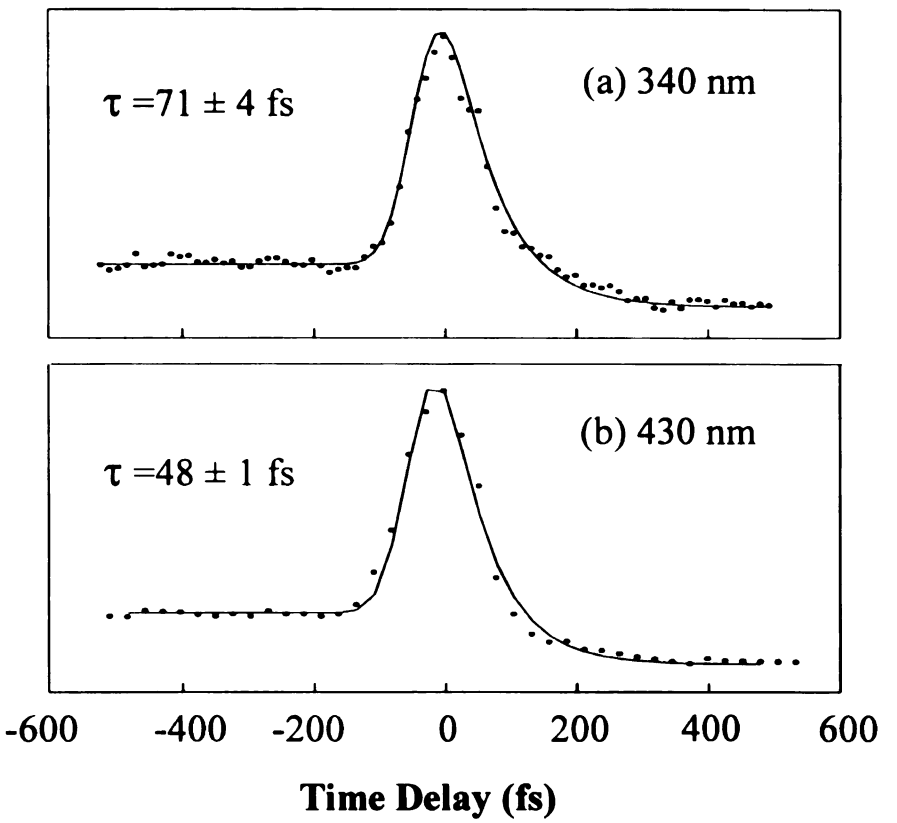

Figure 3.23 Pump-probe data from the multiphoton dissociation of CH_2ICl at 312 nm.

(a) Collected at 340 nm, corresponding to the G → A transition.

(b) Collected at 430 nm, corresponding to the D' → A' transition.

The displayed fits are produced by modelling the dissociation time using the same method described above for CH_2I_2. The observed fits yielded $1/e$ times of 71 ± 4 fs for dissociation to the G state and 48 ± 1 fs for dissociation to the D' state. Assuming the excitation process and energy partitioning in CH_2ICl to be the same as in CH_2I_2, the latter value is in agreement with the dissociation time that would be predicted by reduced mass considerations. Using Equation (3.3), again with a length parameter of 2 Å, to calculate the kinetic energy of the fragments from the dissociation time yields a translational energy of 4278 cm^{-1} (0.53 eV) when the product is ICl(G) and 9361 cm^{-1} (1.16 eV) when

the product is ICl(D'). This represents a difference in translational energy of 5083 cm^{-1}, or 0.63 eV. The energy separation between the G and D' states of CH_2ICl is 6491 cm^{-1}, or 0.8 eV.[148] It therefore appears that ≈ 0.6 eV of the excess energy available when the halogen product is ICl(D') is partitioned into kinetic energy and the remaining 0.2 eV into internal energy of the fragments.

The dynamics of molecular photodetachment of ICl(G) from CH_2ICl were studied with the probe laser polarised both parallel and perpendicular to the pump. A certain degree of rotational anisotropy was observed. The *r(t)* obtained from the data, along with a least-squares fit, is presented in Figure 3.24 (a). As before, the fit was determined by assuming a Gaussian population of rotational *j* levels and fitting for the position and FWHM of the Gaussian. Because the observed rotational population so closely resembles a Boltzmann distribution, see Figure 3.24 (b), the *r(t)* was also fit to a thermal distribution of rotational levels. The fit is shown in Figure 3.24 (a) and the resulting rotational population in Figure 3.24 (b). In both cases, the rotational population of ICl molecules was found to be centered at approximately $j = 10$, which corresponds to a rotational temperature in the Boltzmann case of 169 K and a rotational energy of 6 cm^{-1}. This is very much lower than was observed in the X_2 fragments, and indicates that CH_2ICl is undergoing a different photodissociation mechanism than was observed in the CH_2X_2 molecules. This result, and the apparently lower excitation energy (*vide supra*), are not unexpected because the CH_2ICl molecule carries none of the transition restrictions arising from the C_{2v} symmetry of the other molecules studied.

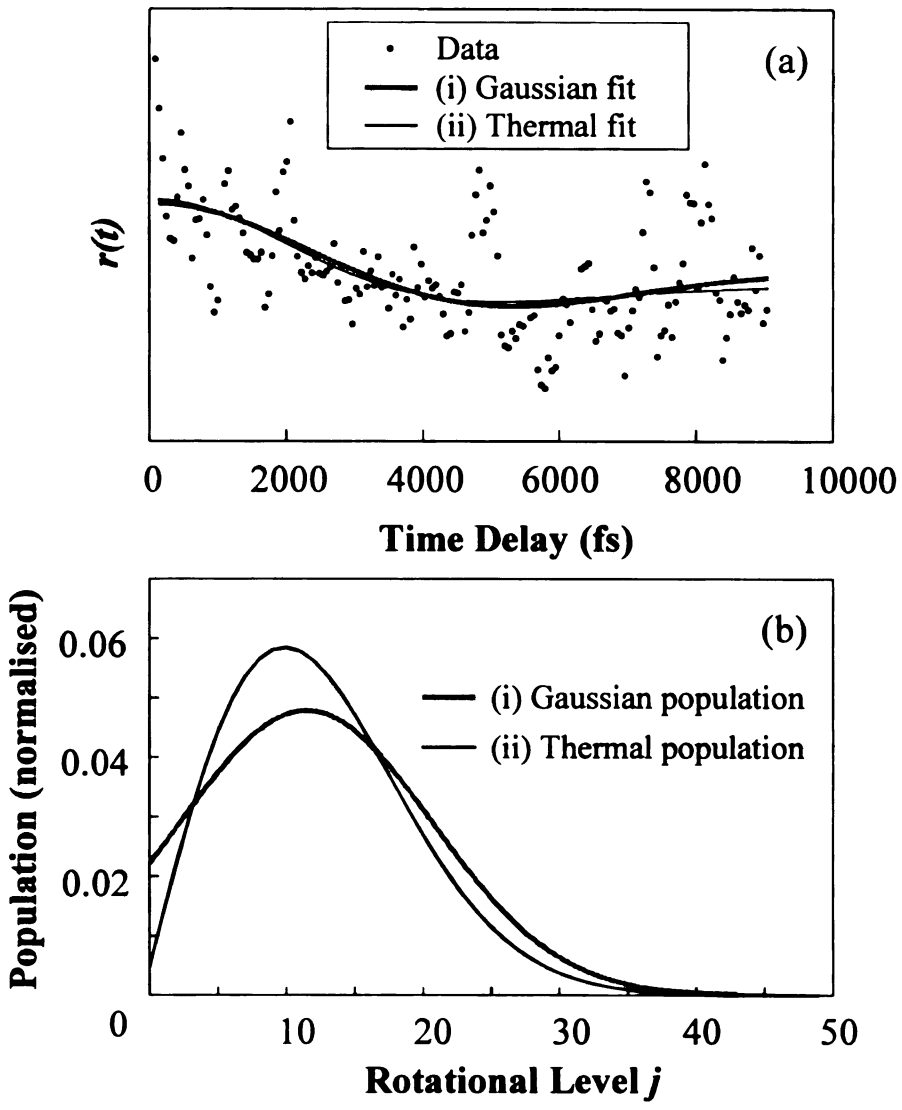

Figure 3.24. Pump-probe data was collected from the CH_2ICl sample at 340 nm with the liquid reservoir maintained at 0 °C. Dynamics were studied with the probe laser polarised both parallel and perpendicular to the pump.

(a) The purely anisotropic contribution *r(t)* to the 340 nm signal. Also shown are a least-squares fit obtained by assuming a Gaussian distribution of rotational levels (i) and a thermal (Boltzmann) distribution (ii).

(b) The rotational populations *P(j)* responsible for the fits shown in (a). The two results are very similar, and produce almost identical fits.

There were no discernible vibrational oscillations in the time-resolved fluorescence data collected at 340 nm from the CH_2ICl cell. The 430 nm data, however, does exhibit some modulation in the intensity as a function of pump-probe time delay; this data is shown in Figure 3.25. Pump-probe data were collected with the pump and probe lasers polarised parallel to each other and the liquid reservoir maintained at 0 °C. Fits were obtained using the exponential decay model described above and also by fast Fourier transform (FFT); the fits are also shown in Figure 3.25, along with the resulting parameters. The FFT 'fit' was obtained by taking a Fourier transform of the transient data. Two major contributing frequencies were identified from the FFT results and the

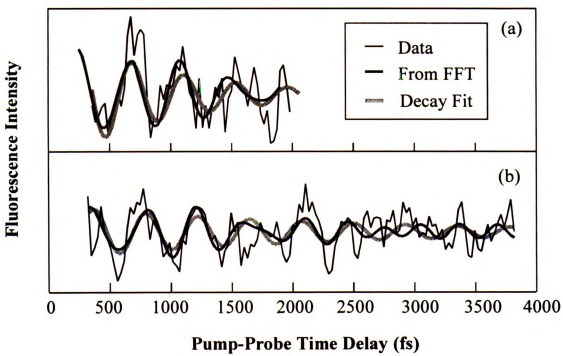

Figure 3.25 Pump-probe data collected from the CH_2ICl sample. Fits to the data obtained from the Fourier transform and from the exponential decay model (Equation 3.1) are also displayed.

time behaviour arising as a result of these frequencies simulated. To do this, a crude model was constructed in which the time-dependent behaviour is produced by addition of cosines of the contributing frequencies. The data were fit using a bimodal Gaussian distribution, with the centre of each mode fixed at the frequency yielded by the FFT results and the width and relative intensity of each mode allowed to vary. It can be seen from Figure 3.25 that a fairly good fit to the data can be obtained by this method. The central frequencies used to obtain this fit were 78 cm^{-1} for the decay fit and 78 and 107.4 cm^{-1} for the Fourier fit, which were the frequencies yielded by the FFT. Two sets of data are shown in Figure 3.25; (a) and (b) were recorded separately but were both fit using the same frequency parameters. The observed frequencies therefore seem to be quite reproducible. A beat frequency of 78 cm^{-1} corresponds to $v \approx 23$ in the A state of ICl,[168,169] $v \approx 86$ of ICl(D'),[148] or $v \approx 78$ of ICl(G).[166] Similarly, an oscillation of 107.4 cm^{-1} indicates occupation of v = 17-18 in ICl(A),[168,169] v = 60 in ICl(D')[148] or v = 56 - 57 in ICl(G).[166]

3.4 Discussion

3.4.1 Spectroscopy

A. The Parent Molecule

For all the molecules studied, photoinduced molecular detachment was found to occur very rapidly (usually < 100 fs). Within this time, the molecules are not expected to have rotated to any significant degree, which makes it likely that all the dipoles of the

multiphoton pump transition are parallel, since this is the most favourable situation for absorption. This is particularly so in the case of the pathway responsible for the I_2 product that fluoresces at 272 nm. Figures 3.11 and 3.12 clearly show that there is a high degree of anisotropy in this pathway. If each of the transition dipoles corresponding to the three–photon pump transition had different orientations, one would not expect the anisotropy to be so clear. Thus, the three transition dipoles are likely to be parallel to each other; in the absence of evidence to the contrary it is reasonable to assume that they are so.

Few studies of the spectroscopy of CH_2I_2 at high energies have been conducted, and the large size of the iodine atoms makes the molecule difficult to model using theoretical methods. As a consequence, the excited state which is being accessed by the excitation is unknown. In an effort to elucidate the nature of the parent electronic state that correlates to dihalogen products, Okabe *et al.* compared the absorption spectrum of CH_2I_2 in the vacuum ultraviolet region with the fluorescence excitation spectrum in the same region (342 nm detection).[124] The absorption and fluorescence excitation spectra both showed broad continua, which were ascribed to C – I $\sigma \rightarrow \sigma^*$ transitions. Although features assignable to Rydberg transitions appeared in the absorption spectrum, their absence from the fluorescence excitation spectrum seems to exclude the involvement of Rydberg state excitation in the I_2 photodetachment process. Since molecular Rydberg states have very long lifetimes, particularly at high excitation energies (from $\approx$ 100 fs for low N to $\sim$ μs for high N), the rapid rise-time of the signal in these experiments also indicates that Rydberg states are not involved in the molecular detachment process.

It is possible to reach a relatively low energy excited state of CH_2I_2 by absorption of a single 312 nm photon. One therefore expects resonance enhancement in the three photon process if the first transition is to this state, which has B_1 symmetry.[129,130,132] If this is the case, the dissociative state reached is expected to be a B_1 electronic state at about 12 eV above the ground state. A B_1 transition in this molecule is aligned along the I – I direction. Although it has been argued that an orbital with B_1 symmetry has a node between the iodine atoms and therefore cannot be responsible for the production of I_2, the total (*i.e.* many electron) wavefunction may nevertheless have electron density between the two iodine atoms. Two-photon resonant enhancement at 312 nm allows access to B_2 (perpendicular to the CH_2 plane) and A_1(parallel to the Z axis) dissociative states; there are no symmetry restrictions on forming a bond between the iodine atoms via transitions having either symmetry.

B. The Products

No evidence of molecular halogen products in any of the lower (valence) states was observed. However, valence states of halogens tend not to be very strongly bound; for example, I_2 has a dissociation energy of 1.54 eV in its ground state, 0.54 eV in its B state and $\approx$ 0.3 eV in its A and A' states.[170] Molecular product in any of these states would dissociate rapidly under the experimental conditions because the available energy is very high. An ion-pair state, which correlates to $X^+ + X^-$, would be a good candidate for a dissociation product because these states are strongly bound and have long range attractive forces. For homonuclear halogens there are eighteen of these, corresponding to the ^3P, ^1D and ^1S terms of the X^+ ion.

First tier ion-pair states of I_2 have equilibrium energies within 0.16 eV of each other.[171] The two other ion-pair families are found approximately 0.9 and 1.5 eV higher.[170] Three photon excitation with 312 nm is equivalent to 12 eV, which translates into an excess energy of $\approx$ 3 eV above the observed barrier to molecular photodetachment at 9.4 eV. This brings all the ion-pair states within energetic reach. The observed data for CH_2I_2 photodissociation indicates that only a small percentage (10%, not corrected for fluorescence yield or detection efficiency) of fluorescence occurs at wavelengths between 250 and 290 nm. These wavelengths correspond to the second tier of ion-pair states, which correlate with $X^+(^3P_0) + X^-(^1S)$.[150] (In the case of CH_2Br_2 and CH_2Cl_2 dissociation, second and third tier ion-pair states fluoresce too far in the UV to be detectable in air.) The observed predominance of the D' state strongly suggests that electronic excitation directly correlates to this state. It may also be the case that dissociation to the D' state is brought about by two-photon resonance enhancement, producing a dissociative state of A_1 or B_2 symmetry as discussed above, but that the f state is a product of the single photon enhancement through B_1 symmetry. One would expect this pathway to produce less I_2 product because formation of an interhalogen bond would not be favoured in this case. However, it is also possible that high-energy excitation of the parent molecule yields a halogen molecule in another ion-pair state while it is still close to the carbene fragment, and that under these circumstances relaxation to the D' state occurs. For example, the dissociation process itself may act as a half-collision. It is known that single collisions of most I_2 ion-pair states with buffer gases are highly efficient in causing non-radiative transitions to the D' state;[146] it is possible that the half-collision represented by

the dissociation may be efficient enough to produce a similar effect. If this were the case, it would explain the observed discrepancy between fits to the dispersed fluorescence spectrum and the vibrational dynamics in the 340 nm region. Halogen molecules in the D' state produced by collisional association would contribute to the observed fluorescence spectrum, but would not necessarily be in phase with those molecules that dissociated directly into the D' state.

3.4.2 Energy Partitioning

If a 12 eV excitation produces I_2 in the D', f, g or G states, only the three lowest electronic states of CH_2, i.e. $\tilde{X}(^3B_1)$ (T_0 = 0.0 eV), $\tilde{a}(^1A_1)$ (T_0 = 0.39 eV), and $\tilde{b}(^1B_1)$ (T_0 = 1.27 eV),[172] are energetically feasible products of the photodissociation process. Table III lists possible combinations of the I_2 and CH_2 states, each of which represents a distinct photodissociation channel of CH_2I_2. For each channel, Table III also gives the minimum energy required for the dissociation process and the remaining energy available for internal and kinetic energy of the photofragments.

From fitting the observed rotational anisotropy data at 272 nm, the I_2 rotational distribution has been found to be centered around j_{max} = 350, which corresponds to an average rotational energy in the product I_2 molecules of approximately 0.3 eV. From fitting the experimentally observed vibrational coherence data, the I_2 fragment has been found to contain only moderate vibrational excitation with an average vibrational quantum number of $v \approx 14$ for I_2 in the f state, or $v \approx 19$ for I_2 in the D' state. With vibrational frequencies on the order of 100 cm^{-1}, we can therefore estimate that the

Table III. Energetics for several dissociation channels of CH_2I_2.[130,150,155,156] The table gives the minimum energies required to dissociate a ground state CH_2I_2 molecule to produce CH_2 and I_2 fragments in several possible electronic states. The available energies are calculated based on a three photon transition at 312 nm.

I_2 States	**CH_2 States**	**Energy Required (eV)**	**Available Energy (eV)**
D' ($^3\Pi_{2g}$)	$\tilde{X}\ ^3B_1$	8.38	3.62
	$\tilde{a}^1A_1$	8.77	3.23
	$\tilde{b}^1B_1$	9.65	2.35
f ($^3\Pi^+_{0g}$)	$\tilde{X}\ ^3B_1$	9.20	2.80
	$\tilde{a}^1A_1$	9.59	2.41
	$\tilde{b}^1B_1$	10.47	1.53
g ($^1\Sigma_{0g}$+)	$\tilde{X}\ ^3B_1$	10.2	1.8
	$\tilde{a}^1A_1$	10.6	1.43
	$\tilde{b}^1B_1$	11.5	0.55
G(1_g)	$\tilde{X}^3B_1$	9.27	2.65
	$\tilde{a}^1A_1$	9.66	2.26
	$\tilde{b}^1B_1$	10.54	1.38

energy partitioned into vibrational excitation of the I_2 fragment is approximately 0.2 eV in both cases. The small vibrational energy in the I_2 fragment can be attributed to the fact that the I – I distance in CH_2I_2 is 3.57 Å, very similar to that of I_2 ion–pair states;[141,150,155,156] little vibrational excitation is then expected.

The fragments therefore contain at least 1.8 eV of translational and internal energies. With the assumption of a three–photon excitation and of I_2 in one of its second tier ion–pair states f, g or G, the formation of CH_2 ($\tilde{b}$) can be ruled out because there is not enough energy available (see Table III). If this is the case, we are left with a limited number of choices, *i.e.* CH_2 ($\tilde{X}$) + I_2 (f, g, G) and CH_2 ($\tilde{a}$) + I_2 (f, g, G). Which of these channels is responsible for photodissociation of CH_2I_2 to yield I_2 fluorescence at 272 nm remains to be investigated.

Because the HCH angle in ground state CH_2I_2 differs significantly from the bond angle of CH_2 in the $\tilde{X}$ and $\tilde{b}$ states,[141] vibrational excitation should be expected in the CH_2 photofragment if it is produced in either of these states. This could represent a significant amount of energy, especially when one considers the high vibrational frequencies of CH_2.

3.4.3 Mechanism

Femtosecond studies of the reaction dynamics of Rydberg states of methyl iodide showed a substantial difference in reaction time for the photodissociation of CH_3I and CD_3I.[75] The explanation proposed for this observation was that vibrational modes in the

alkyl fragment are involved in the predissociation process, thus making the isotope effect for the dissociation substantial. Photodissociation studies of alkyl iodides at 304 nm excitation energy also revealed that the partitioning of available energy into IVR increased from 19% for methyl iodide to 70% in n-butyl iodide, an energy difference of 1 eV.[173,174] Both findings contrast directly with our results, which indicate no apparent increase in IVR in the alkyl fragment on going from diiodomethane to gem-diiodobutane (*vide supra*). Furthermore, within experimental resolution the dissociation time for CH_2I_2 and CD_2I_2 was found to be the same. Reduced mass considerations alone predict that CD_2I_2 will dissociate $\approx$ 3 fs slower than CH_2I_2, which is well within the experimental resolution. This is strong evidence that vibrational modes in the alkyl fragment are not involved in the dissociation.

The short time photodissociation dynamics for breaking of a single C – I bond of CH_2I_2 have been studied recently by many groups using both femtosecond time–resolved techniques[72,136] and resonance Raman spectroscopic measurements.[134,135,137,138] It was found that the dissociation process takes place in less than 120 fs[72,136] and that the I–C – I symmetric stretching mode is initially activated, which leads to breaking of one of the two C – I bonds by coupling to the I–C – I antisymmetric stretching mode.[134,135,137,138]

In order to investigate the possible contribution of various vibrational modes of the parent molecule to the molecular detachment process, a frequency analysis of the ground-state equilibrium geometry of CH_2I_2 was performed using GAUSSIAN 94.[175-177] Table IV compares the normal mode frequencies of the calculated gas phase values to the

experimental liquid[178] and solution phase values.[137] Despite the fact that the calculated and experimental values are determined for different phases, it can be seen that the calculated frequencies are close to the experimentally observed ones (0.1 - 9% deviation). The larger errors occur for those modes involving mostly iodine atom motion. This is not unexpected, because *ab initio* calculations on molecules containing many-electron atoms like iodine are inherently less precise.

Table IV. Comparison of theoretical and experimental CH_2I_2 vibrational energies in cm^{-1}.

Mode	Description	Calculated	Experimental		
		Gas phase	Liquid CH_2I_2 (Raman)	Liquid CH_2I_2 (Infrared)	Solution (Raman)
ν_4	I-C-I bend	117	121		134
ν_3	I-C-I symmetric stretch	454	486	486	493
ν_9	I-C-I asymmetric stretch	552	567	573	581
ν_7	CH_2 rock	716	714	717	714
ν_5	CH_2 twist	1056	1028		1028
ν_8	CH_2 wag	1148	1104	1106	
ν_2	H-C-H bend	1374	1350	1351	1369
ν_1	H-C-H symmetric stretch	2958	2968	2967	2968
ν_6	H-C-H asymmetric stretch	3043	3049	3049	3049

Figure 3.26 shows the results of the normal mode analysis, plotted as a function of I - I and CH_2-I_2 distance. For each mode, the amplitude of the motion corresponds to one

quantum of excitation in that mode. It is apparent that only the I-C-I bending and I-C-I symmetric stretching modes, ν_4 and ν_3 respectively, contribute to the I - I interatomic distance. The other normal modes produce little or no change in the distance between the iodine atoms, which is further evidence that these modes are not involved in the molecular photodetachment process. The I-C-I bending ν_4 contributes significantly to the $H_2C \ldots I_2$ coordinate. Because this is the lowest energy mode, it is expected to be significantly populated at room temperature; at 294 K approximately 10 % of the molecules have four quanta in this mode. A reaction coordinate that mimics the motion the molecule undergoes when ν_4 is excited is therefore a reasonable candidate for the photodetachment mechanism.

The two mechanisms shown in Figure 3.27 are both concerted; in other words, breaking of the two C – I bonds and formation of the I – I bond happen in a single kinetic step. The difference between the two is that one preserves the C_{2v} symmetry of the parent molecule CH_2I_2, while the other proceeds through a bent geometry and does not. In this situation, one of the C – I bonds breaks earlier, or to be more precise, faster than the other. The synchronous concerted mechanism shown in Figure 3.27 (a) conserves the C_{2v} symmetry of CH_2I_2. According to this mechanism, CH_2 flies away along the symmetry axis, which passes through the center of mass of CH_2I_2. The impact parameter *b* would in this case be zero, and no rotational excitation is expected in the halogen fragment. On the other hand, the asynchronous concerted mechanism shown in Figure 3.27 (b) does yield a nonzero orbital angular momentum because in this case *b* is finite.

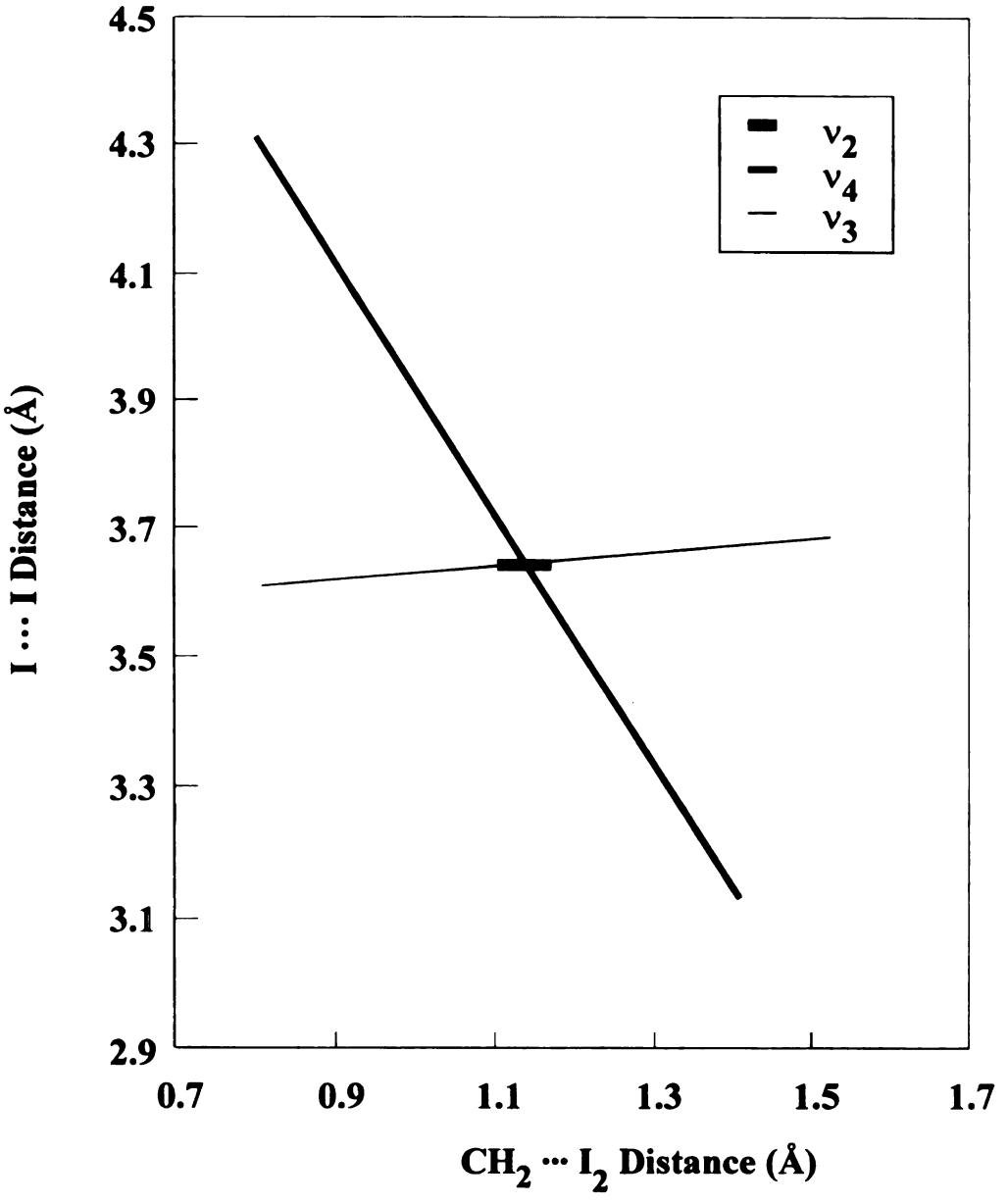

Figure 3.26 Normal mode analysis of the ground state of CH_2I_2, plotted as a function of I-I and CH_2-I distance. Only the I-C-I bending (ν_4) and I-C-I symmetric stretch (ν_3) modes contribute to the H_2C-I_2 distance.

The data collected from the CH_2I_2 cell at 272 nm exhibits a high degree of rotational excitation in the nascent I_2. In this case, based on an estimated 1.26 eV of translational energy and the 250 $\hbar$ of angular momentum determined from the rotational anisotropy, the impact parameter b can be estimated to be approximately 2.7 Å. This clearly indicates that the molecular detachment process which produces the I_2 molecules that fluoresce at 272 nm happens according to the asynchronous concerted mechanism. It was however not possible to reliably analyse the rotational excitation in the I_2 fragment detected at 340 nm. For this reason, we cannot with any degree of confidence assign a mechanism to the reaction $CH_2I_2 \rightarrow CH_2 + I_2(D')$, at least not based on the analysis of the rotational anisotropy of the I_2 fragment.

A Hückel frontier molecular orbital study of the dissociation of CX_2Y_2[128] at lower energies indicated that the 'least-motion' path (in which C_{2V} symmetry is retained) is a high-energy pathway and that when the carbene moiety is allowed to slip off-centre from the halogen-halogen axis, the reaction path is considerably stabilized.[128] This corresponds to a pathway for the concerted elimination of the general type shown in Figure 3.27 (b).

Because the carbene radical is ambiphilic, *i.e.* the lone pair at the front of the radical behaves as a nucleophile and the empty $p\pi$ orbital is electrophilic, an asynchronous concerted mechanism would tend to produce charge separation in the halogen fragment.[128] This is consistent with the fact that only ion-pair states of halogen molecules have been observed on the photodetachment of halogens from dihaloalkanes. In this case, an ylide-type transition state would be stabilised by the charge distribution of the carbene

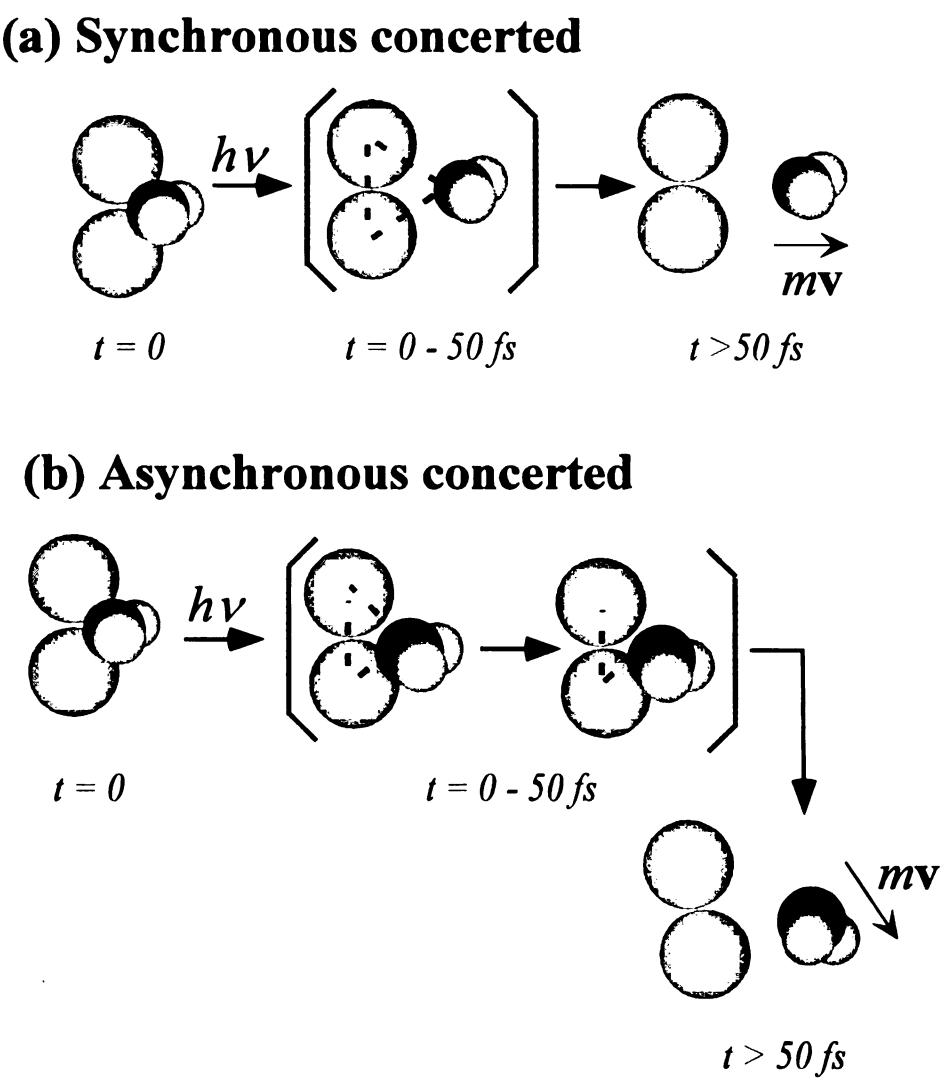

Figure 3.27 Schematic of possible mechanisms for the photoinduced molecular detachment of X_2 from gem-dihaloalkanes. Both proceed in a single kinetic step. The time scales given for these mechanisms are based on time-resolved measurements.

(a) Synchronous concerted mechanism. Breaking of the two carbon-halogen bonds is initiated at the same time and proceeds at the same rate. An interhalogen bond forms before the carbon-halogen bonds are completely broken. This pathway has a symmetric transition state and preserves the C_{2v} symmetry of the parent.

(b) Asynchronous concerted mechanism. In this case, the rate at which the two carbon-halogen bonds break is different. Again, the interhalogen bond forms before the halogens are completely dissociated from the carbene.

fragment. Iso-diiodomethane, H_2-C – I - I, has been observed in gas matrices at low energies;[179] in calculations of this system, it was found that less than 2 eV of excitation energy is required to produce this species. This is less energy than is needed to form CH_2I + I.[140] However, the bonding between the iodine atoms in this species is significantly weaker than in I_2 or I_2^-, which may explain why CH_2 + 2I are the more common reaction products. The iodine atoms in this molecule are described as a contact ion pair in which the charges are mostly concentrated on the iodine atoms; there is little redistribution of charge on the carbon atom.[140] This is also consistent with a charge-transfer mechanism.

One would expect a direct recoil pathway to allow relatively efficient coupling between the α- carbon and the internal modes of the alkyl fragment, in which case a significant difference in IVR rate would be observed between methylene and butylene iodide. This may however be defeated in $RCHI_2$ both by the very rapid rate of reaction and by the large difference in vibrational frequency between modes involving primarily the C-I and C-C or C-H bonds.

Cain *et al.* also found that the barrier height for $CX_2 + Y_2 \rightarrow CX_2Y_2$ (where Y denotes a halogen atom) or the reverse process depends on the HOMO–LUMO gap of the halogen molecule Y_2.[128] The lower the gap, the lower the barrier. Since the HOMO–LUMO gap decreases from F_2 to I_2, they concluded that the barrier decreases from CX_2F_2 to CX_2I_2, resulting in a corresponding decrease in rotational excitation. This leads to the prediction that there will be an increase in rotational excitation on traversing the series from CH_2I_2 through CH_2Br_2 to CH_2Cl_2. Unfortunately, it wasn't possible to analyse the

anisotropic data from the D' state of either I_2 or Cl_2, so this prediction can not currently be tested.

The possibility of a third mechanism has also been investigated. If we assume that it requires one 312 nm photon to dissociate one of the C – I bonds and a second to dissociate the other C – I bond, the third photon could then be said to cause photoassociation between the two iodine atoms thus produced. This will be called a three–step mechanism. The difference between this mechanism and the asynchronous concerted mechanism has to be emphasised. In the asynchronous concerted mechanism, absorption of the three photons happens simultaneously and instantaneously. The bond breaking and bond formation events then take place after absorption of the three photons. Since the photodissociation processes happen within the time duration of the pulse, we can not directly distinguish the two possibilities experimentally unless much shorter laser pulses are used. Therefore, in order to distinguish between them, the dynamics resulting from each mechanism were simulated as described in Appendix B.

As far as the photoinduced molecular detachment processes in this study are concerned, the penta–atomic molecule CH_2I_2 can be treated as a triatomic with the CH_2 moiety being viewed as a pseudo atom. In Appendix B it is assumed that the bonds are rigid and that there is no translation or rotation of the system as a whole. Excess energy deposited to dissociate a bond is assumed to be manifested as a force acting along the direction of the bond (*i.e.* axial recoil). Therefore, it is sufficient to consider only the motion of the atoms on the triatomic plane.

Figure 3.28 Classical simulations of molecular detachment processes. In each snapshot, the large spheres represent the iodine atoms and the small sphere represents the CH_2 moiety. In both mechanisms, the two C – I bond breaking events are assumed to be separated by 32 fs.

(a) The three–step mechanism. The excess energy is estimated to be 1. 8 eV for the first bond breaking event and 0.3 eV for the second. In this case, the I – I bond is assumed to form immediately after the second C – I bond breaks.

(b) The asynchronous concerted (ylide) mechanism. The excess energy is estimated to be 2.7 eV for the first bond breakage and zero for the second. The I – I bond is assumed to form immediately after the first bond breaking event.

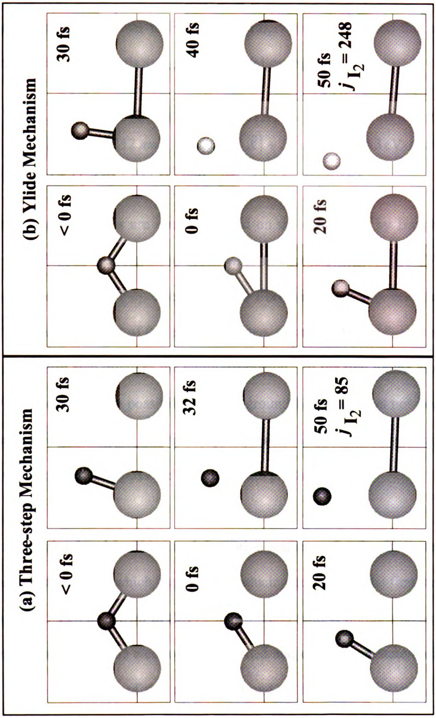
(a) Three-step Mechanism
< 0 fs
30 fs
0 fs
32 fs
20 fs
50 fs
$j_{I_2} = 85$
(b) Ylide Mechanism
< 0 fs
30 fs
0 fs
40 fs
20 fs
50 fs
$j_{I_2} = 248$

Figure 3.28

Figures 3.28 (a) and (b) present the simulated results for the two mechanisms. To obtain the simulation shown in Figure 3.28 (a), we have assumed that the molecular detachment process proceeds according to the following three steps:

$$\begin{cases} CH_2I_2\left(\tilde{X}\right) + h\nu\left(312\,nm\right) \rightarrow CH_2I\left(\tilde{X}\right) + I\left(^2P_{3/2}\right) + 1.8\,\text{eV} \text{ at } t=0 \\ CH_2I\left(\tilde{X}\right) + h\nu\left(312\,nm\right) \rightarrow CH_2\left(\tilde{X}\right) + I\left(^2P_{1/2}\right) + 0.3\,\text{eV} \text{ at } t=32\,fs \\ I\left(^2P_{3/2}\right) + I\left(^2P_{1/2}\right) + h\nu\left(312\,nm\right) \rightarrow I_2(f) + 0.6\,\text{eV} \end{cases} \quad (3.11)$$

where the excess energies are obtained based on the data given by Baughcum *et al.*[130] The first C – I bond is assumed to break with an excess energy of 1.8 eV to produce I atom in the ground state $^2P_{3/2}$. The second C – I bond is assumed to break at 32 fs later[37] and with an excess energy of 0.3 eV. In this step, excited I atom ($^2P_{1/2}$) is assumed to be formed. The third step involves the photoassociation[68] of the two iodine atoms to form I_2 in the *f* excited state. The possibility of two ground I products has not been considered because photoassociation in the third step to produce I_2 (*f*) from two ground state iodine atoms is not energetically possible with a 312 nm photon.

An alternative bond breaking and formation sequence for the three-step mechanism was also investigated, in which, instead of producing ground I in the first step and excited I in the second step as shown in (3.11), the first and second photons break both carbon-iodine bonds and form one electronically excited and one ground state iodine atom. The results from a simulation of this mechanism and of the pathway shown in (3.11) both predict an I_2 angular momentum that is inconsistent with experimental observations (*vide infra*). Because of this, only the pathway described in (3.11) will be considered in the following discussion.

The energetics shown in the following equation have been used for the simulation of the asynchronous concerted mechanism in Figure 3.27 (b).

$$CH_2I_2 + 3h\nu(312\ \text{nm}) \rightarrow CH_2 + I_2(f) + 2.7\ \text{eV}. \qquad (3.12)$$

Here the excess energy is taken from Table III. The first C – I bond is assumed to break with an excess energy of 2.7 eV. At 32 fs later, the second C – I bond is assumed to break with no excess energy.

Each snapshot in Figures 3.28 (a) and (b) depicts the spatial arrangement of individual atoms (the CH_2 moiety is treated as a pseudo atom) and their bonding configuration at a particular instance. Here, notice that the time reference is chosen to be the instance when the first bond breaks and it may not coincide with the experimental time zero, which is the instance when the pump transition takes place.

Aside from facilitating visualisation of the molecular detachment process, a more important purpose of the simulation is to obtain a quantitative estimate of the orbital angular momentum L. This then allows one to compare the estimated L with that obtained from analysis of the experimental data. Since the three (pseudo) atoms in CH_2I_2 are assumed to be motionless before the first bond breaking in this simulation, the triatomic system contains no total angular momentum and will continue not to do so because of conservation of angular momentum. Thus the orbital angular momentum L is the same as the I_2 angular momentum in magnitude but opposite in sign. With a time lag of 32 fs between the two bond breaking events, an I_2 angular momentum of $85\hbar$ is predicted

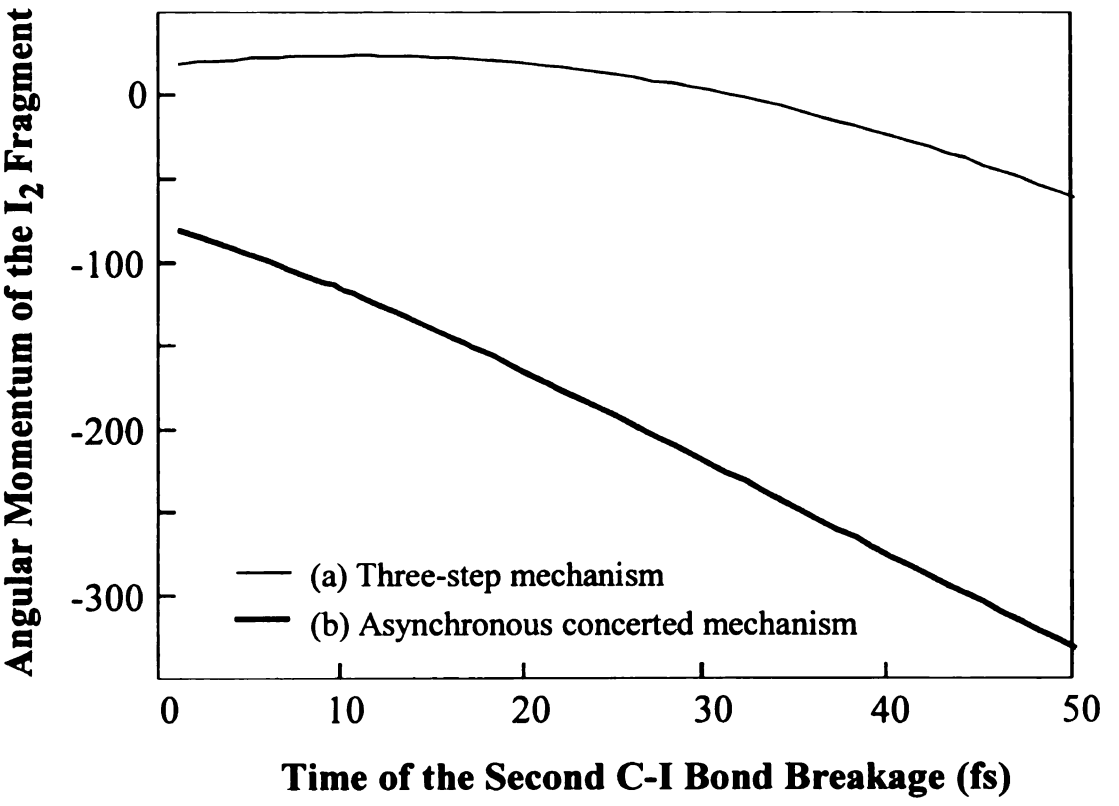

Figure 3.29 Dependence of I_2 angular momentum on the time lag between the two bond breaking events. The two traces present the dependencies for the asynchronous concerted mechanism (a) and the three–step mechanism (b). The conditions are as stated for Figure 3.26.

from the three–step mechanism, Figure 3.28 (a) and 248 $\hbar$ from the asynchronous concerted mechanism, Figure 3.28 (b). Figure 3.29 examines how the time lag affects the angular momentum of the I_2 fragment. This figure and Figure 3.27 clearly show that the asynchronous concerted mechanism predicts an I_2 angular momentum that is more in agreement with experimental observations.

4. PHOTOASSOCIATION

4.1 Introduction

4.1.1 Bimolecular Reactions

Many spectroscopic studies on the dynamics of chemical reactions examine the photodissociation process, in which the molecule of interest undergoes a unimolecular decomposition. Of more general interest however are bimolecular, or full-collision, reactions in which two or more free, unbound reactants form a collision complex, undergo structural, energetic and electronic changes as a result of the interaction between them, and separate into fragments. Bimolecular reaction dynamics have typically been investigated by molecular beam techniques, in which the states of reacting species can be quite carefully controlled and the nature of the products accurately measured. However, as discussed in the Introduction, this approach allows only the asymptotic properties of the system to be examined. While this certainly yields some information about the nature of the transition state region, it is vital to a proper understanding of reaction processes to determine what happens while the reactive species are interacting with each other. Because the collision complex (hereafter called transition state complex) is typically short-lived, the processes occurring during its lifetime are difficult to measure directly, but they are vital to the progress of the reaction.

A bimolecular reaction can be thought of as a sequence of half-collisions; the reactants first combine with each other to form a collision complex which then undergoes

the requisite changes before dissociating to form products. In principle, either or both of these processes may be investigated spectroscopically. To interrogate the second 'half' of the full-collision reaction, it is possible to use photodissociation, which is a very common, and useful, method of studying what occurs when a species undergoes fragmentation to form products. The analogous technique for examination of the first process discussed above is photoassociation, which is considerably less extensively applied. It is photoassociation which is of interest to this study.

4.1.2 Photoassociation

Photoassociation occurs when the absorption of a photon by a collision pair induces bond formation between them.[66,180-183] The process can be described as truly bimolecular when the reactants are free and unbound prior to initiation of the reaction. Photoassociation is distinct from other types of photoinduced reaction because the reacting species absorb the light cooperatively; a sequential process in which one body is excited and subsequently reacts with the other is described as a laser-assisted or photoinduced rather than photoassociation reaction. To avoid ambiguity, it is therefore important to ensure that neither of the reacting species absorbs the light independently of the other; excitation and bond formation are cooperative and concurrent. For this reason, the frequency of the light is carefully chosen so as to be resonant with a transition of the transition state complex but not with either of the reactants.[2] This condition ensures that the transition state complex is excited directly. The efficiency of product formation and the nature of the products should then be sensitive to the form of the reactive potential energy surface. Monitoring the properties of the reaction products as the photoassociation

energy is tuned therefore provides a sensitive probe of the transition state region for the bimolecular reaction.

Photoassociation spectroscopy has been used for a number of purposes, for example to study the electronic excited states of species having repulsive ground states.[184-188] A number of frequency-resolved photoassociation studies exist on the long-range interactions between ultracold atoms as a means to elucidate details about the ground-state potential of alkali metal dimers near the dissociation limit.[189-193] 'Collision-induced absorption' is a consequence of photoassociation, and has been described in some detail.[62,63] The gas-phase reactions of metal atoms with H_2[194-197] and on salt surfaces[198,199] have been studied by this method. Additionally, the possibility exists to use excimers which undergo a radiative transition to the ground state as lasing media; several investigations have therefore been conducted on these types of systems.[65,200-202] Photoassociation has obvious potential in directing the outcome of chemical reactions, and a number of theoretical studies exist on the possibility of using it for this application.[69,87,203,204] Experimental results have been demonstrated in the frequency-resolved regime for the Penning ionisation of Li[64] and for energy transfer,[205,206] for example.

Unlike photodissociation, which is generally amenable to study by time-resolved methods, real-time observation of photoassociation reactions presents difficulties. There are several reasons for this. Because the irradiation time is short, the number of collision pairs which can be associated within the pulse essentially depends on the spatial

distribution and relative momenta of the atoms at the moment when the pulse is switched on. In a gas phase sample this number may be prohibitively small. A more fundamental problem arises as a result of the nature of the ground state, which is composed of a thermal ensemble of continuum states and will therefore contain a broad distribution of positions and momenta. As a result of this, it may not be possible to prepare a well-defined wavepacket on the excited state potential energy surface. The 'time zero' or initiation time of a bimolecular reaction is also ambiguous because the species are undergoing random motion, which introduces a spread in both the energy and timing of the reaction. These drawbacks have to some extent been circumvented by the use of precursors.[55,57,58,207] These are generally van der Waal's complexes which undergo a full collision reaction upon liberation of one of the reactants from the complex, or following photoactivation of an atom.[56] In this way, the collision geometry and initiation time of the reaction are clearly defined. A number of such harpooning or laser-assisted reactions have been studied experimentally.[2,48,57,207-210] While this approach overcomes many of the drawbacks to studying bond formation processes by time-resolved methods, it involves absorption of light by a precursor before the reaction can occur, not direct excitation of the transition state complex. Reactions of this type are therefore not photoassociative.

A number of theoretical studies exist on the possibility of directly probing photoassociation dynamics in real time.[67,211,212] These however deal with the ground state as a coherent superposition of states, which is not likely to be valid in the case of a thermal gas sample at ambient temperature.

When a pulse of sufficiently short time duration excites a molecule, a coherent superposition of eigenstates or wavepacket is produced. In the case of a free → bound (photoassociation) transition, where the initial excitation is from a set of continuum states, well localised wavepackets can be formed on the excited state surface as long as there is a large enough difference in the slope between the upper and lower electronic states. The Franck-Condon factors of the transition dictate that photoassociation probability is greatest when the laser wavelength is resonant with the energy difference between the ground and excited state energies, which imposes a spatial and energetic restriction on the reaction. Tuning of the wavelength of the binding pulse can thus be used to select a range of reactive impact parameters. Temporal resolution is afforded by the binding pulse, and is limited only by the pulse duration. Molecular dynamics following photoassociation can thus be probed using the same techniques that have been used for bound → free or bound → bound transitions.[68,213] Results are presented below on the application of this method to the formation of Hg_2*.

In this work, experimental observations of photoassociation investigated by time-resolved pump-probe spectroscopy are presented. The system selected for these studies was gas-phase mercury atoms, which have the potential to form electronically excited molecular dimers.

4.1.3 The Mercury Dimer

The spectroscopy of Hg_2 has been extensively studied, both experimentally[70,202,214-228] and by computational methods.[200,229,230]. The ground $X(0_g^+)$ state is almost purely

repulsive, having a well depth of 370 cm^{-1}, representing the formation of Van der Waal's dimers at an internuclear separation of 3.63 Å.[216,218,222] The first ungerade molecular state accessible from the ground state is the $D1_u(^3\Sigma_u^+)$ state,[216,218,222] which correlates with $Hg(^1S_0)$ + $Hg(^3P_0)$.[221] The $D1_u$ state is characterised by a broad, intense fluorescence centred at 335 nm (29,850 cm^{-1}), which has been observed by nanosecond excitation of mercury vapour in a molecular beam.[214-216] The second harmonic of our CPM is at 312 nm, which corresponds to 32,050 cm^{-1}. This is resonant with the $X(0_g^+) \rightarrow D1_u$ transition in Hg_2; it should therefore be energetically possible to cause photoassociation to produce Hg_2 using 312 nm pulses. The molecular product would be easily detectable by observation of fluorescence at 335 nm, and the repulsive ground state prevents the accumulation of molecular products, allowing the use of a static cell. The relatively high vapour pressure of mercury also avoids the necessity to use prohibitively high experimental temperatures. For these reasons, mercury vapour was considered to be a suitable system for a study of photoassociation on the femtosecond time scale.

4.2 Experimental

For these experiments, a sample cell very similar to the one described previously for the photoinduced molecular detachment reactions was used. However, it is particularly important in these experiments to exclude gaseous impurities, particularly air, to avoid problems associated with spurious fluorescences and quenching of Hg_2 emission.[231,232] Because there are no problems associated with buildup of molecular product for this

system it was therefore decided to prepare a permanently sealed cell for these experiments.

The mercury sample, triply vacuum distilled and certified to contain a total of less than one part per million impurities (Bethlehem Apparatus Co.), was introduced to a thoroughly cleaned and vacuum baked glass line by injection over an argon atmosphere. The injection port was then sealed and the sample pumped to 10^{-5} Torr. Mercury was transferred to the sample cell by distillation under vacuum, until an amount substantial enough to be able to form a reservoir was collected. The portion of the line containing the quartz cell and a 'U' trap was then closed to the rest of the pumping station and immersed in liquid nitrogen to achieve cryopumping while the cell was sealed off. The purity of the sample was checked by LIF in the 190 to 850 nm region at high laser intensity. Fluorescence from the cell showed some atomic mercury lines (resulting from multiphoton excitation); no spectral evidence of contamination in the sample was found.

In order to raise the vapour pressure of the sample, the cell was wrapped in heating tape and maintained at a constant temperature throughout the experiment. The cell temperature was monitored externally by thermocouples placed in two positions; the first beside the liquid reservoir, to get a measure of the vapour pressure inside the cell, and the second as close as possible to the laser interaction region in order to determine the energetics of the reaction. Raising the cell temperature has the additional advantage of imparting sufficient thermal energy to the unbound ground-state mercury atoms to raise

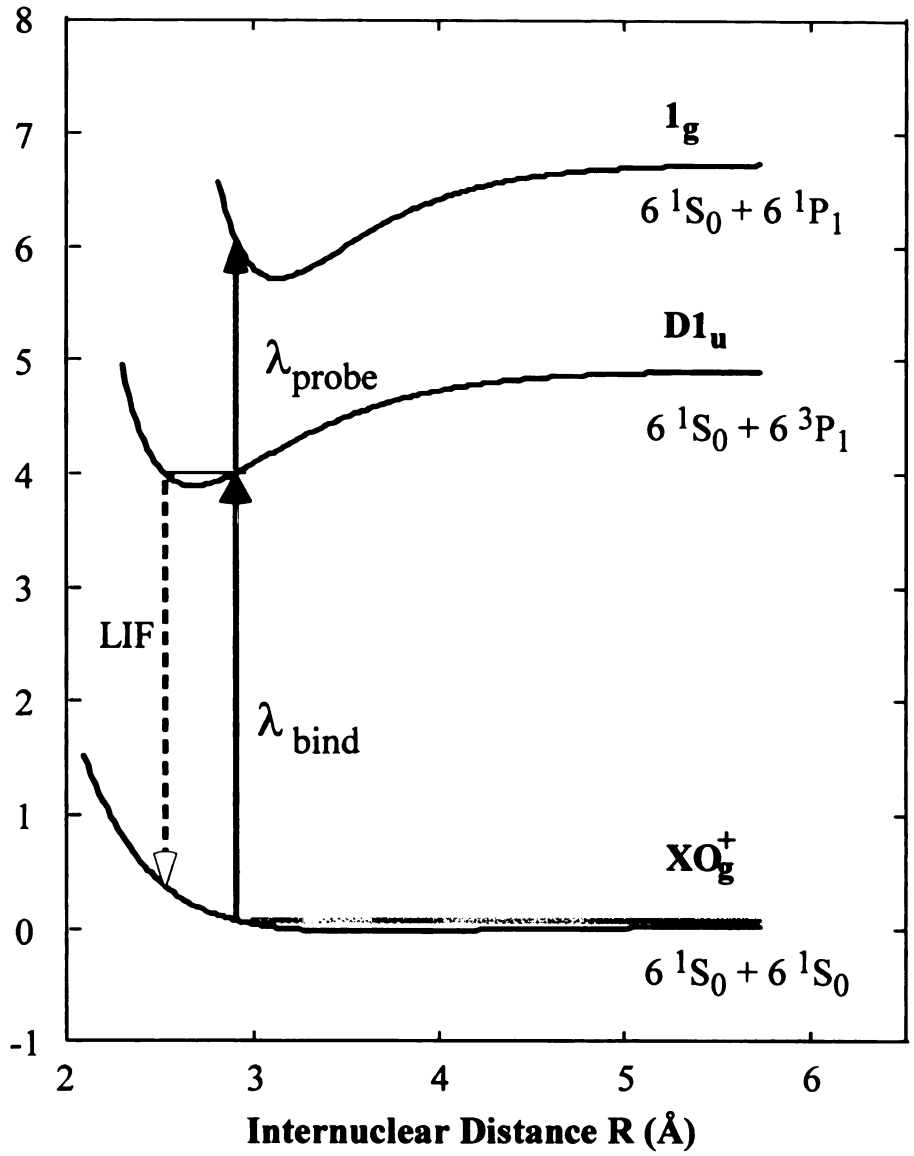

Figure 4.1 Schematic of the potential energy surfaces relevant to the femtosecond photoassociation of mercury atoms. The corresponding atomic states at the asymptotic limits are indicated.

them above the shallow well in the molecular X state. Most of the results were obtained at 160° C, which corresponds to a mercury vapor pressure of 4.2 Torr.[233]

A schematic of the potential energy surfaces involved in the Hg-Hg photoassociation process is shown in Figure 4.1. Because the ground state of Hg_2 is repulsive, molecules in this state exist as separated atoms. Pairs of atoms will then be located on the ground state potential energy surface according to their separation distance and the amount of thermal energy they possess; for convenience these can be termed collision pairs. There will be a finite Franck-Condon factor for excitation from the appropriate region of the ground state to the $D1_u$ state of Hg_2. It is expected therefore that collision pairs with the appropriate internuclear distance and combined thermal energy to be located in the optically coupled region of the 312 nm pulse can be photoassociated to the molecular $D1_u$ state. This can be verified by observation of the characteristic $D \rightarrow X$ fluorescence at 335 nm. Also shown (inset) is the region ΔR_x of most probable excitation based on the average thermal energy kT of the atoms and on the spectrum of the binding pulse. Notice that the narrow range of interatomic distances captured by the excitation process is in the repulsive part of the ground state potential, above the dissociation energy of the dimer.

Once the Hg_2^* excimers are formed, molecular dynamics can be probed by fluorescence depletion using a second femtosecond pulse at 624 nm. There is a high density of electronic states in Hg_2 at energies above 32,000 cm^{-1}, which means there is a good chance that the probe pulse energy will correspond with a resonance from the $D1_u$ state to some higher-lying molecular state. The state represented in the figure corresponds

to the 1_g state of Hg_2, which has been observed ≈ 2 eV above the $D1_u$ state[230,234] and has the correct parity for a single-photon transition from this state.

4.3 Results and Discussion

4.3.1 Spectroscopy

Presented in Figure 4.2 (a) is the dispersed fluorescence spectrum obtained from the mercury cell by excitation with the fourth harmonic of the Nd:YAG laser at 266 nm. Light at this wavelength is resonant with the $6\ ^1S_0 \rightarrow 6\ ^3P_0$ transition of mercury atoms, and will cause excitation of some of the mercury in the vapour. Three-body collisions with other atoms and with the walls should then produce excimers in the $D1_u$ state. The reason for collecting this spectrum in addition to the one obtained under 312 nm excitation is to compare the appearance of the spectra and thereby confirm whether or not the $D1_u$ state of Hg_2 is producing the fluorescence. The 266 nm pulses are ≈ 5 ns in duration and should produce a significant population of $Hg(6\ ^3P_0)$ and consequently $Hg_2(D1_u)$. The spectrum shown in Figure 4.2 (a) is characteristic of Hg_2 $D \rightarrow X$ fluorescence.[214-216] The spectrum produced by excitation of the mercury cell with a 60 fs pulse at 312 nm is presented in Figure 4.2 (b). This is also a characteristic $D \rightarrow X$ spectrum; the lower signal:noise in the second spectrum is a consequence of lower fluorescence intensity. The population of $Hg_2(D1_u)$ producing the spectrum in Figure 4.2 (b) is somewhat red-shifted relative to the spectrum produced by excitation at 266 nm, which is not unexpected given the difference in excitation energy. Power dependence measurements indicated that there is a linear dependence of fluorescence on the intensity

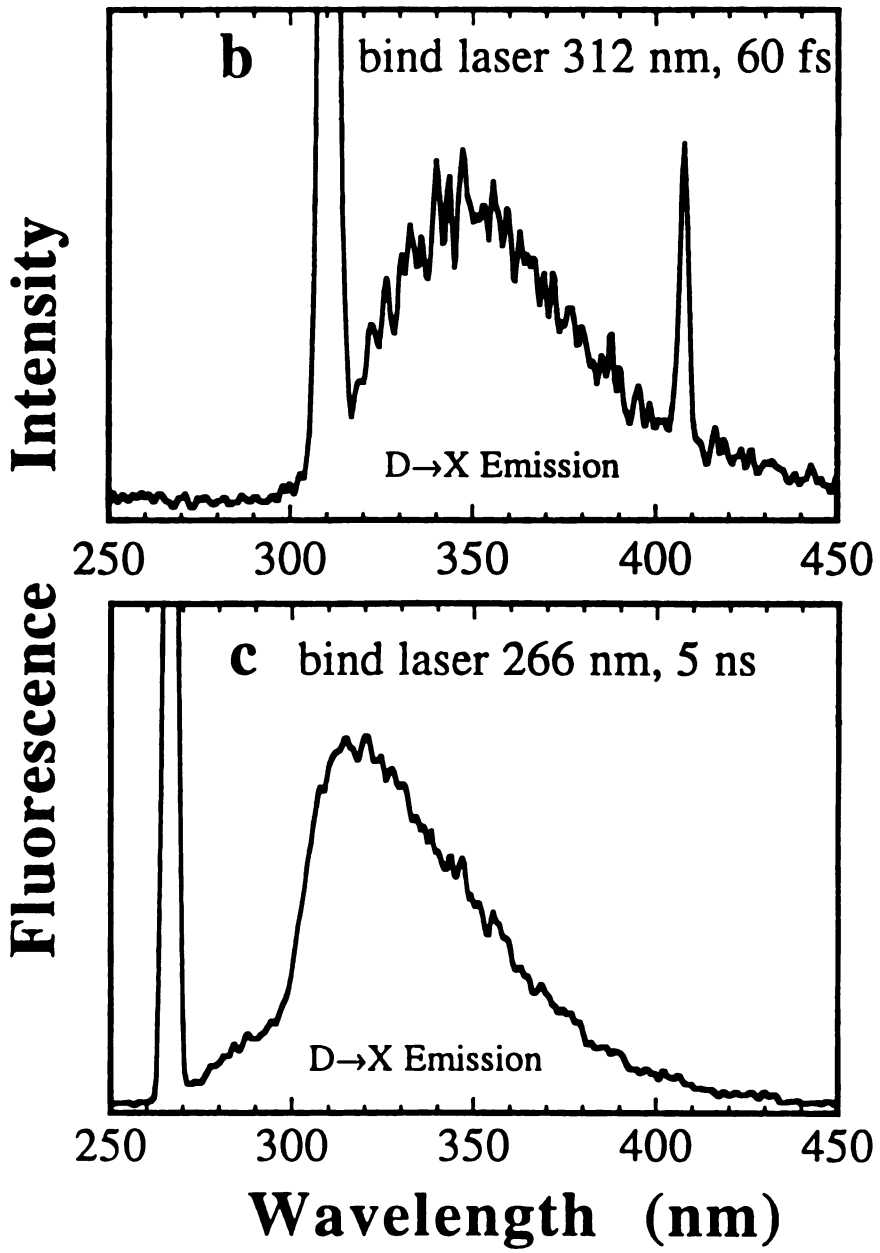

Figure 4.2 Dispersed fluorescence spectra resulting from the excitation of mercury vapor in a static cell at 160 °C.

(a) Excitation at 266 nm with a nanosecond laser pulse.

(b) Using a 60 fs laser pulse centred at 312 nm. The D → X emission is red-shifted compared to the emission produced by 266 nm excitation because of the difference in excitation energy. The peak at 407.8 nm is an atomic line resulting from two-photon excitation to the 7^1S_0 state.

of the 312 nm pulse. It is apparent by comparison of Figures 4.2 (a) and (b) that excitation of atomic mercury vapour with a 312 nm femtosecond pulse produces Hg_2. It remains to verify the mechanism of this process.

4.3.2 Dynamic Behaviour

To determine the dynamics of the Hg_2 formation process and the molecular dynamics of the nascent product, pump-probe experiments were performed with 312 nm pulses as the pump and 624 nm pulses acting as the probe. Fluorescence data were collected at 340 nm with the probe laser polarised both parallel and perpendicular to the pump. The results are shown in Figure 4. 3. The data were normalised to the same level at negative times, since the fluorescence intensity when the probe pulse precedes the pump should be insensitive to the polarisation of the lasers relative to one another. At negative times, the fluorescence signal produced by photoassociation into the $D1_u$ state is unaffected by the depletion (probe) pulse, which precedes it. As time zero is approached, depletion of the molecular fluorescence begins to be apparent as molecules in the $D1_u$ state absorb the 624 nm pulse and are excited into a higher energy electronic state. Figure 4.3 indicates that the possibility for depletion persists for at least five picoseconds.

Two aspects of the figure are worthy of particular attention. First, it should be noted that the onset time of the depletion is very rapid, being completed within $\approx$ 200 fs. This observation implies that the process responsible for the portion of the fluorescence being depleted also takes place on a femtosecond time scale. As discussed above for the case of I_2 formation from CH_2I_2 (*vide supra*), the time of onset of the depletion can be used to

obtain a direct measure of the bond formation time. Fitting to the isotropic portion of the data revealed that the molecule formation time is within the pulse.

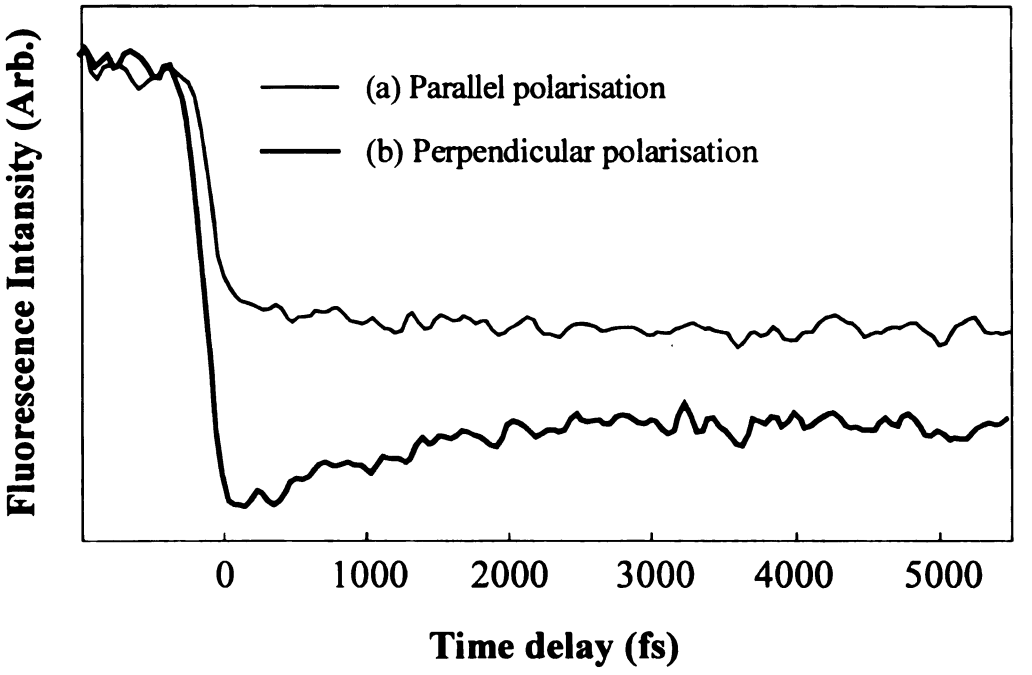

Figure 4.3 Femtosecond pump-probe transients from the photoassociation of mercury at 312 nm. Data was collected with the probe laser polarised parallel (a) and perpendicular (b) to the binding laser. Note that bond formation occurs during the pulse and that the data is clearly anisotropic, indicating alignment of the nascent molecules.

The second point is the observed anisotropy in the data. If photoassociation is occurring, the pump pulse would produce Hg_2 molecules selectively aligned according to a cosine squared distribution about its polarisation direction (assuming a parallel transition). The probability for absorption of the probe pulse and consequent fluorescence depletion would then be greater when the probe pulse was polarised parallel to the pump than when it was perpendicular. For the case of parallel polarisation direction, the depletion probability would be expected to be at a maximum immediately after time zero, when the molecules still retained their initial alignment, and would gradually decrease in

time as they rotate away from the position of maximum alignment with the laser field direction. The data shown in Figure 4.3 has a dephasing time τ_c of $\approx$ 1.1 ps. The observed anisotropy and time evolution of the data clearly indicate rotational coherence in the nascent Hg_2 molecules.

The rotational anisotropy $r(t)$ of the transients can be extracted using the weighted difference[36]

$$r(t) = \frac{I_{\parallel} - I_{\perp}}{I_{\parallel} + 2I_{\perp}}; \tag{4.1}$$

the result is shown in Figure 4.4. The observed dephasing of rotational anisotropy can be analysed using a simple model which treats the rotational population P_j as a Gaussian:

$$r(t) = \sum_{J=0}^{\infty} r(j,t) P_j, \tag{4.2}$$

where

$$P_j = \frac{1}{\Delta_j}\sqrt{\frac{4\ln 2}{\pi}} \exp\left\{-4\ln 2\left(\frac{j - j_{\max}}{\Delta_j}\right)^2\right\} \tag{4.3}$$

and

$$r(j,t) = 0.1 + 0.3\cos(2\omega_j t) \tag{4.4}$$

where $\Delta_j = 4\pi Bj$ is the molecular rotational frequency.[21] Least-squares fitting to the data indicates that the rotational excitation can be modeled with a rotational distribution centred at $j_{max} \approx 30$ of $Hg_2(D1_u)$ and a FWHM Δj of ≈ 90, as shown in Figure 4.4 (b). This is equivalent to $\approx$ 17 cm^{-1} of rotational excitation at the position of maximum population (the spread is 0 - 103 cm^{-1}).

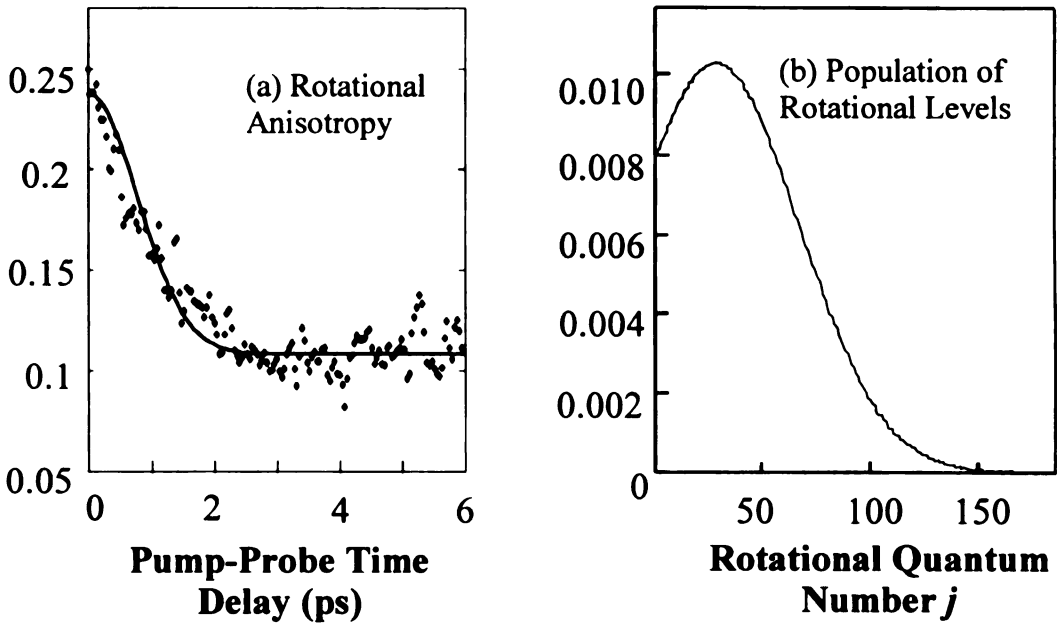

Figure 4.4 (a) Rotational anisotropy *r(t)* obtained from the experimental data. The heavy line is the best fit to the experimental data (plotted as points), as described in the text.

(b) Rotational population of the photoassociated product, obtained from the fit to the rotational anisotropy.

4.3.3 Other Processes

In order to verify that the observed dimer fluorescence and molecular dynamics are a result of photoassociation, we need to consider other processes that might produce the same results. There are several alternatives, including excitation of an existing (van der Waal's) dimer population, photolysis of an equilibrium population of Hg_3 molecules and multiphoton excitation of atoms followed by collisional association to form the excimer. The ratio of dimers to monomers under the experimental conditions is estimated to be $\approx 3.5 \times 10^{-5}$.[iv] In addition, the relative displacement of the two states makes the Franck-

[iv] Calculated by statistical thermodynamic methods using the procedure outlined in Reference 235.

Condon factors for transition between the ground state well and the $D1_u$ state very small ($< 10^{-14}$).[216,222] Also, it requires ≈ 300 cm^{-1} more energy than a 312 nm photon possesses to excite molecules by a vertical transition from the bottom of the ground state to the $D1_u$ state. These factors combine to make bound → bound transitions highly improbable.

At the temperature and pressure conditions of the experiments, the trimer concentration in the cell is estimated to be less than one in 10^{15}. The observed fluorescence intensity is quite substantial; it seems most unlikely that a femtosecond pulse acting on less than $1:10^{15}$ of a total number density of 10^{17} cm^{-3} in a narrow focal area could produce a measurable amount of fluorescence, particularly if that signal was then depleted.

The formation of short-lived ($\tau < 50$ ns) Hg_2^* excimers by collisional association of ground and excited state atoms has been shown to occur.[236] This is probably the origin of the 'background level' of fluorescence; the amount of depletion observed represented only about 10 % of the total undepleted signal. However, collisional association of excited atoms requires three-body collisions. At 160 °C the mean time between two-body collisions is 125 ns;[v] the rise time of any signal associated with three-body collisions would therefore have to be on the order of several hundred nanoseconds. The gate on the boxcar was set to $\approx$ 50 ns for collection of data, which discriminates against slower processes. Also, femtosecond depletion of a nanosecond signal should not produce any

[v] Assuming ideal gas behaviour. Pressure-temperature data obtained from Reference 159, p. **6**-113.

visible change in intensity because the timescale of the probe laser is so short. Most importantly, collisional association of atoms is an inherently isotropic process and could not result in molecular products exhibiting rotational anisotropy as was observed in the time-resolved data collected from the cell at 335 nm (see Figure 4.3). The presence in the cell of excimers formed by collisional association is therefore not expected to interfere with observation of the photoassociation data.

4.3.4 Magnitude of the Signal

The magnitude of the photoassociation signal depends critically on the number of atoms that have a neighbour within the binding distance $\Delta R_x = R_{max} - R_{min}$ at the instant that the binding pulse is applied. To determine this quantity, a radial distribution function $P(r)$ is used to calculate the probability that a shell of radius r and thickness dr centred on a single atom contains a neighbouring atom:

$$P(r) = \int_{R_{min}}^{R_{max}} \rho g(r) 4\pi r^2 dr \tag{4.5}$$

where ρ is the number density of atoms in the vapour and $g(r)$ is the radial distribution function.[235] As a first approximation, we used

$$g(r) = \exp\left[-\frac{V(r)}{kT}\right], \tag{4.6}$$

where $V(r)$ is the potential energy describing the interaction between the atoms and $P(r)$ is the fraction of atoms having a neighbour within the volume described by ΔR_x. Using parameters for the ground state potential from Koperski *et al.*[216] yields $P(r) \approx 7 \times 10^{-7}$. R_{min} and R_{max} were estimated based on the spectrum of the 312 nm pulse, the available

kinetic energy and the vertical transition energy between the $X0_g^+$ and $D1_u$ states.

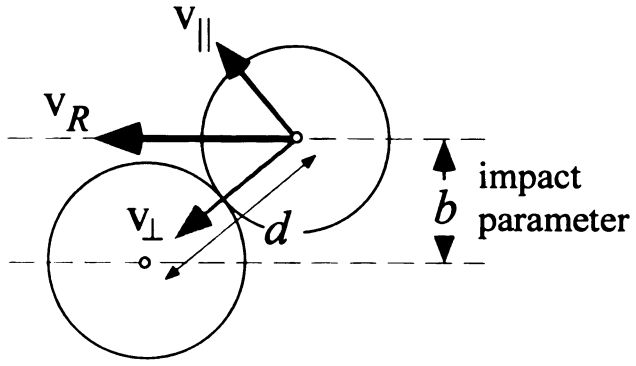

$$E_R = \frac{1}{2}\mu\left(v_{||}^2 + v_{\perp}^2\right) \qquad \frac{E_{\perp}}{E_R} = 1 - \frac{b^2}{d^2}$$

Figure 4.5 Schematic of a bimolecular collision process, illustrating the definition of the impact parameter *b*. The equations show the relation between the relative energy of collision E_R and the energy $E_\perp$ along the direction of the interatomic axis as a function of the impact parameter.

In order for photoassociation to occur, the relative collision energy of an atom pair with a given impact parameter *b* (as defined in Figure 4.5) should satisfy the condition

$$E_{rel} \geq \frac{V_1(R')}{1-(b/R')^2}, \tag{4.7}$$

where $V_1(R')$ is the potential energy of the ground state and R' the internuclear distance at which the laser is resonant with the transition from the ground to the upper electronic state.[69] An expression can be derived for the differential photoassociation cross section $d\sigma_{PA}/db$ using the well-known expression for the scattering cross section:

$$\frac{d\sigma_{PA}}{db} = 2\pi b P(b), \tag{4.8}$$

where $P(b)$ is the opacity function.[1] Integration over the Boltzmann population of scattering states, taking into account the energetic restriction in Equation (4.7), results in

$$P(b) = \exp\left\{-\frac{V_1(R')}{[1-(b/R')^2]k_BT}\right\}. \tag{4.9}$$

Figure 4.6 shows plots of $d\sigma_{PA}/db$ for three values of binding wavelength. Note that at 350 nm, only those collision pairs with very small impact parameters are photoassociated. As the binding laser is tuned to shorter wavelengths, the position of highest photoassociation probability shifts to larger impact parameters and the selectivity is lost. The opacity function in Equation (4.9) reaches a limiting value $P(b) = 1$ at high excitation energies, when $V_1(R')$ approaches zero. This behaviour is also shown in Figure 4.5 for comparison.

The restrictions on impact parameter imposed by Equation (4.9) are reflected in the rotational quantum numbers of the product molecules. The conversion from impact parameter to angular momentum is obtained by using the quantum-to-classical conversion $j\hbar = \mu v b$, where v is the relative velocity of the atoms at the moment when they are photoassociated. Figure 4.6 was plotted using the mean relative velocity $\bar{v}$. Under experimental conditions (σ_{bind} = 312 nm, R' = 2.82 Å), it can be seen that the predicted parameters are $j_{max} \approx 50$ and $\Delta j \approx 65$. A number of assumptions inherent in the model may be responsible for the discrepancy between the experimental and theoretical rotational distribution, see Figure 4.4 (b). The larger Δj in the experimental data may be due to the use of a single average value for the relative velocity of the atoms rather than

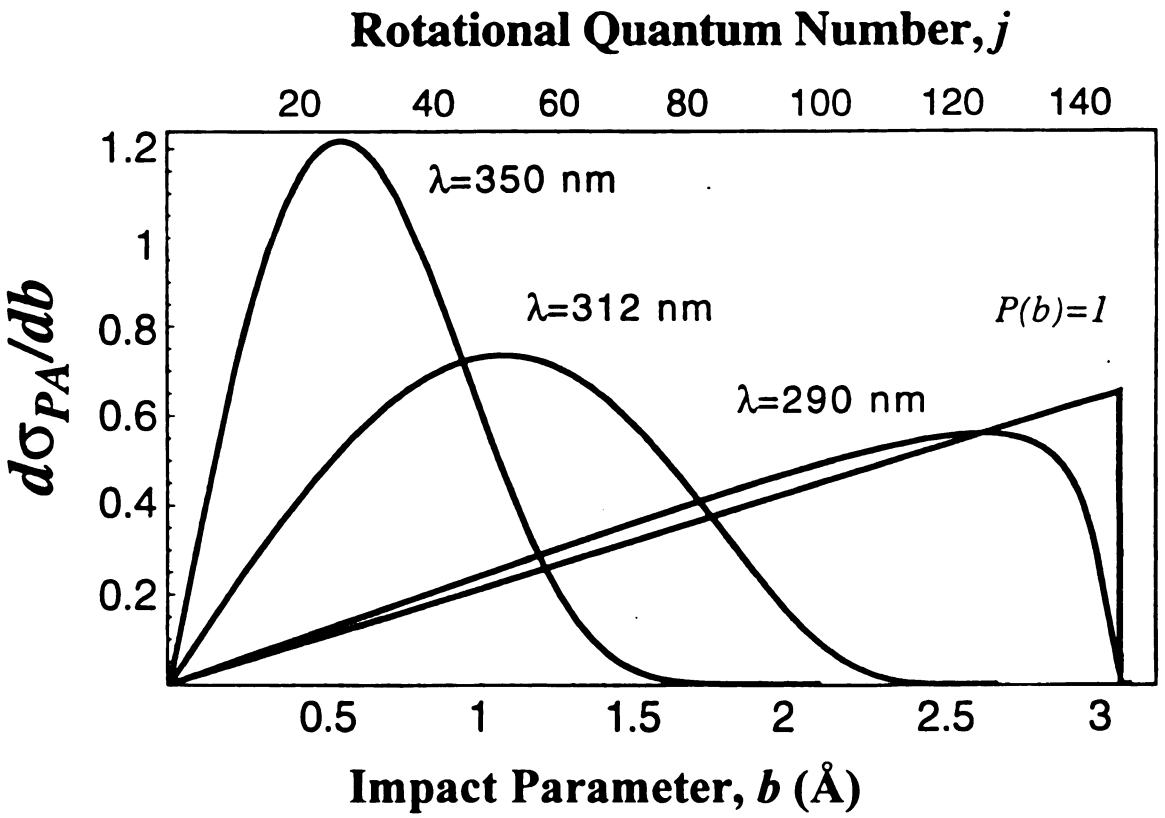

Figure 4.6 The differential photoassociation cross section $d\sigma_{PA}/db$ from Equation 4.9, plotted as a function of binding wavelength. Note that as the wavelength is tuned to lower energies the reaction requires smaller impact parameters and the products are formed with a narrower, lower energy distribution of rotational excitation. At 290 nm the photoassociation process is not very restrictive and approaches the theoretical limit $P(b) = 1$ (see text).

the thermal distribution. A slight saturation of the photoassociation transition by the laser may also make the rotational distribution appear to be broader than it actually is.

Quantum mechanical simulations of this work indicate that it is also possible to observe vibrational coherence in the photoassociated molecules.[69,70,237] However, the modulation depth of these coherences is not large and we have to date been unable to unambiguously identify vibrations in the pump-probe data.

5. SUMMARY AND CONCLUSIONS

Time-resolved spectroscopy using ultrashort pulses is a complementary technique to more conventional, frequency-resolved, spectroscopic methods. The advantage of using ultrashort laser pulses to study molecular processes is that dynamic behaviour can be observed directly, which avoids ambiguities that may arise in the analysis of spectral linewidths, for example. Additionally, the fast nature of the excitation can be used to favour the detection of short-lived species over asymptotic products. In many cases, particularly where reactions are occurring, this allows the observation and analysis of processes that may not be observable by frequency-resolved methods. Two experiments have been performed in which this principle is demonstrated.

Results have been presented of a femtosecond pump-probe experiment on a photoinduced molecular detachment process. Dissociation of gem-dihaloalkanes using multiphoton excitation with a femtosecond pulse was found to produce molecular halogens in ion pair states as a product. The reaction has been shown to be quite general, occurring for a number of dihalogenated molecules and always producing the appropriate halogen in the D' state. The reaction is prompt, and appears to occur without a significant amount of IVR. When iodine was the molecular product, a simple impulsive model was found to reproduce the relative dissociation time for alkane fragments having different masses; this model broke down however with other halogen products.

In the case of molecular detachment of iodine from methylene iodide, vibrational

coherence in the molecular product was observed, indicating that the reaction is concerted. This is a significant result because it demonstrates that a phase coherent wavepacket created in a molecule can persist even after dissociation into products.

At least two other ion-pair states of iodine were observed as products of this reaction. For one of these pathways, rotational anisotropy was observed in the pump-probe data, indicating a high degree of rotational excitation in the molecular product. It was concluded that the observed reaction dynamics and product excitation can best be explained by an asynchronous concerted reaction mechanism, in which one of the carbon-halogen bonds breaks more rapidly than the other. It was not possible to determine the degree of rotational excitation in the $I_2(D')$ product, but analysis of the molecular detachment of Br_2 from CH_2Br_2 indicated a rotational population centred at $j \approx 76$, which is considerably less than was observed for the iodine product in a more highly excited ion-pair state ($j \approx 350$).

The majority of dihaloalkanes studied were of C_{2v} symmetry. Experiments conducted on CH_2ICl showed that for this molecule, the halogen in the D' state was again produced and that the dissociation was very rapid. Analysis of the anisotropy observed in the time data revealed that there was very little rotational excitation in the molecular product, being approximately equal to a thermal distribution centred at $j \approx 10$. This is very different to the results from the rest of the study, in which significant rotational excitation was observed in the products, and indicates a different reaction pathway. This is not unexpected in light of a possible symmetry barrier in molecules of C_{2v} symmetry to the

formation of an interhalogen bond. A barrier of this type would tend to favour an asynchronous concerted mechanism of the type proposed for highly excited ion-pair states of I_2, in which the symmetry of the molecule is broken during dissociation. No such restriction exists in the case of CH_2ICl, so that there is no barrier to a 'direct dissociation' mechanism of the type shown in Figure 3.28 (a). The asynchronous concerted mechanism would be expected to produce a high degree of rotational excitation in the products; an impulsive dissociation retaining the geometry of the parent molecule would not. It seems reasonable therefore that the asynchronous concerted mechanism is the pathway when the parent molecule has C_{2v} symmetry but that the reaction proceeds by the synchronous concerted mechanism when it does not.

In order to determine more about the mechanism of the photoinduced molecular detachment mechanism, it would be very useful to be able to measure the energetics of the alkane fragments. If these experiments were performed in a molecular beam apparatus, time-of flight detection could be used to do this. A reliable description of the excited state of the parent molecule from which the dissociation occurs would also be very useful; theoretical work is underway to allow this.

Results have also been presented of an experiment in which a femtosecond pulse was used to cause an unrestricted bimolecular (photoassociation) reaction. In this case, excitation of unbound mercury atoms in a thermally populated set of continuum states to a bound electronically excited state produces electronically excited dimers (excimers). The restrictive Franck-Condon factor for the excitation process produces phase coherent

wavepackets on the upper state. This allows the molecular dynamics of the reaction and of the nascent products to be studied in real time by fluorescence depletion probing. It was determined that under the conditions of the experiment, the rotational excitation in the mercury excimers can be fit to a Gaussian distribution having a maximum at $j_{max} \approx 30$ and a FWHM Δj of ≈ 90. The rotational excitation in the product reflects the energy restrictions imposed on the photoassociating molecules by the resonance condition with the binding pulse. The effect of this restriction on reactive impact parameters has been analysed.

Observation of vibrational coherence in the nascent dimers would allow a more complete analysis of the energetics, and a fuller understanding of the bond formation process. To date it has not proved possible to unambiguously identify vibrational oscillations in the time resolved data. Part of the difficulty may be the fact that a depletion experiment is inherently more subject to noise variations in the signal. A background-free detection method could help tremendously in elucidating more information about the photoassociation reaction studied here. Additionally, it would be of great interest to study photoassociation reactions between an atom and a diatomic molecule, for example, in which orientation and alignment would also play a rôle.

APPENDICES

APPENDIX A

Mathematical Formulation for Fitting Time Zero Data

In order to simulate the transition state dynamics of the molecular detachment reaction, the signal is treated as a sum of two contributions so that $I_{total}(t) = I_{depletion}(t) + I_{timezero}(t)$, as shown in Figure 3.7.

To model the depletion dynamics, we will use a function of the form shown in Figure 3.7 (a). This can be represented mathematically by $\eta(t)\{e^{-t/\tau}-1\}$, where $\eta(t)$ is a step function and τ represents the decay time of the transition state, which we will assume decays as an exponential. This function will be convoluted with a Gaussian to simulate the effects of the temporal width of the pulse:

$$\eta(t)\left[\exp\left(-\frac{t}{\tau}\right)-1\right]\otimes\frac{1}{x\sqrt{\pi}}\exp\left(-\frac{t^2}{x^2}\right)$$

$$=\frac{1}{x\sqrt{\pi}}\int_0^\infty\exp\left(-\frac{(t-\delta)^2}{x^2}\right)\exp\left(-\frac{t}{\tau}\right)dt-\frac{1}{x\sqrt{\pi}}\int_0^\infty\exp\left(-\frac{(t-\delta)^2}{x^2}\right)dt. \qquad \text{(A1)}$$

where $x=\frac{\sigma}{\sqrt{4\ln 2}}$ and σ is the FWHM of the pulse. Integrating this expression over t produces the dynamic model for depletion of the molecules:

$$\frac{1}{2x}\exp\left[\left(\frac{x}{2\tau}\right)^2-\frac{\delta}{\tau}\right]\left[1+\mathrm{erf}\left(\left|\frac{\delta}{x}-\frac{x}{2\tau}\right|\right)\right]\mathrm{sign}\left(\frac{\delta}{x}-\frac{x}{2\tau}\right)-\frac{1}{2x}\left[1+\mathrm{sign}\left(\frac{\delta}{x}\right)\mathrm{erf}\left(\left|\frac{\delta}{x}\right|\right)\right] \quad \text{(A2)}$$

where δ indicates the time delay between the pump and probe pulses.

In order to model time zero, we need the convolution of a delta function with a Gaussian. This has already been solved; it is the second term in (A1). Thus the complete solution for the molecular dynamics of the molecules at time zero can be represented as shown:

$$A\frac{1}{x\sqrt{\pi}}\exp\left(-\frac{t^2}{x^2}\right)\otimes\eta(t)\left[\exp\left(-\frac{t}{\tau}\right)-1\right]+B\frac{1}{x\sqrt{\pi}}\exp\left(-\frac{t^2}{x^2}\right)\otimes\eta(t)\exp\left(-\frac{t}{\tau}\right)+C$$

$$=A\exp(\alpha^2-\beta)\left[1+\mathrm{sign}(\gamma-\alpha)\mathrm{erf}\left(\left|\gamma-\alpha\right|\right)\right]+\mathrm{Bsign}(\gamma)\mathrm{erf}\left(\left|\gamma\right|\right)+C, \quad \text{(A3)}$$

where $\alpha=\frac{x}{2\tau}$, $\beta=\delta/\tau$ and $\gamma=\delta/x$.

A, B and C are experimentally determined fitting parameters, since we cannot predict *a priori* the amount which each component will contribute to the overall signal. A number of assumptions and approximations were made in this model. First of all, in the interest of simplicity, the changes in signal caused by rotational dephasing and vibrational coherence have not been accounted for. Also, the intensity profile of the pulse in the depletion model is in fact a convolution of the three 312 nm pulses causing the initial excitation with the 624 nm (probe) pulse. For the model, the temporal width of the probe pulse as measured by frequency-resolved optical gating (FROG) was used. This introduces little error because the three-photon excitation will have a considerably narrower temporal width than the 624 nm pulse; the cross-correlation will therefore have

a width very similar to that of the probe. We have also assumed that the convoluted FWHM of the pulses producing the time zero feature is the same as that used for the depletion; the assumption is necessary because the exact excitation process at time zero is not known.

APPENDIX B

Classical Mechanical Simulation of Dissociation Dynamics

To illustrate the general idea of the treatment, we will consider a specific bonding arrangement, *i.e.* atom 1 is initially bonded to atom 2 and atom 2 to atom 3 (*e.g.* the CH_2 pseudo atom to the two I atoms of CH_2I_2). Let m_i, (x_i, y_i) and (v_{xi}, v_{yi}) be the mass, current position and velocity of atom i respectively. At an infinitesimal time δt later, changes of the atomic positions can be determined trivially using $\delta x_1 = v_{x1}\delta t$, *etc.* The changes in the atomic velocities, on the other hand, can be determined by the following set of simultaneous equations:

$$\delta P_x = m_1\delta v_{x1} + m_2\delta v_{x2} + m_3\delta v_{x3} = 0 \qquad \text{(B1) (a)}$$

$$\delta P_y = m_1\delta v_{y1} + m_2\delta v_{y2} + m_3\delta v_{y3} = 0 \qquad \text{(b)}$$

$$\delta J_z = m_1\left(x_1\delta v_{y1} - y_1\delta v_{x1}\right) + m_2\left(x_2\delta v_{y2} - y_2\delta v_{x2}\right) + m_3\left(x_3\delta v_{y3} - y_3\delta v_{x3}\right) = 0 \qquad \text{(c)}$$

$$\frac{1}{2}\delta T = m_1\left(v_{x1}\delta v_{x1} + v_{y1}\delta v_{y1}\right) + m_2\left(v_{x2}\delta v_{x2} + v_{y2}\delta v_{y2}\right) + m_3\left(v_{x3}\delta v_{x3} + v_{y3}\delta v_{y3}\right) = 0 \qquad \text{(d)}$$

$$\frac{1}{2}\delta\frac{dr_{12}^2}{dt} = \left[\left(v_{x1} - v_{x2}\right)^2 + \left(v_{y1} - v_{y2}\right)^2\right]\delta t + \left(x_1 - x_2\right)\left(\delta v_{x1} - \delta v_{x2}\right) + \left(y_1 - y_2\right)\left(\delta v_{y1} - \delta v_{y2}\right) = 0 \qquad \text{(e)}$$

$$\frac{1}{2}\delta\frac{dr_{23}^2}{dt} = \left[\left(v_{x2} - v_{x3}\right)^2 + \left(v_{y2} - v_{y3}\right)^2\right]\delta t + \left(x_2 - x_3\right)\left(\delta v_{x2} - \delta v_{x3}\right) + \left(y_2 - y_3\right)\left(\delta v_{y2} - \delta v_{y3}\right) = 0 \qquad \text{(f)}$$

where equations B1 (a) – (d) are essentially the conservation laws of momentum, angular momentum and kinetic energy. Equations B1 (e) and (f) are imposed by the rigid bonds between atoms 1 and 2 and between atoms 2 and 3 respectively. These equations govern the free propagation of the triatomic system.

Now consider the situation of a bond breaking event, specifically breaking of the 1–2 bond with an excess energy E. Assuming that the bond breaking event is instantaneous, there is no change in the position of each atom before and after the breaking. But there will be abrupt changes in the velocities of the atoms, which can be obtained by solving the following simultaneous equations:

$$\delta P_x = m_1 \delta v_{x1} + m_2 \delta v_{x2} + m_3 \delta v_{x3} = 0 \qquad \text{(B2) (a)}$$

$$\delta P_y = m_1 \delta v_{y1} + m_2 \delta v_{y2} + m_3 \delta v_{y3} = 0 \qquad \text{(b)}$$

$$\delta J_z = m_1\left(x_1 \delta v_{y1} - y_1 \delta v_{x1}\right) + m_2\left(x_2 \delta v_{y2} - y_2 \delta v_{x2}\right) + m_3\left(x_3 \delta v_{y3} - y_3 \delta v_{x3}\right) = 0 \qquad \text{(c)}$$

$$\frac{1}{2}\delta T = m_1\left(v_{x1} \delta v_{x1} + v_{y1} \delta v_{y1}\right) + m_2\left(v_{x2} \delta v_{x2} + v_{y2} \delta v_{y2}\right) + m_3\left(v_{x3} \delta v_{x3} + v_{y3} \delta v_{y3}\right) = E/2 \qquad \text{(d)}$$

$$\frac{\delta v_{x1}}{\delta v_{y1}} = \frac{x_1 - x_2}{y_1 - y_2} \qquad \text{(e)}$$

$$\frac{1}{2}\delta \frac{dr_{23}^2}{dt} = \left(x_2 - x_3\right)\left(\delta v_{x2} - \delta v_{x3}\right) + \left(y_2 - y_3\right)\left(\delta v_{y2} - \delta v_{y3}\right) = 0 \qquad \text{(f)}$$

where Equations B2 (a) – (c) are identical to those in B1. Equation B2 (e) reflects the restriction that bond breaking results in axial recoil. Similar free propagation and bond breaking equations can also be obtained for other bonding arrangements and bond formation and bond breaking processes. With these equations, the motion of the atoms

can be predicted and mechanical quantities such as the angular momentum of the fragments can be obtained readily.

1 R. D. Levine and R. B. Bernstein, *Molecular Reaction Dynamics and Chemical Reactivity* (Oxford University Press, New York, 1987).

2 D. M. Neumark, *Annu. Rev. Phys. Chem.* **43,** 153 (1992).

3 G. Herzberg, in *Molecular spectra and molecular structure*, Vol. III, 2nd ed. (Van Nostrand, New York, 1966).

4 J. C. Polanyi and A. H. Zewail, *Acc. Chem. Res.* **28,** 119 (1995).

5 C. V. Shank and B. I. Greene, *J. Phys. Chem.* **87,** 732 (1983).

6 G. Fleming, *Chemical Applications of Ultrafast Spectroscopy* (Clarendon Press, Oxford, 1986).

7 C. V. Shank, *Science* **233,** 1276 (1986). and references therein.

8 L. Dhar, J. A. Rogers and K. A. Nelson, *Chem. Rev.* **94,** 157 (1994).

9 M. Motzkus, S. Pedersen and A. H. Zewail, *J. Phys. Chem.* **100,** 5620 (1996).

10 T. Kobayashi, in *Modern Nonlinear Optics, Part 3*, edited by M. Evans and S. Kielich (John Wiley & Sons, Inc., 1994).

11 G. K. Paramonov, *Chem. Phys. Lett.* **169,** 573 (1990).

12 J. Manz, in *Femtochemistry and Femtobiology*, edited by V. Sundström (World Scientific, Singapore, 1997), p. 98 .

13 M. Dantus and P. Gross, in *Encyclopedia of Applied Physics*, Vol. 22 (Wiley-VCH Verlag GmbH, 1998), p. 431.

14 E. J. Heller, *Acc. Chem. Res.* **14,** 368 (1981).

15 D. Huber, S. Ling, D. G. Imre and E. J. Heller, *J. Chem. Phys.* **90,** 7317 (1989).

16 D. Huber and E. J. Heller, *J. Chem. Phys.* **89,** 4752 (1988).

17 S. Y. Lee, in *Femtosecond Chemistry*, Vol. 1, edited by J. Manz and L. Woste (VCH, Weinheim, 1995), p. 273.

18 Y.-X. Yan and K. A. Nelson, *J. Chem. Phys.* **87,** 6240 (1989).

19 Y.-X. Yan and K. A. Nelson, *J. Chem. Phys.* **87,** 6257 (1989).

20 R. B. Bernstein and A. H. Zewail, *Chem. Phys. Lett.* **170,** 321 (1990).

21 J. S. Baskin and A. H. Zewail, *J. Phys. Chem.* **98,** 3337 (1994).

22 D. M. Jonas, S. E. Bradforth, S. A. Passino and G. R. Fleming, *J. Phys. Chem.* **99,** 2594 (1995).

23 R. Bersohn and A. H. Zewail, *Ber. Bunsenges. Phys. Chem.* **92,** 373 (1988).

24 J. Cao and K. R. Wilson, *J. Chem. Phys.* **106,** 5062 (1997).

25 M. Gruebele and A. H. Zewail, *J. Chem. Phys.* **98,** 883 (1993).

26 P. M. Felker, *J. Phys. Chem.* **98,** 7844 (1992).

27 M. Gruebele, G. Roberts, M. Dantus, R. M. Bowman and A. H. Zewail, *Chem. Phys. Lett.* **166,** 459 (1990).

28 R. Baer and R. Kosloff, *J. Phys. Chem.* **99,** 2534 (1995).

29 R. Baer and R. Kosloff, *Chem. Phys. Lett.* **200,** 183 (1992).

30 M. J. Rosker, M. Dantus and A. H. Zewail, *J. Chem. Phys.* **89,** 6113 (1988).

31 T. Seideman, *J. Chem. Phys.* **103,** 7887 (1995).

32 M. Dantus, R. M. Bowman, J. S. Baskin and A. H. Zewail, *Chem. Phys. Lett.* **159,** 406 (1989).

33 M. Dantus, R. M. Bowman and A. H. Zewail, *Nature* **343,** 737 (1990).

34 P. M. Felker, J. S. Baskin and A. H. Zewail, *J. Phys. Chem.* **90,** 724 (1986).

35 P. M. Felker and A. H. Zewail, *J. Chem. Phys.* **86,** 2460 (1987).

36 R. G. Gordon, *J. Chem. Phys.* **45,** 1643 (1966).

37 Q. Zhang, U. Marvet and M. Dantus, *J. Chem. Phys.* **109,** 4428 (1998).

38 A. H. Zewail, *J. Chem. Soc. Faraday Trans 2* **85,** 1221 (1989).

39 L. D. Landau and E. M. Lifshitz, *Mechanics*, 3rd ed. (Pergamon Press, Oxford, 1976).

40 R. Bersohn, in *Molecular Photodissociation Dynamics*, edited by M. N. R. Ashfold and J. E. Baggot (1987), p. 1.

41 T. S. Rose, M. J. Rosker and A. H. Zewail, *J. Chem. Phys.* **91,** 7415 (1989).

42 A. Materny, J. L. Herek, P. Cong and A. H. Zewail, *J. Phys. Chem.* **98,** 3352 (1994).

43 M. Dantus, PhD, California Institute of Technology, 1991.

44 T. S. Rose, M. J. Rosker and A. H. Zewail, *J. Chem. Phys.* **88,** 6672 (1988).

45 M. Dantus, R. M. Bowman, M. Gruebele and A. H. Zewail, *J. Chem. Phys.* **91,** 7437 (1989).

46 M. Dantus, M. J. Rosker and A. H. Zewail, *J. Chem. Phys.* **87,** 2395 (1987).

47 M. Dantus, M. J. Rosker and A. H. Zewail, *J. Chem. Phys.* **89,** 6128 (1988).

48 N. Scherer, *J. Chem. Phys.* **92,** 5239 (1990).

49 D. M. Neumark, *Acc. Chem. Res.* **26,** 33 (1993).

50 C. Jouvet and B. Soep, *Chem. Phys. Lett.* **96,** 426 (1983).

51 C. Jouvet and B. Soep, *J. Chem. Phys.* **80,** 2229 (1984).

52 S. Buelow, G. Radhakrishnan, J. Catanzarite and C. Wittig, *J. Chem. Phys.* **83,** 444 (1985).

53 S. Buelow, M. Noble, G. Radhakrishnan, H. Reisler, C. Wittig and G. Hancock, *J. Phys. Chem.* **90,** 1015 (1986).

54 G. Radhakrishnan, S. Buelow and C. Wittig, *J. Chem. Phys.* **84,** 727 (1986).

55 N. F. Scherer, L. R. Khundkar, R. B. Bernstein and A. H. Zewail, *J. Chem. Phys.* **87,** 1451 (1987).

56 J. P. Visticot, B. Soep and C. J. Whitham, *J. Phys. Chem.* **92,** 4574 (1988).

57 R. Sims, M. Gruebele, E. D. Potter and A. H. Zewail, *J. Chem. Phys.* **97,** 4127 (1992).

58 S. I. Ionov, G. A. Brucker, C. Jaques, Valachovic and C. Wittig, *J. Chem. Phys.* **99,** 6553 (1993).

59 S. K. Shin, C. Wittig and W. A. Goddard, *J. Phys. Chem.* **95,** 8048 (1991).

60 M. Alagia, N. Balucani, P. Casavecchia, D. Stranges and G. G. Volpi, *J. Chem. Phys.* **98,** 8341 (1993).

61 C. Wittig and A. H. Zewail, in *Chemical Reactions in Clusters* (Oxford University Press, New York, 1996), p. 64.

62 H. B. Levine and G. Birnbaum, *Phys. Rev.* **154,** 86 (1966).

63 E. Hudis, Y. Ben-Aryeh and U. P. Oppenheim, *Phys. Rev. A* **43,** 3631 (1991).

64 A. v. Hellfeld, J. Caddick and J. Weiner, *Phys. Rev. Lett.* **40,** 1369 (1978).

65 H. P. Grieneisen and R. E. Francke, *Chem. Phys. Lett.* **88,** 585 (1982).

66 V. S. Dubov, L. I. Gudzenko, L. V. Gurvich and Iokovlenko, *Chem. Phys. Lett.* **45,** 330 (1977).

67 M. Machholm, A. Giusti-Suzor and F. H. Mies, *Phys. Rev. A* **50,** 5025 (1994).

68 U. Marvet and M. Dantus, *Chem. Phys. Lett.* **245,** 393 (1995).

69 P. Gross and M. Dantus, *J. Chem. Phys.* **106,** 8013 (1997).

70 P. Backhaus and B. Schmidt, *Chem. Phys.* **217,** 131 (1997).

71 T. R. Gosnell, A. J. Taylor and J. L. Lyman, *J. Chem. Phys.* **94,** 5949 (1991).

72 K. Saitow, Y. Naitoh, K. Tominaga and K. Yoshihara, *Chem. Phys. Lett.* **262,** 621 (1996).

73 J. H. Glownia, J. A. Misewich and P. P. Sorokin, *J. Chem. Phys.* **92,** 3335 (1990).

74 J. H. Glownia, R. E. Walkup, D. R. Gnass, M. Kaschke, J. A. Misewich and P. P. Sorokin, in *Femtosecond Chemistry*, Vol. 1, edited by J. Manz and L. Woste (VCH, Weinheim, 1995), p. 131.

75 M. H. M. Janssen, M. Dantus, H. Guo and A. H. Zewail, *Chem. Phys. Lett.* **214,** 281 (1993).

76 C. C. Hayden and D. W. Chandler, *J. Phys. Chem.* **99,** 7897 (1995).

77 J. L. Knee, in *Femtosecond Chemistry*, Vol. 1, edited by J. Manz and L. Woste (VCH, Weinheim, 1995), p. 167.

78 C. Meier and V. Engel, in *Femtosecond Chemistry*, Vol. 1, edited by J. Manz and L. Woste (VCH, Weinheim, 1995), p. 369.

79 E. Schrodinger, *Naturwiss* **14,** 664 (1926).

80 P. Ehrenfest, *Z. Physik* **45,** 455 (1927).

81 T. F. George, *J. Phys. Chem.* **86,** 10 (1982).

82 D. J. Tannor and S. A. Rice, *J. Chem. Phys.* **83,** 5013 (1985).

83 D. J. Tannor, R. Kosloff and S. A. Rice, *J. Chem. Phys.* **85,** 5805 (1986).

84 D. Neuhauser and H. Rabitz, *Acc. Chem. Res.* **26,** 496 (1993).

85 W. S. Warren, H. Rabitz and M. Dahleh, *Science* **259,** 1581 (1993).

86 M. Shapiro, J. W. Hepburn and P. Brumer, *Chem. Phys. Lett.* **149,** 451 (1988).

87 J. L. Krause, M. Shapiro and P. Brumer, *J. Chem. Phys.* **92,** 1126 (1990).

88 J. L. Krause, R. M. Whitnell, K. R. Wilson, Y. Yan and S. Mukamel, *J. Chem. Phys.* **99,** 6562 (1993).

89 R. S. Judson and H. Rabitz, *Phys. Rev. Lett.* **68,** 1500 (1992).

90 P. Brumer and M. Shapiro, *Acc. Chem. Res.* **22,** 407 (1989).

91 Y. Yan, R. E. Gillilan, R. M. Whitnell, K. R. Wilson and S. Mukamel, *J. Phys. Chem.* **97,** 2320 (1993).

92 N. F. Scherer, A. J. Ruggiero, M. Du and G. R. Fleming, *J. Chem. Phys.* **93,** 856 (1990).

93 N. F. Scherer, R. J. Carlson, A. Matro, M. Du, A. J. Ruggiero, V. Romero-Rochin, J. A. Cina, G. R. Fleming and S. A. Rice, *J. Chem. Phys.* **95,** 1487 (1991).

94 E. D. Potter, J. L. Herek, S. Pedersen, Q. Liu and A. H. Zewail, *Nature* **355,** 66 (1992).

95 V. D. Kleiman, L. Zhu, J. Allen and R. J. Gordon, *J. Chem. Phys.* **103,** 10800 (1995).

96 M. Blackwell, P. Ludowise and Y. Chen, *J. Chem. Phys.* **107,** 283 (1997).

97 I. Pastirk, E. J. Brown, Q. Zhang and M. Dantus, *J. Chem. Phys.* **108,** 4375 (1998).

98 J. Cao and K. R. Wilson, *J. Chem. Phys.* **107,** 1441 (1997).

99 D. S. Bethune, *Appl. Opt.* **20,** 1897 (1981).

100 R. L. Fork, C. V. Shank and R. T. Yen, *Appl. Phys. Lett.* **41,** 223 (1982).

101 T. Sizer II, J. D. Kafka, I. N. Duling III, C. W. Gabel and G. A. Mourou, *IEEE J. Quantum Electron.* **QE-19,** 506 (1983).

102 M. M. Murnane and R. W. Falcone, *J. Opt. Soc. Am. B* **5,** 1573 (1988).

103 A. Migus, C. V. Shank, E. P. Ippen and R. L. Fork, *IEEE J. Quant. El.* **QE-18,** 101 (1982).

104 W. H. Knox, *IEEE J. Quantum Electron.* **QE-24,** 388 (1988).

105 A. E. Siegman, *Lasers* (University Science Books, 1986).

106 R. L. Fork, C. V. Shank, R. Yen and C. A. Hirliman, *IEEE J. Quantum Electron.* **QE-19,** 500 (1983).

107 J. A. Valdmanis and R. L. Fork, *IEEE J. Quantum Electron.* **QE-22,** 112 (1986).

108 F. Salin and A. Brun, *J. Appl. Phys.* **61,** 4736 (1987).

109 D. J. Kane and R. Trebino, *Optics Lett.* **18,** 823 (1993).

110 D. J. Kane and R. Trebino, *IEEE J. Quantum Electron* **29,** 571 (1993).

111 R. Trebino and D. J. Kane, *J. Opt. Soc. Am.* **A10,** 1101 (1993).

112 G. C. G. Waschewsky, D. C. Kitchen, P. W. Browning and L. J. Butler, *J. Phys. Chem.* **99,** 2635 (1995).

113 H. Okabe, *Photochemistry of Small Molecules* (Wiley, New York, 1978).

114 L. J. Butler, E. J. Hintsa, S. F. Shane and Y. T. Lee, *J. Chem. Phys.* **86,** 2051 (1987).

115 R. B. Woodward and R. Hoffmann, *Angew. Chem. Int. Ed. Engl.* **8,** 781 (1969).

116 M. J. S. Dewar, *J. Am. Chem. Soc.* **106,** 209 (1984).

117 C. E. M. Strauss and P. L. Houston, *J. Phys. Chem.* **94,** 8751 (1990).

118 B. H. Mahan, *Chem. Dynamics* **8,** 55 (1975).

119 W. T. Borden, R. J. Loncharich and K. N. Houk, *Ann. Rev. Phys. Chem.* **39,** 213 (1988).

120 E. F. Cromwell, D.-J. Liu, M. J. J. Vrakking, A. H. Kung and Y. T. Lee, *J. Chem. Phys.* **95,** 297 (1991).

121 J. Steadman and T. Baer, *J. Chem. Phys.* **91,** 6113 (1989).

122 P. J. Dyne and D. W. G. Style, *J. Chem. Soc.* , 2122 (1952).

123 D. W. G. Style and J. C. Ward, *J. Chem. Soc.* , 2125 (1952).

124 H. Okabe, M. Kawasaki and Y. Tanaka, *J. Chem. Phys.* **73,** 6162 (1980).

125 C. Fotakis, M. Martin and R. J. Donovan, *J. Chem. Soc. Faraday Trans.* **78,** 1363 (1982).

126 Research on High Energy Storage for Laser Amplifiers, edited by G. Black (Stanford Research Institute, 1976).

127 H. Okabe, A. H. Laufer and J. J. Ball, *J. Chem. Phys.* **55,** 373 (1971).

128 S. R. Cain, R. Hoffmann and E. R. Grant, *J. Phys. Chem.* **85,** 4046 (1981).

129 P. M. Kroger, P. C. Demou and S. J. Riley, *J. Chem. Phys.* **65,** 1823 (1976).

130 S. L. Baughcum and S. R. Leone, *J. Chem. Phys.* **72,** 6531 (1980).

131 T. F. Hunter and K. S. Kristjansson, *Chem. Phys. Lett.* **90,** 35 (1982).

132 M. Kawasaki, S. J. Lee and R. Bersohn, *J. Chem. Phys.* **63,** 809 (1975).

133 W. H. Pence, S. L. Baughcum and S. R. Leone, *J. Phys. Chem.* **85,** 3844 (1981).

134 J. Zhang, E. J. Heller, D. Huber, D. G. Imre and D. Tannor, *J. Chem. Phys.* **89,** 3602 (1988).

135 J. Zhang and D. G. Imre, *J. Chem. Phys.* **89,** 309 (1988).

136 B. J. Schwartz, J. C. King, J. Z. Zhang and C. B. Harris, *Chem. Phys. Lett.* **203,** 503 (1993).

137 W. M. Kwok and D. L. Phillips, *Chem. Phys. Lett.* **235,** 260 (1995).

138 W. M. Kwok and D. L. Phillips, *J. Chem. Phys.* **104,** 2529 (1996).

139 F. Duschek, M. Schmitt, P. Vogt, A. Materny and W. Kiefer, *J. Raman Spectrosc.* **28,** 445 (1997).

140 M. N. Glukhovtsev and R. D. Bach, *Chem. Phys. Lett.* **269,** 145 (1997).

141 Z. Kisiel, L. Pszczolkowski, W. Caminati and P. G. Favero, *J. Chem. Phys.* **105,** 1778 (1996).

142 X. Zheng, S. Fei, M. C. Heaven and J. Tellinghuisen, *J. Chem. Phys.* **96,** 4877 (1992).

143 J. Tellinghuisen, *J. Mol. Spectrosc.* **94,** 231 (1982).

144 H. Hemmati and G. J. Collins, *Chem. Phys. Lett.* **75,** 488 (1980).

145 A. Sur and J. Tellinghuisen, *J. Mol. Spectrosc.* **88,** 323 (1981).

146 J. B. Koffend, A. M. Sibai and R. Bacis, *J. Physique* **43,** 1639 (1982).

147 P. C. Tellinghuisen, B. Guo, D. K. Chakraborty and J. Tellinghuisen, *J. Mol. Spectrosc.* **128,** 268 (1988).

148 J. C. D. Brand and A. R. Hoy, *Appl. Spectrosc. Rev.* **23,** 285 (1987).

149 P. J. Jewsbury, K. P. Lawley, T. Ridley, F. F. Al-Adel, P. R. R. Langridge-Smith and R. J. Donovan, *Chem. Phys.* **151,** 103 (1991).

150 K. Lawley, P. Jewsbury, T. Ridley, P. Langridge-Smith and R. Donovan, *Mol. Phys.* **75,** 811 (1992).

151 P. J. Wilson, T. Ridley, K. P. Lawley and R. J. Donovan, *Chem. Phys.* **182,** 325 (1994).

152 J. Tellinghuisen, *J. Chem. Phys.* **82,** 4012 (1985).

153 A. D. Bandrauk, in *Femtosecond Chemistry*, Vol. 1, edited by J. Manz and L. Woste (VCH, Weinheim, 1995), p. 261.

154 Q. Zhang, U. Marvet and M. Dantus, *J. Chem. Soc., Faraday Discuss.* **108** (1997).

155 K. S. Viswanathan, A. Sur and J. Tellinghuisen, *J. Mol. Spectrosc.* **86,** 393 (1981).

156 K. S. Viswanathan and J. Tellinghuisen, *J. Mol. Spectrosc.* **101,** 285 (1983).

157 J. Tellinghuisen, *Chem. Phys. Lett.* **49,** 485 (1977).

158 Handbook of Chemistry and Physics, 77th ed., edited by D. R. Lide (Chemical Rubber Company Press, **1996-7**), pp. **6**_79.

159 Handbook of Chemistry and Physics, 53rd ed., edited by D. R. Lide (Chemical Rubber Company Press, 1972-3), pp. **D**_151.

160 G. L. Gutsev and T. Ziegler, *J. Phys. Chem.* **95,** 7220 (1991).

161 S. Koda, *Chem. Phys.* **66,** 383 (1982).

162 NIST Chemistry WebBook (Online) , edited by W. G. Mallard and P. J. Linstrom (National Institute of Standards and Technology, Gaithersburg MD, 1998).

163 S. A. Kudchadker and A. P. Kudchadker, *J. Phys. Chem. Ref. Data* **4,** 457 (1975).

164 J. C. D. Brand, D. Bussieres, A. R. Hoy and S. M. Jaywant, *Chem. Phys. Lett.* **109,** 101 (1984).

165 J. D. Spivey, J. G. Ashmore and J. Tellinghuisen, *Chem. Phys. Lett.* **109,** 456 (1984).

166 J. B. Hudson, L. J. Sauls, P. C. Tellinghuisen and J. Tellinghuisen, *J. Mol. Spectrosc.* **148,** 50 (1991).

167 G. V. Calder and W. F. Giauque, *J. Phys. Chem.* **69,** 2443 (1965).

168 J. A. Coxon and M. A. Wickramaaratchi, *J. Mol. Spectrosc.* **79,** 380 (1980).

169 J. A. Coxon, R. M. Gordon and M. A. Wickramaaratchi, *J. Mol. Spectrosc.* **79,** 363 (1980).

170 R. S. Mulliken, *J. Chem. Phys.* **55,** 288 (1971).

171 K. Wieland, J. B. Tellinghuisen and A. Nobs, *J. Mol. Spectrosc.* **41,** 69 (1972).

172 G. Herzberg, *Molecular Spectra and Molecular Structure* (Van Nostrand Reinhold, New York, 1945).

173 W. K. Kang, K. W. Jung, K.-H. Jung and H. J. Hwang, *J. Phys. Chem.* **98,** 1525 (1994).

174 W. K. Kang, K. W. Jung, D. C. Kim, K.-H. Jung and H.-S. Im, *Chem. Phys.* **196,** 363 (1995).

175 Gaussian 94, Revision D.3 ed., edited by M. J. Frisch, G. W. Trucks, H. B. Schlegel, P. M. W. Gill, B. G. Johnson, M. A. Robb, J. R. Cheeseman, T. Keith, G.

A. Petersson, J. A. Montgomery, K. Raghavachari, M. A. Al-Laham, V. G. Zakrzewski, J. V. Ortiz, J. B. Foresman, J. Cioslowski, B. B. Stefanov, A. Nanayakkara, M. Challacombe, C. Y. Peng, P. Y. Ayala, W. Chen, M. W. Wong, J. L. Andres, E. S. Replogle, R. Gomperts, R. L. Martin, D. J. Fox, J. S. Binkley, D. J. Defrees, J. Baker, J. P. Stewart, M. Head-Gordon, C. Gonzalez and J. A. Pople (Gaussian, Inc., Pittsburgh, PA, 1995).

176 A. P. Scott and L. Radom, *J. Phys. Chem.* **100,** 16502 (1996).

177 J. A. Pople, A. P. Scott, M. W. Wong and L. Radom, *Isr. J. Chem.* **33,** 345 (1993).

178 F. L. Voelz, F. F. Cleveland and A. G. Meister, *J. Opt. Soc. Am.* **43,** 1061 (1953).

179 G. Maier and H. P. Reisenauer, *Angew. Chem. Int. Ed. Engl.* **25,** 819 (1986).

180 S. Mrozowski, *Z. Physik* **106,** 458 (1937).

181 R. O. Doyle, *J. Quant. Rad. Spec. Transfer* **8,** 1555 (1968).

182 D. B. Lidov, R. W. Fakone, T. F. Young and S. E. Harris, *Phys. Rev.* **36,** 462 (1976).

183 G. Inoue, J. K. Ku and D. W. Setser, *J. Chem. Phys.* **80,** 6006 (1984).

184 J. H. Schloss, R. B. Jones and J. G. Eden, *J. Chem. Phys.* **99,** 6483 (1993).

185 R. B. Jones, J. H. Schloss and J. G. Eden, *J. Chem. Phys.* **98,** 4317 (1993).

186 E. B. Gordon, V. G. Egorov, S. E. Nalivaiko, V. S. Pavlenko and O. S. Rzhevsky, *Chem. Phys. Lett.* **242,** 75 (1995).

187 T. Bergeman and P. Liao, *J. Chem. Phys.* **72,** 886 (1980).

188 H. Scheingraber and C. R. Vidal, *J. Chem. Phys.* **66,** 3694 (1977).

189 J. D. Miller, R. A. Cline and D. J. Heinzen, *Phys. Rev. Lett.* **71,** 2204 (1993).

190 R. Napolitano, J. Weiner, C. J. Williams and P. S. Julienne, *Phys. Rev. Lett.* **73,** 1352 (1994).

191 P. D. Lett, P. S. Julienne and W. D. Philips, *Ann. Rev. Phys. Chem.* **46,** 423 (1995).

192 H. R. Thorsheim, J. Weiner and P. S. Julienne, *Phys. Rev. Lett.* **58,** 2420 (1987).

193 R. A. Cline, J. D. Miller and D. J. Heinzen, *Phys. Rev. Lett.* **73,** 632 (1994).

194 P. D. Kleiber, A. M. Lyrra, K. M. Sando, V. Zafiropoulos and W. C. Stwalley, *J. Chem. Phys.* **85,** 5493 (1986).

195 P. D. Kleiber, A. M. Lyrra, K. M. Sando, S. P. Heneghan and W. C. Stwalley, *Phys. Rev. Lett.* **54,** 2003 (1985).

196 S. Bililign, P. D. Kleiber, W. R. Kearney and K. M. Sando, *J. Chem. Phys.* **96,** 218 (1992).

197 S. Bililign and P. D. Kleiber, *Phys. Rev. A* **42,** 6938 (1990).

198 M. D. Barnes, P. R. Brooks, R. F. Curl and P. W. Harland, *J. Chem. Phys.* **94,** 5245 (1991).

199 T. C. Maguire, P. R. Brooks, R. F. Curl, J. H. Spence and S. J. Ulvick, *J. Chem. Phys.* **85,** 844 (1986).

200 E. W. Smith, R. E. Drullinger, M. M. Hessel and J. Cooper, *J. Chem. Phys.* **66,** 5667 (1977).

201 D. J. Ehrlich and R. M. Osgood, *Phys. Rev. Lett.* **41,** 547 (1978).

202 S. Majetich, C. A. Tomczyk and J. R. Wiesenfeld, *J. Appl. Phys.* **69,** 563 (1991).

203 M. Shapiro and P. Brumer, *Phys. Rev. Lett.* **77,** 2574 (1996).

204 D. Holmes, P. Brumer and M. Shapiro, *J. Chem. Phys.* **105,** 9162 (1996).

205 R. W. Falcone, W. R. Green, J. C. White, J. F. Young and S. E. Harris, *Phys. Rev. A* **15,** 1333 (1977).

206 P. L. Cahuzac and P. E. Toschek, *Phys. Rev. Lett.* **40,** 1087 (1978).

207 P. Y. Cheng, D. Zhong and A. H. Zewail, *J. Chem. Phys.* **103,** 5153 (1995).

208 T. O. Nelson, D. W. Setser and J. Qin, *J. Phys. Chem.* **97,** 2585 (1992).

209 J. Qin and D. W. Setser, *Chem. Phys. Lett.* **184,** 121 (1991).

210 F. Huang, D. W. Setser and B. S. Cheong, *Isr. J. Chem.* **34,** 127 (1994).

211 I. D. Petsalakis, T. Mercouris and C. A. Nicolaides, *Chem. Phys.* **189,** 615 (1994).

212 T. Mercouris, I. D. Petsalakis and C. A. Nicolaides, *Chem. Phys. Lett.* **208,** 197 (1993).

213 U. Marvet and M. Dantus, in *Femtochemistry: Ultrafast Chemical and Physical Processes in Molecular Systems*, edited by M. Chergui (World Scientific, Singapore, 1996), p. 138.

214 M. Stock, E. W. Smith, R. E. Drullinger and M. M. Hessel, *J. Chem. Phys.* **68,** 4167 (1978).

215 R. E. Drullinger, M. M. Hessel and E. W. Smith, *J. Chem. Phys.* **66,** 5656 (1977).

216 J. Koperski, J. B. Atkinson and L. Krause, *Can. J. Phys.* **72,** 1070 (1994).

217 M. Sampoli, F. Barocchi, A. Guasti, R. Winter, J. Rathenow and F. Hensel, *Phys. Rev. A* **45,** 6910 (1992).

218 R. D. van Zee, S. C. Blankespoor and T. S. Zwier, *J. Chem. Phys.* **88,** 4650 (1988).

219 R. Niefer, J. B. Atkinson and L. Krause, *J. Phys. B* **16,** 3531 (1983).

220 R. J. Niefer, J. Supronowicz, J. B. Atkinson and L. Krause, *Phys. Rev. A* **35,** 4629 (1987).

221 A. Zehnacker, M. C. Duval, C. Jouvet, C. Ladeux-Dedonder, D. Solgadi, B. Soep and O. Bonoist d'Azy, *J. Chem. Phys.* **86,** 6565 (1987).

222 J. Koperski, J. B. Atkinson and L. Krause, *Chem. Phys. Lett.* **219,** 161 (1994).

223 F. Barocchi, M. Sampoli, F. Hensel, J. Rathenow and R. Winter, *J. Non-Cryst. Solids* **156-158,** 663 (1993).

224 J. Supronowicz, R. J. Niefer, J. B. Atkinson and L. Krause, *J. Phys. B: At. Mol. Phys.* **19,** 1153 (1986).

225 A. Czajkowski, W. Kedzierski, J. B. Atkinson and L. Krause, *Chem. Phys. Lett.* **238,** 327 (1995).

226 W. Kedzierski, J. Supronowicz, A. Czajkowski, J. B. Atkinson and L. Krause, *J. Mol. Spectrosc.* **173,** 510 (1995).

227 R. J. Niefer, J. Supronowicz, J. B. Atkinson and L. Krause, *Phys. Rev. A* **34,** 1137 (1986).

228 M. Stupavsky, G. W. F. Drake and L. Krause, *Phys. Lett.* **39 A,** 349 (1972).

229 P. Schwerdtfeger, J. Li and P. Pyykko, *Theor. Chim. Acta.* **87,** 313 (1994).

230 F. H. Mies, W. J. Stevens and M. Krauss, *J. Mol. Spectrosc.* **72,** 303 (1978).

231 R. E. Drullinger, M. M. Hessel and E. W. Smith, *Natl. Bur. Standards Monograph* **143** (1975).

232 A. C. Vikis and D. J. Le Roy, *Phys. Lett.* **44A,** 325 (1973).

233 Handbook of Chemistry and Physics, 74th ed., edited by D. R. Lide (CRC, Boca Raton, 1993-4).

234 R. J. Hay, T. H. Dunning and R. C. Raffenetti, *J. Chem. Phys.* **65,** 2679 (1976).

235 D. A. McQuarrie, *Statistical Mechanics* (Harper and Row, New York, 1976).

236 A. B. Callear and K.-L. Lai, *Chem. Phys.* **69,** 1 (1982) and references therein.

237 P. Backhaus, J. Manz and B. Schmidt, *Adv. Chem. Phys.* (1997) (in press).